UNIVERSITY
OF OSLO

Lisa M. Buschmann

Ionospheric Plasma Structuring at High Latitudes

Studies with in-situ Measurements from Sounding Rockets and Satellites

Thesis submitted for the degree of Philosophiae Doctor

Department of Physics
Faculty of Mathematics and Natural Sciences

University of Oslo

2024

Series of dissertations submitted to the
Faculty of Mathematics and Natural Sciences, University of Oslo
No. **2726**

ISSN **1501-7710**

Cover: UiO.
Print production: Graphic center, University of Oslo.

「 立ちはだかってる巨大な壁も、見方を変えたら大きな扉。」

工藤新一・名探偵コナン・青山剛昌[1]

[1]Translation: "From a different perspective, an imposing wall is just a large door."
Kudō Shin'ichi, Detective Conan, Aoyama Gōshō

Preface

This thesis is submitted for the degree of *Philosophiae Doctor* at the University of Oslo. The thesis comprises two papers focusing on the analysis of plasma structuring within the ionospheric cusp with in-situ measurements from sounding rockets. A third paper focuses on long-term statistics on plasma structuring within the high-latitude ionosphere. The three studies form the main pillar of this thesis. An introduction guides the reader into the topic of space weather and the importance of understanding the drivers for plasma structuring in the ionosphere. The following chapters lead up to the presentation of the papers and provide an introduction to the physical processes necessary for understanding the papers and for the instrumentation used in this work.
While the papers that are part of this thesis comprise a varying number of co-authors, I was responsible for writing the manuscripts and conducting the research done for each of them. I would like to thank all co-authors for their invaluable discussions about the findings and their feedback provided to the manuscripts.

Acknowledgements

First and foremost I would like to thank my main supervisor Wojciech Miloch for the possibility to conduct this research and the invaluable guidance through the last three years. Thank you for always supporting whatever idea I came up with and for helping me execute them in the end. I would also like to extend this gratitude to my co-supervisors Lasse Clausen, Andres Spicher and Sigvald Marholm. Their invaluable discussions, guidance and scientific insights have made it possible that I am able to write this thesis as it is right now. Thank you very much.
I would also like to thank the entirety of the 4DSpace group for the nice chats within the lunch break, the opportunity to gather for waffles every month and generally the great time spent together. A special thank you goes out Magnus Ivarsen for the countless helpful discussions, and explanations of code and the grand mysteries of the ionosphere. Special gratitude also goes to Yaqi Jin for the innumerable help and discussion and providing plots for the third paper. Special thanks go to Daria Kotova for the scientific discussions and always lending an ear when I had questions. Moreover, I would like to thank the engineers of this group, Bjørn Lybekk and Espen Trondsen. Special gratitude to Pascal Sado, Florine Enengl and Anna Piterskaya, my fellow PhD-students-in-crime for the great time, discussions, knitting breaks, and get-togethers. This is fine. It truly is.

I would like to thank Yoshifumi Saito for providing me with the opportunity to spend three months at JAXA ISAS in order to analyse the data from the SS-520-3 sounding rocket. My time at JAXA was incomparably wonderful, and helped me tremendously in further finding my path going forward from here. With that I would also like to thank Milla and Ralf for the great time at JAXA, helping me understand Japan in a better way, the great conversations over lunch or even greater ones in the pub, if we did not get flooded away in Machida while on our way there. I would also like to thank Iris and Susan for making my stay in Japan something I remember very fondly, and for being great friends even after we all came back. Japan would not have been the same without you.
Within the same scope I would like to thank Katie Herlingshaw, whom I have first met at JpGU this year, and who has since encouraged me to keep the writing up with daily tomato sessions. I say tomayto, you say tomahto.
I would also like to thank my former Master thesis supervisor Åshild Fredriksen who has encouraged me to pursue a PhD and was also always there for me when questions came up during the PhD.
A thesis is never mastered alone, but besides all the scientific and academic contributions over the years, a special thank you goes out to my parents Regina and Alfred who have always supported me in my decisions to further pursue my studies and in moving abroad in order to pursue a master's degree in space physics in Norway. Special thanks also to Reinhold, who was always interested in my studies and stories and who has supported me within all my decisions as well. Thank you for everything, I love all of you dearly.
It is likely possible to thank a vast variety of people for leaving an imprint on my life that lead to the writing of this thesis, but I would like to express my sincerest appreciation to my Alaskan family Julene, Kaitlyn and Shelby, whom I stayed with already over a decade ago, but who have shaped my love of the north and specifically the northern lights immensely. I would not be who and where I am now without you. Thank you so much for that.
I would also like to express gratitude to my friends who have supported me along the way, especially Julia and Desmond (and again Pascal) who have been there since the beginning of my studies and have stuck around through three theses, several international moves, the development of too much love for coffee, and overall over ten years of friendship. Der SUV fährt total geschaffte Physiker heim. Oink Oink!
Gratitude goes also out to Marthe and Reynir, who have grown to some of my closest friends since moving to Norway and who have supported me within the last months while finishing up this work. Thank you for being you.
Last but not least, thank you to Bruce and the Squad^{TM} for providing the best coffee and mental support Norway has to offer.
Very last but not least, thank you to Julia and Desmond for the proofreading done within this manuscript, to Reynir for proofreading the Norwegian abstract, and to Iris for spellchecking the Japanese quote.

Lisa M. Buschmann
Oslo, February 2024

Abstract

This dissertation focuses on investigating plasma structures within different regions and altitudes in the polar ionosphere. The data used in **Paper I** and **Paper III** comprises in-situ measurements from sounding rockets in the polar cap and cusp, and a distinction between structuring in regions with and without particle precipitation is made. Spectral analysis of high-cadence electron density measurements allows an insight into density variations on a variety of scale sizes, and it is investigated whether the spectra in different regions undergo steepening. In-situ measurements of particle precipitation provide the location of the cusp and provide a way to distinguish structures within and outside the cusp. The in-situ measurements are further supported by ground-based and satellite data, providing information on e.g. the electron temperature, ion drift velocities and scintillation indices.

Paper I shows an increase in structuring at hundred meter to kilometer scales is observed when the rocket is located within the cusp. An increase in energy within these scale sizes lifts the corresponding frequency part of power spectral density within this region, which favours an onset of spectral steepening in the cusp and just poleward of the cusp. These findings are verified in **Paper III** by comparing structures in- and outside of the cusp at similar altitudes.

These plasma structures convecting from the cusp into the polar cap can then be further broken down as indicated by an increase in energy at meter-scales.

Paper II shows long-term statistical studies of the polar ionosphere and provides an interhemispheric, seasonal climatology of the electron density and field-aligned magnetic field at kilometer-scales. We observe seasonal variations in electron density structuring at these scales, with density structuring peaking around the equinoxes, and large interhemispheric variations within. Analysis of the B_y magnetic field data indicates an increase of the Poynting flux associated with the Alfvénic energy into the cusp, for all seasons and both hemispheres, with enhancements in local summer.

Sammendrag

Denne avhandlingen fokuserer på å undersøke plasmastrukturer i ulike regioner og høyder i den polare ionosfæren. Dataene som brukes i **Paper I** og **Paper III** består av in-situ målinger fra sonderaketter i polar cap og polar cusp, og det skilles mellom strukturering i regioner med og uten partikkelnedbør. Spektralanalyse av målinger av elektrontetthet med høy kadens gir et innblikk i tetthetsvariasjoner på ulike skalastørrelser, og det undersøkes om spektrene i ulike regioner blir brattere. In-situ-målinger av partikkelutfelling viser plasseringen av cuspen og gjør det mulig å skille mellom strukturer innenfor og utenfor cuspen. In-situ målingene støttes også av bakkebaserte data og satellittdata som gir informasjon om blant annet elektrontemperatur, ionedrifthastigheter og scintillasjonsindekser.
Paper I viser at det observeres en økning i strukturering på hundre meters til kilometers skala når raketten befinner seg innenfor cuspen. En økning i energien innenfor disse skalastørrelsene løfter den tilsvarende frekvensdelen av effektspektraltettheten i dette området, noe som bidrar til at spektret blir brattere i cuspen og like ved polen av cuspen. Disse funnene blir verifisert i **Paper III** ved å sammenligne strukturer i og utenfor cuspen i lignende høyder. Disse plasmastrukturene som konvekterer fra cuspen og inn i polar cap, kan deretter brytes ytterligere ned, noe som indikeres av en økning i energi på meterskala.
Paper II viser langsiktige statistiske studier av den polare ionosfæren og gir en interhemisfærisk, sesongmessig klimatologi for elektrontetthet og feltjustert magnetfelt på kilometerskala. Vi observerer sesongvariasjoner i elektrontetthetsstruktureringen på disse skalaene, med tetthetsstrukturering som topper seg rundt jevndøgn, og store interhemisfæriske variasjoner innenfor. Analyse av B_y-magnetfeltdataene indikerer en økning av Poynting-fluksen knyttet til Alfvén-energien inn i cuspen, for alle årstider og begge halvkuler, med forsterkninger om sommeren.

List of Papers

List of Papers Included in this Dissertation

Paper I

Buschmann, L.M., Bonnell, J.W., Bounds, S., Clausen, L.B.N., Kletzing C., Marholm, S., Miloch W.J., Roglans, R. and Spicher, A. 'The role of particle precipitation on plasma structuring at different altitudes by in-situ measurements'. In: *Journal of Space Weather and Space Climate*. Vol. 13, no. 13 (2023), Topical Issue - Ionospheric plasma irregularities and their impact on radio systems. DOI: 10.1051/swsc/2023012.

Paper II

Buschmann, L.M., Clausen, L.B.N., Spicher, A., Ivarsen, M.F. and Miloch, W.J 'Statistical Studies of Plasma Structuring in the Auroral Ionosphere by the Swarm Satellites'. In: *Journal of Geophysical Research: Space Physics*. Vol. 129, no. 2 (2024) DOI: 10.1029/2023JA032097.

Paper III

Buschmann, L.M., Asamura, K., Clausen, L.B.N., Jin, Y., Kumamoto, A., Ogawa, Y., Oksavik, K., Saito, Y., Spicher, A., Yokota, S. and Miloch, W.J. 'Plasma structuring within an expanded active cusp region studied with the SS-520-3 sounding rocket'. *Submitted for publication in Earth, Planets and Space*

List of Papers not Included in this Dissertation

Paper IV

Buschmann, L.M. and Fredriksen, Å. 'Axial and radial development of the hot electron distribution in a helicon plasma source, measured by a retarding field energy analyzer (RFEA)'. *Plasma Sources Science and Technology.* Vol. 31, no. 2, (2022), DOI: 10.1088/1361-6595/ac47e5.

Contents

Chapter 1

Introduction

Space Weather is the physical and phenomenological state of natural space environments. The associated discipline aims, through observation, monitoring, analysis and modelling, at understanding and predicting the state of the Sun, the interplanetary and planetary environments, and the solar and non-solar driven perturbations that affect them, and also at forecasting and nowcasting the potential impacts on biological and technological systems.

COST Action 724
Lilensten and Belehaki, 2009

Space weather affects life on Earth in a variety of different ways. One of the arguably most well-known and recognizable space weather effects are the auroras (aurora borealis and aurora australis for the northern and for the southern hemisphere, respectively). A picture of the nightside aurora borealis can be seen in figure 1.1.

Figure 1.1: Aurora Borealis, photo taken by L.M. Buschmann at Gálggojávri, Northern Norway on 2020-03-01.

When the solar wind, a stream of plasma, reaches the Earth's magnetic field, the interplanetary magnetic field (IMF) frozen-in within the solar wind and the terrestrial magnetic field can connect with each other. This process, also called dayside reconnection, creates a pair of open field lines consisting of the IMF and the terrestrial magnetic field. These open field lines are then dragged over the polar regions towards the night side of the Earth, where they can yet again reconnect (Dungey 1961). The solar wind plasma is thus granted an entryway into the confinements of the Earth's magnetic field, and energetic particles can protrude into the ionosphere and concurrently create the aurora.
Other maybe less known but just as important effects of space weather include for example spacecraft charging, drag on spacecrafts in low Earth orbits[1], and the degradation of trans-ionospheric radio waves, for example in Global Navigation Satellite System (GNSS) positioning services. Structures in the plasma density on the scale of hundreds of meters to several kilometers are known to cause rapid fluctuations in the amplitude and phase of radio signals (Jin, J. I. Moen, Oksavik et al. 2017; Kintner, Ledvina and De Paula 2007). These disturbances are also known as scintillations and can cause faulty positioning and signal tracking error, also known as loss of lock (H. C. Carlson et al. 2007; Kintner, Ledvina and De Paula 2007; Yeh and C.-H. Liu 1982). In recent years, human activity has increased in the polar regions, making accurate positioning for aviation and marine services necessary. Thus, increased research has been conducted on the formation of irregularities within ionospheric plasma at high-latitudes and the connection to enhanced scintillation indices (Jin, J. I. Moen and W. J. Miloch 2014; Kintner, Ledvina and De Paula 2007; Oksavik, J. Moen, Lester et al. 2012), but these effects are still not understood to their full extend.
It is of importance to further understand plasma structuring and the drivers that trigger the redistribution of energies in the high-latitude ionosphere, and an overarching research goal is to develop and improve forecasting and space weather models.
Free energy injected into the high-latitude plasma can trigger an onset of instabilities, which can then further structure the plasma on a variety of different scales (Tsunoda 1988). One of the main sources of free energy is the precipitation of energetic electrons and ions (Dyson and Winningham 1974). Particles can either enter the ionosphere gyrating alongside the magnetic field lines until they gain sufficient energy to overcome the magnetic bottle confinement in the terrestrial magnetic field (Kivelson and C. T. Russell 1995). Alternatively, they can also enter the ionosphere directly through a funnel-shaped opening in between the open and closed fieldlines on the dayside of the Earth, also called the cusp (J. Moen, D. Evans et al. 1996; Oksavik, Søraas et al. 2000). Precipitation into the cusp is usually soft, meaning generally of lower energy (of few 100s of eV) in comparison to precipitation of particles on the nightside. The response in the ionosphere thus occurs at different altitudes depending on the

[1] e.g., in February 2022 a geomagnetic storm lead to an enhanced neutral density within the ionosphere, causing the loss of 38 out of 49 of SpaceX's Starlink satellites (Berger et al. 2023; Fang et al. 2022; Ray et al. 2022)

energy of the precipitating particles.
Solar extreme ultraviolet (EUV) radiation can enhance the plasma density in the dayside ionosphere. This plasma can convect over the polar regions, where it is susceptible to a variety of instabilities, e.g the Kelvin-Helmholtz or Gradient-Drift instabilities, which can further structure the plasma (S. Basu, S. Basu, MacKenzie et al. 1990; H. C. Carlson 2012; H. C. Carlson et al. 2007; Hosokawa, Taguchi et al. 2013; M. J. Keskinen and Ossakow 1983; Kintner and Seyler 1985; J. Moen, Oksavik, Abe et al. 2012; Tsunoda 1988).
One method to access information about instabilities and structuring in the ionosphere is through spectral analysis (Kintner and Seyler 1985). Measurements of the ionosphere have shown that irregularities in the plasma density follow power laws, and that spectral steepening occurs at higher frequencies, as can be observed if the Fourier-transformed density is plotted on log-log axes (Di Mare et al. 2021; Hysell et al. 1994; Ivarsen, Jin et al. 2019; Ivarsen, St-Maurice et al. 2021; Jahn and LaBelle 1998; M. C. Kelley et al. 1982; Kintner and Seyler 1985; LaBelle, M. C. Kelley and Seyler 1986; Spicher, W. Miloch and J. Moen 2014; Tsunoda 1988; Villain, Hanuise and Beghin 1986). Spectral steepening in this work refers to two fits in a power spectral density (PSD) plot on log-log-axes (in all papers within this thesis also referred to as a Double Slope (DS)).

This thesis aims to provide a better understanding of how the energy input into ionospheric plasma in the polar regions is affecting the formation of irregularities that restructures the plasma density, throughout this thesis also referred to as plasma structuring. **Paper I** and **Paper III** focus mainly on plasma irregularities in the cusp, as the sounding rockets described were launched into an active cusp. The cusp is a highly dynamic region on the dayside where a variety of drivers can lead to plasma structuring. Flow shears and particle precipitation into the cusp can lead to the formation of plasma density irregularities on scale sizes linked to the occurrence of enhanced scintillation indices (B. Basu and Coppi 1988; S. Basu, S. Basu, Chaturvedi et al. 1994; L. Clausen et al. 2016; Fæhn Follestad et al. 2020; Jin, J. I. Moen and W. J. Miloch 2015; Kinrade, C. N. Mitchell et al. 2013; Oksavik, J. Moen, Rekaa et al. 2011; Oksavik, Meeren et al. 2015; Rinne et al. 2007; Spicher, Deshpande et al. 2020). It is thus of importance to conduct further research on plasma structuring within the polar cusp ionosphere. In order to conduct the research, we utilize in-situ measurements from sounding rockets and several years of data from the European Space Agency's (ESA) Swarm satellite constellation to carry out long-term statistics.
The rocket in-situ measurements provide high-cadence data of the electron density, and the main analysis method comprises power spectral density analysis of the data sets. Spectral analysis provides a possibility to access information about spectral steepening, and additionally a measure of energy in a range of scale-sizes and how prominent structures of certain sizes are within the ionosphere. In addition to the density data, we further use a range of supporting instrumentation. Data of precipitating electrons and ions on board of the sounding rockets allow us to distinguish between regions with and without particle precipitation.

It further gives us an indication of when the rockets are flying through the cusp. Magnetic field and field-aligned current data are used to analyze the fluctuations in the field-aligned currents, and we further utilize electric field data to analyze the plasma flow. Supplementary to the in-situ measurements we also use data from All-Sky Imagers, scintillation receivers, the European Incoherent Scatter (EISCAT) Svalbard radar, OMNI solar wind data and TEC maps obtained from the Madrigal database. The All-Sky Imagers provide pictures of the aurora for additional information in **Paper I**. The remaining instruments were all used within the scope of **Paper III**. Scintillation receivers and TEC maps provide an additional set of data giving insights on density structures, as they are not based on in-situ measurements. EISCAT data gives insight on the electron density and temperature, and ion temperature and flow speeds along the line-of-sight of the radar. OMNI data is used to obtain information on the solar wind conditions in a window of several days around the rocket launch.

Paper I and **Paper III** provide a high cadence analysis of the electron density within the cusp ionosphere from in-situ measurements obtained from sounding rockets. Spectral analysis of the electron densities gives an insight on plasma structures at meter to kilometer scales. **Paper III** provides observations of high cadence electron density measurements within three different types of structures: polar cap patches, cusp patches and a newly formed tongue-of-ionization. Furthermore, due to the simultaneous launch of two sounding rockets which were analysed in **Paper I**, we were able to compare differences in plasma structures at different altitudes.
Paper II presents a long-term statistical spectral density analysis obtained from electron density and B_y magnetic field data and thus provides an interhemispheric, seasonal climatology of km-scale structures of these quantities. Seasonal variations in the electron density fluctuations are observed, with stronger enhancements within km-scale density structures around the equinoxes. The same results further strongly varied when comparing the northern and southern hemisphere, likely due to the asymmetry in the magnetic field. Analysis of spectral steepening corroborates on earlier studies found in Ivarsen, St-Maurice et al. 2021, showing a higher probability for spectral steepening in local summer, due to the influence of solar EUV radiation on the dissipation of ionospheric instabilities. Fluctuations within the magnetic field indicate variations in the Poynting flux on scales below 10 km (D. Knudsen, M. Kelley and J. Vickrey 1992). The Alfvénic energy associated with the Poynting flux on these scales can also function as a source of free energy into the ionosphere.

Chapter 2

Physical Background

2.1 Plasma Drifts

A plasma is a partially or fully ionized, quasi-neutral gas that exhibits collective behaviour (Chen 2012). This entails amongst other principles that on average the amount of negative and positive charges are equal when observed at large scales. The movement of charged particles has been described on several occasions, e.g, in Chen 2012 and Kivelson and C. T. Russell 1995, and a short summary shall be given in this section. Charged particles are generally subject to the Lorentz force in the presence of electric and magnetic fields ($\boldsymbol{E}$ and $\boldsymbol{B}$, respectively), as given by

$$m\frac{\mathrm{d}\boldsymbol{v}}{\mathrm{d}t} = q(\boldsymbol{E} + \boldsymbol{v} \times \boldsymbol{B}) \tag{2.1}$$

where m, v and q are the particle mass, velocity and charge, respectively. In the simplest case when neglecting the electric field, the particles undergo a simple gyration motion around the magnetic field lines at a cyclotron frequency ω_c given by

$$\omega_\mathrm{c} = \frac{qB}{m} \tag{2.2}$$

The corresponding gyration radius, also called Larmor radius r_L is then given by

$$r_\mathrm{L} = \frac{v_\perp}{\omega_\mathrm{c}} = \frac{mv_\perp}{qB} \tag{2.3}$$

When the electric field cannot be omitted anymore, the particles additionally start drifting in the $\boldsymbol{E} \times \boldsymbol{B}$ direction. Assuming a constant electric field $\boldsymbol{E}$, and a magnetic field in z-direction $\boldsymbol{B} = B\hat{\boldsymbol{z}}$, equation 2.1 can be solved to yield

$$\begin{aligned} v_x &= v_\perp \exp(i\omega_\mathrm{c}t) + \frac{E_y}{B} \\ v_y &= iv_\perp \exp(i\omega_\mathrm{c}t) + \frac{E_x}{B} \end{aligned} \tag{2.4}$$

These equations can then be generalized to obtain the $\boldsymbol{E} \times \boldsymbol{B}$-drift

$$\boldsymbol{v}_{\boldsymbol{E}\times\boldsymbol{B}} = \frac{\boldsymbol{E} \times \boldsymbol{B}}{B^2} \tag{2.5}$$

It can be seen at once that the drift is independent of particle charge, and thus both positive and negative charges drift in the same direction. This equation can be further generalized by replacing $\boldsymbol{F} = q\boldsymbol{E}$ with another force. In the presence of a non-uniform magnetic field $\nabla\boldsymbol{B} \perp \boldsymbol{B}$, we thus obtain the Gradient-B drift $\boldsymbol{v}_{\nabla B}$:

$$\boldsymbol{v}_{\nabla B} = \pm\frac{1}{2}v_\perp r_L \frac{\boldsymbol{B} \times \nabla B}{B^2} \tag{2.6}$$

In a curved magnetic field, however, the particle will further be susceptible to the centripetal force, which leads to the curvature drift $\boldsymbol{v}_c$

$$\boldsymbol{v}_c = \frac{mv_\parallel^2}{qB^2}\frac{\boldsymbol{R_c} \times \boldsymbol{B}}{R_c^2} \tag{2.7}$$

where $\boldsymbol{R_c}/R_c = R_c\hat{\boldsymbol{r}}$ with constant radius of curvature R_c. In comparison to the $\boldsymbol{E} \times \boldsymbol{B}$ drift, both the curvature and ∇B drift are dependent on charge, and thus positive and negative charges will drift in opposite directions. Particles within the Earth's magnetic field configuration will be subject to both curved magnetic fields with varying field strength and electric fields. The implications will be further elaborated in the following sections.

2.2 Sun-Earth Interaction

The impact of the solar wind on the Earth's polar ionosphere is substantial.
The solar wind carries the IMF in addition to plasma emitted from the Sun's corona.
When the IMF reaches the Earth's magnetic field, the two may interact, and the terrestrial magnetic field becomes compressed on the day side, as a result of the solar wind impact. The night side magnetic field, however, stretches out away from the Sun, and can reach a distance of several hundred Earth radii (Kivelson and C. T. Russell 1995). This description, however, is a very simplistic portrayal, as the interaction between the solar wind and the Earth's magnetic field is in reality rather complex.
If the IMF contains a southward component, it can reconnect with the terrestrial, northward pointing field in a process called dayside reconnection. The newly opened fieldlines can then convect over the polar regions towards the nightside, taking electrons and ions from within the solar wind along. On the nightside of the Earth, in the magnetotail, the fieldlines can yet again reconnect in a process called nightside reconnection. As a result, the charged particles following along the convecting magnetic field lines are being trapped in the now closed magnetic field configuration of the Earth. The reconnected field lines convect once again towards the dayside of the Earth. This process is called the Dungey cycle and was first proposed by Dungey 1961, a schematic can be seen in figure 2.1. The right hand side of the top figure shows the ionospheric convection, illustrating the movement of the field line footprints over the polar regions.

2.3 High Latitude Ionosphere and the Aurora

The Earth's ionosphere is a plasma containing region above approximately 80 km in altitude and is mostly embedded into the thermosphere, a layer of the Earth's atmosphere reaching between 100 and 1000 km in altitude. In addition to coupling to the thermosphere, the ionosphere is altered by the interaction of the solar wind and the magnetosphere. It is thus heavily influenced by

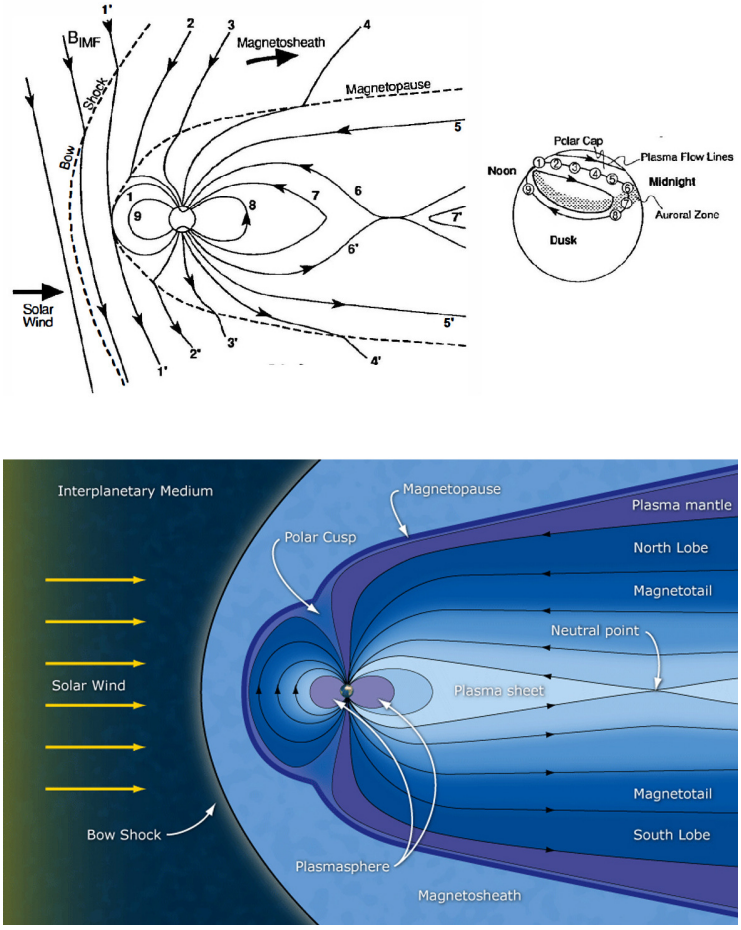

Figure 2.1: Upper panel: Schematic of the polar convection cycle (Dungey cycle) driven by magnetic reconnection. [1] - The IMF connects with the Earth's magnetic field, creating a pair of open field lines. [2-5] - The open field lines get dragged across the polar caps into the night side, where they can reconnect in [6]. The closed field lines then return to the dayside along the edge of the polar cap [7-9]. The footprints of the field lines form a convection cell as seen in the right sub-figure of this image. Obtained and rearranged for better visibility from Kivelson and C. T. Russell 1995. Lower panel: Schematic of the Earth's magnetosphere, obtained from ESA and C. Russell 2023-12-02.

magnetosphere-ionosphere-thermosphere (MIT) coupling. The processes occurring in the high-latitude ionosphere are vast and complex. The following section focuses on describing phenomena relevant for this dissertation, including, among others, M-I-T coupling, plasma motion, plasma structuring, and ionospheric current systems.

2.3.1 The Continuity Equation and M-I-T Coupling

The production, losses and transport of plasma in the ionosphere have been discussed in great detail in a variety of different works, for example in Brekke 2012, J. F. Vickrey and M. C. Kelley 1982 and Nishimura et al. 2021. The following subsection aims to give an overview of the different mechanisms, and, to avoid cluttering, will not refer to these citations until the beginning of the next subsection.
The ionosphere is divided into three regions, the D-region, E-region, and F-region (Kivelson and C. T. Russell 1995). The D-region is the lowest region, located below approximately 90 km. The E-region spans altitudes between approximately 90 and 130 km, while the F-region protrudes upwards of roughly 130 km. The F-region is further characterized by two peaks in ionospheric density, called the F_1 and F_2 peaks. The characteristics of the peaks depend on a variety of different aspects. The thermosphere, which functions as a background for the ionosphere, has a significant impact on the ionosphere. The production, loss and transport is governed by the continuity equation. For ions it is given by

$$\frac{\partial n_i}{\partial t} = p_i - l_i - \Delta(\mathbf{v_i} n_i) \tag{2.8}$$

where n_i and $\mathbf{v_i}$ are the ion density and velocity, respectively, and p_i and l_i are the ion production and loss terms, respectively.
One of the production mechanisms is the ionization due to solar EUV radiation. The neutral density n of the atmosphere for a given height z is given by

$$n(z) = n_0 \exp(-z/H) \tag{2.9}$$

where H is the scale height, the height for which the atmospheric pressure has decreased by $1/e$ for some reference height z_0. It can be seen that the density decreases with rising altitude. Incoming solar radiation with a certain intensity $I(z)$ will thus ionize a number of neutral particles. As n decreases while I increases with altitude, a peak ionization altitude z_m will form, which is dependant on a variety of influences, e.g., the solar zenith angle (SZA). The resulting Chapman production profiles p for ionization above and below z_m are then given by

$$\begin{aligned} p &\approx p_m \exp(-z/H), && z >> z_m \\ p &= p_m \exp\left(-\sec\chi \, \exp\left(-\frac{z - z_m}{H}\right)\right), && z << z_m \end{aligned} \tag{2.10}$$

where χ is the SZA and p_m is the peak ionization at height z_m. The plasma density in the ionosphere is thus dependant on the influence of solar EUV radiation, which leads to diurnal and seasonal changes of the intensity and location of the F_1 and F_2 peaks. It has also been shown that the F-layer electron density depends on the 11-year solar cycle, with higher density during solar maximum (Jin, Spicher et al. 2019).
The plasma that has been formed through ionization immediately tries to reinstate the earlier existing equilibrium. In addition to transport mechanisms, which will be addressed shortly, a part of the ionization will be lost in recombination with neutrals. The composition of the ionosphere depends greatly on altitude. While the ionosphere mainly constitutes NO^+ and O_2^+ below 150 km in altitude, the F-region, above 150 km, consists mainly of O^+, though NO^+, O_2^+ are also present. Note, that these compositions can vary greatly with solar activity.
The two main recombination processes are radiative and dissociative recombination. The former describes the recombination of an ion and electron by forming a neutral under the emission of a photon

$$X^+ + e \rightarrow X + h\nu \tag{2.11}$$

while the latter describes the recombination of a molecule and an electron by forming two neutrals

$$XY^+ + e \rightarrow X + Y \tag{2.12}$$

Dissociative recombination occurs at a much faster rate. In the E-region, where NO^+ and O_2^+ are predominant, dissociative recombination forms the most important loss. In the F-region, where O^+ is more dominant, radiative recombination of atomic oxygen ions is more common, however, the process is slow and recombination takes place at a lesser pace. An additional dissociative recombination process in the F-region is $NO^+ + e \rightarrow N + O$. As the neutral density diminishes with rising altitudes, recombination plays a larger role in the E-region than it does in the F-region.
In addition to losses and production, the ionospheric plasma is also subject to transport. Density gradients in the plasma lead particles to drift to regions of lower density. This process is also known as diffusion. This drifting can be hindered by collisions with other particles along their way. The diffusion equation for a species j is given by

$$\frac{\partial n_j}{\partial t} - D_j \nabla^2 n_j = 0 \tag{2.13}$$

where $D_j = kT/m_j\nu_j$ is the diffusion coefficient, k is Boltzmann's constant, T_j, m_j, $\nu_j$and n_j are the species' temperature, mass, collisional frequency, and density, respectively.
In the vicinity of a magnetic field, particles are generally bound by the field lines and the direction of motion is thus pointed along the field. The diffusion coefficient along the magnetic field line is notwithstanding given by $D_{\parallel,j} = D_j = kT/m_j\nu_j$. Diffusion perpendicular to the magnetic field, however, is occurring at a lower rate and dependant on the gyrofrequency of the particle with

$D_{\perp,j} = kT_j\nu_j/m_j\omega_j^2$, where $\omega_j = qB/m_j$ is the gyrofrequency of the particles. This indicates that the cross-field diffusion, or diffusion perpendicular to the magnetic field is occurring $\propto 1/B^2$. It has, however, been shown that this is not the case, and that the cross-field diffusion is rather scaling with $1/B$. This diffusion is called Bohm diffusion.
As the ionospheric plasma is considered quasi-neutral, thus consisting of the same amount of negative and positive charges, the diffusion equation mainly depends on the difference in temperature, mass and collisional frequency. While all of these differ, the mass ratio between electrons and ions prevails, which subsequently leads to a higher D for ions, and consecutively leading to their faster diffusion. The ensuing charge separation forms an electric field, also known as the ambipolar field, which assimilates the diffusion rates of both species. This process is also known as ambipolar diffusion.
In addition to diffusion, particles can also be transported by e.g., electric fields or neutral winds.
This last subsection shows the intimate coupling between the ionosphere and the thermosphere, and how the composition of the thermosphere can influence the ionosphere and vice versa.
In addition to thermosphere-ionosphere coupling, as described in the first part of this subsection, the ionosphere is also intimately coupled to the magnetosphere. One implication is the impact of particle precipitation, energetic electrons and ions that can enter from the magnetosphere in different manners. Charged particles are bound to the magnetic field lines, and are undergoing a gyration motion as outlined in the previous section. Field lines in the vicinity of the Earth converge, and as a result, the magnetic field becomes stronger in these regions. Particles with insufficient kinetic energy will bounce back due to magnetic mirroring and are trapped within the magnetic field configuration (also known as magnetic-bottle confinement). These trapped particles are thus subject to an azimuthal drift stemming from the curvature drift and gradient-B drift. Positively charged particles are then drifting westward, while negatively charged particles are drifting towards the east. The resulting current around the Earth is called the ring current (Cowley 2000). Trapped particles can get scattered into the loss-cone in the vicinity of the Earth and subsequently precipitate into the ionosphere, where they can form the aurora. Typical wavelengths and colors of the aurora include green (557.7 nm) and red (630.0 nm) which stem from the excitation of atomic oxygen. Excitation of nitrogen leads to purple and blue hues.
Poleward of the auroral region the polar cap can be found. The polar cap is a region located within the open-closed field line boundary (OCB), and thus generally less dominated by particle precipitation.
Another region crucial to the understanding of this work is the polar cusp. As briefly mentioned in the introduction, the cusp is a funnel-like shape delimited by the OCB as seen in figure 2.1. Magnetosheath plasma thus has a direct access into the ionosphere and vice-versa. Moreover, as the cusp location is dependant on the OCB, it serves as a footprint of dayside reconnection. Thus, when reconnection occurs, the location of the cusp changes, dependant on the z-

and y-components of the IMF (Jin, Spicher et al. 2019).

2.3.2 Tongue-of-Ionization and Polar Cap Patches

The plasma on the dayside ionosphere is formed by solar EUV radiation. As a consequence, the dayside plasma is of a higher plasma density. The ionospheric convection cells can drag a tongue-like structure of high-density plasma from the dayside over the polar cap into the nightside. Due to the morphology of the structure, it is also called tongue-of-ionization (TOI) (Sato and Rourke 1964; Sato 1959). Due to the differential plasma velocity within the ionospheric convection cells, the TOI may have a different velocity than the background plasma. It has been shown that the TOI is associated with the formation of plasma irregularities (W. Knudsen 1974; Sato and Rourke 1964; Sato 1959) and that its trajectory is dependant on the IMF B_y (J. Moen, Qiu et al. 2008). The TOI can further be segmented by a variety of mechanisms, and among others particle precipitation, influence of dayside reconnection and flow shears have been proposed (L. B. N. Clausen and J. Moen 2015; Lockwood and Carlson Jr 1992; Milan, Lester and Yeoman 2002; J. Moen, H. Carlson et al. 2006; Sojka, Bowline and Schunk 1994; Q.-H. Zhang, B.-C. Zhang, R.-Y. Liu et al. 2011; Q.-H. Zhang, B.-C. Zhang, J. Moen et al. 2013). These, further segmented, convecting islands of high density plasma can be called polar cap patches (PCP) if they are located within the polar cap, the plasma density within the polar cap patch is at least two times that of the background density, and they have to horizontally span a few hundred to thousand kilometres (Crowley et al. 1996; Tsunoda 1988). PCP can have lifetimes of several hours (Hosokawa, J. Moen et al. 2011) and travel towards the nightside following the convection cells at speeds up to $1000\,\mathrm{km\,s^{-1}}$ (E. J. Weber et al. 1984; E. Weber et al. 1986), before they reach the auroral oval, a region around the geomagnetic poles equatorward of the polar cap. PCP within the auroral oval and the cusp are called auroral blobs and cusp patches, respectively (Jin, J. I. Moen, Oksavik et al. 2017).

2.3.3 Ionospheric Current Systems

The terrestrial magnetic field lines can carry enough charges to form field-aligned currents (FAC). These FAC, also called Birkeland currents, couple the magnetosphere and the Earth's ionosphere.
The large-scale FAC can be divided into Region 1 and Region 2 (R1 and R2) currents flowing in or out of the ionosphere (Iijima and Potemra 1976a; Iijima and Potemra 1976b). A schematic of the R1 and R2 FAC along with the Hall and Pedersen currents (described briefly later within this section) which comprise the ionospheric current system can be seen in figure 2.2. The R1 current pair is located at higher latitudes than the R2 current pair, and is flowing downward into the ionosphere in the dawn sector and upward out of the ionosphere in the dusk sector. The R2 currents flow in the opposite directions (Iijima and Potemra 1976b). The R1 and R2 currents further construct the boundary of the auroral oval, when mapped into the ionosphere. In addition to the R1 and

R2 current sheets, a third system is located at higher latitudes and allocated to the cusp region (Iijima and Potemra 1976a; Wilhjelm, Friis-Christensen and Potemra 1978). The cusp FAC are often located poleward and adjacent to the R1 current and additionally flow opposite to the R1 current (Iijima, Fujii et al. 1978). This can be seen in figure 2.3.
The R1 and R2 currents map into the magnetopause and the ring current, respectively.

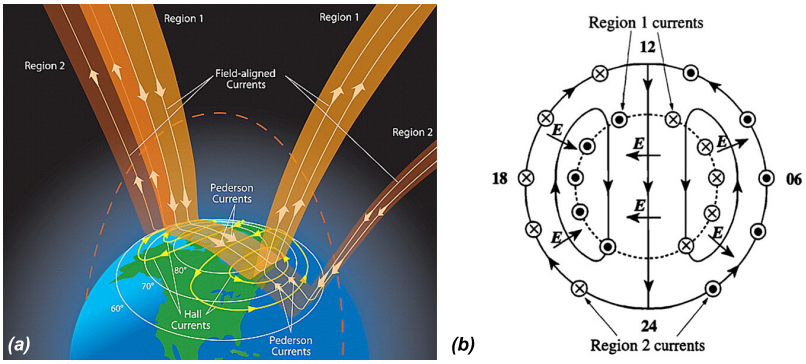

Figure 2.2: (a): an illustration of the ionospheric current systems, obtained from Le, Slavin and Strangeway 2010.
(b): A schematic of the ionospheric currents, the Pedersen current flows in the direction of $\boldsymbol{E}$, while the Hall current flow anti-parallel to $\boldsymbol{E} \times \boldsymbol{B}$, obtained from Cowley 2000.

Within the E-region, particles of the FAC can collide with neutrals due to the higher plasma density in the lower ionosphere. As a result of the difference in collision rates of ions and electrons, a charge separation ensues in directions along $\boldsymbol{E}$ and $\boldsymbol{E} \times \boldsymbol{B}$, resulting in the Pedersen and Hall currents, respectively, as indicated in figure 2.2b. The Pedersen current is closing the FAC within the ionosphere.

2.4 Ionospheric Instabilities

The ionospheric plasma is susceptible to a variety of macroscopic and microscopic instabilities. Macroscopic instabilities occur on large scale sizes, and are usually addressed in a fluid picture. Microscopic instabilities affect particles on an individual level, when the plasma cannot be seen as an entity anymore, and single particles and their distribution functions have to be addressed. Instabilities are a general mean of energy redistribution within a system in a non-equilibrium state, if a source of free energy is given (Treumann and Baumjohann 1997). In the following section, two of the major macroscopic instabilities that are believed to lead to restructuring of the plasma density in the ionosphere are discussed in further detail: The Gradient-Drift instability (GDI) and the Kelvin-Helmholtz

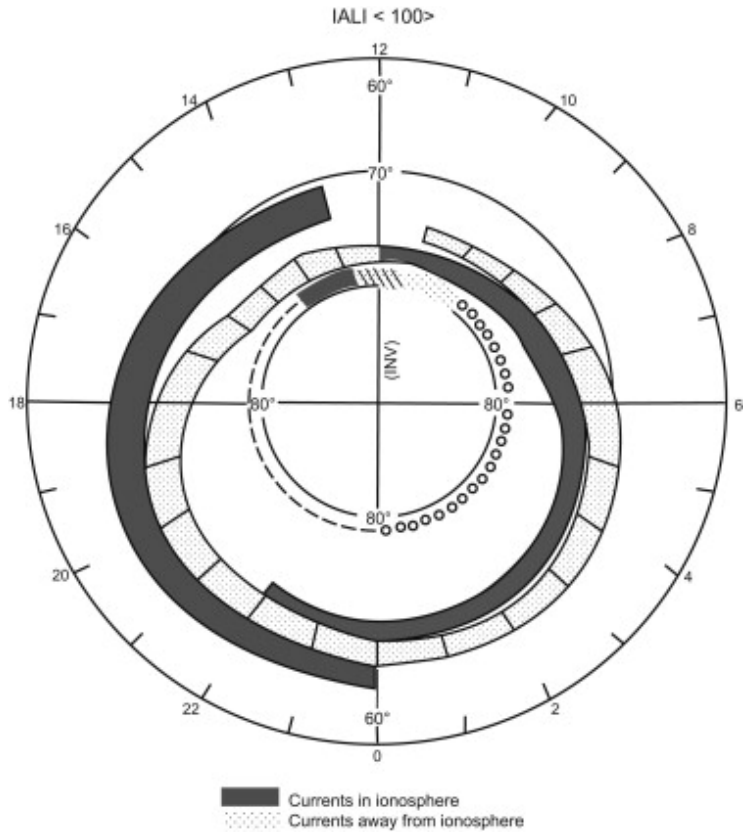

Figure 2.3: Pattern of the FAC, obtained from Triad (Iijima and Potemra 1976a). The dark grey regions indicate currents flowing into the ionosphere, while the dotted grey regions indicate currents flowing out of the ionosphere. The smaller regions found around 12 MLT indicate currents in and out of the cusp.

instability (KHI) (M. J. Keskinen and Ossakow 1983; M. Keskinen, H. Mitchell et al. 1988; Tsunoda 1988).

2.4.1 Gradient-Drift Instability

The Gradient-Drift instability (also named $\boldsymbol{E} \times \boldsymbol{B}$ drift instability (Tsunoda 1988)) acts on ionospheric density gradients, and thus can act on the trailing edges of convecting polar cap patches (Tsunoda 1988). A schematic depiction of the GDI can be seen in figure 2.4. Let the plasma have a density gradient in the x-direction, the electric field is directed towards y, while the magnetic field is pointing into the z-direction. When looked at closely, this resembles the field-configuration within the polar cap. An electric field is flowing from dawn to dusk (compare to figure 2.2b), while the terrestrial magnetic field is flowing

into the Earth. Polar cap patches which are then convecting from the dayside into the nightside provide a density gradient for the instability to act on. The electrons are generally highly magnetized as their gyrofrequency is higher than their collision frequency (Kivelson and C. T. Russell 1995). The ions, on the other hand, have higher collision frequency than gyrofrequency and can thus follow the electric field, leaving the electrons behind. In high-density regions, more ions move in the negative x-direction along E than in the lower density regions as seen in figure 2.4. If a sinusoidal perturbation is imposed onto the boundary, an imbalance of charges builds up on the boundaries, which induces a polarisation electric field $\boldsymbol{E}_\mathrm{P}$ due to a charge separation. The concurrent $\boldsymbol{E}_\mathrm{P} \times \boldsymbol{B}$-drift magnifies the perturbation, leading to a growth of the instability. Generally, an initial perturbation has to be present in order for an instability to grow.
In a different scenario where the density gradient proceeds into the opposite direction as previously discussed, more net charges are located below the boundary, leading to an $\boldsymbol{E}_\mathrm{P}$ in the opposite direction. The induced $\boldsymbol{E}_\mathrm{P} \times \boldsymbol{B}$-drift then dampens the perturbation. This entails the following implication: The leading edge of PCP is generally stabilized by the GDI, while the trailing edge of the PCP is subject to structuring due to the GDI.

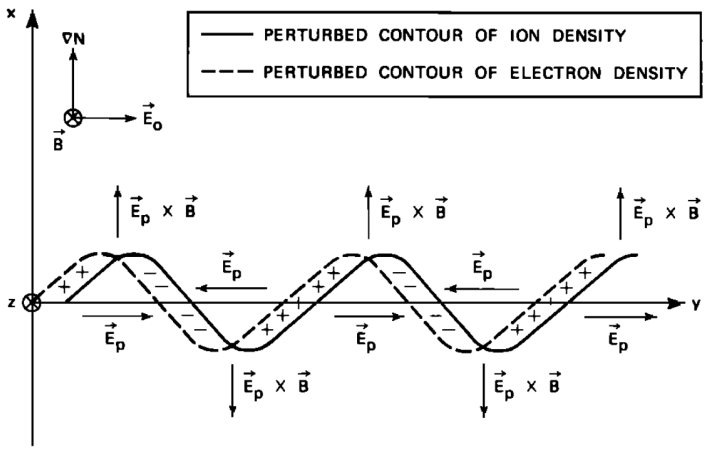

Figure 2.4: Schematic of the Gradient-Drift instability, obtained from Tsunoda 1988. The electric and magnetic fields are pointing in the y and z-direction, respectively. A density gradient is present along the positive x-direction.

2.4.2 Kelvin-Helmholtz Instability

The Kelvin-Helmholtz instability in a plasma is generated by the movement of plasma regions relative to each other in vicinity of a perpendicular magnetic field (M. Keskinen, H. Mitchell et al. 1988). Let there be a small perturbation at the

boundary between the two plasmas. As the plasma is moving, the perturbations lead to regions of enhanced and decreased plasma flow along the boundary, which will lead to a variety in pressure. The differences in flow and pressure can then further enhance the initial perturbations. Due to the movement of the plasma, these perturbations then get dragged along and form vortices, so called eddies. These eddies can reach scales down to the order of the ion gyroradius (Ganguli et al. 1994; M. Keskinen, H. Mitchell et al. 1988) and can furthermore exhibit strong density gradients. These may trigger an onset of other instabilities, like the GDI or microinstabilities. A schematic and simulation of the KHI forming between two plasmas of different densities can be seen in figure 2.5. The top panel, panel a, shows a schematic of the formation of the KHI due to a difference in flow velocities of the two plasmas. The bottom panel shows a simulation of two plasmas flowing in the same direction, however, with different flow speeds. The bottom panel, panel b, shows simulations of two plasmas flowing in the same direction at different velocities.
The KHI can occur in a variety of scenarios. Within auroral arcs, large perpendicular electric fields lead to strong $\boldsymbol{E} \times \boldsymbol{B}$ drifts. These can further induce strong polarization drifts that can drive the KHI (Treumann and Baumjohann 1997). Flow shears within the cusp have been proposed to trigger the KHI as well, leading to the formation of irregularities and concurrently to enhanced scintillation indices (B. Basu and Coppi 1988; S. Basu, S. Basu, Chaturvedi et al. 1994; Oksavik, J. Moen, Rekaa et al. 2011; Spicher, Deshpande et al. 2020). The KHI has also been discussed as an important mechanism in the formation of PCP (H. C. Carlson 2012; H. C. Carlson et al. 2007).
As the cusp and PC exhibit strong flow shears and density gradients for the KHI and GDI to act upon, they are good candidates for the formation of irregularities and structuring in these regions and are thus the main instability mechanisms focused on in this thesis.
H. C. Carlson et al. 2007 and Hosokawa, Shiokawa et al. 2009 studied patch formation and structuring in the northern hemisphere. They observed plasma structuring throughout the entirety of PCP which dictates another mechanism than the GDI, which solely affects the trailing edge of PCP. Furthermore, the time it takes for these patches to be thoroughly structured has been found to be too fast in order to be solely explained by the GDI alone. It was thus proposed that the KHI first pre-structures the plasma when entering the PC, as flow shears present at the boundary are sufficiently strong. The GDI can then act on the already structured plasma, further breaking it down to smaller scales, which was further supported by findings in J. Moen, Oksavik, Alfonsi et al. 2013.

2.4.3 Sources of Free Energy

As mentioned previously, the injection of free energy into a system can trigger a variety of instabilities. The last sections already touched upon the formation of irregularities through density gradients and flow shears. In this section the injection of free energy through precipitating particles, mainly by input of the

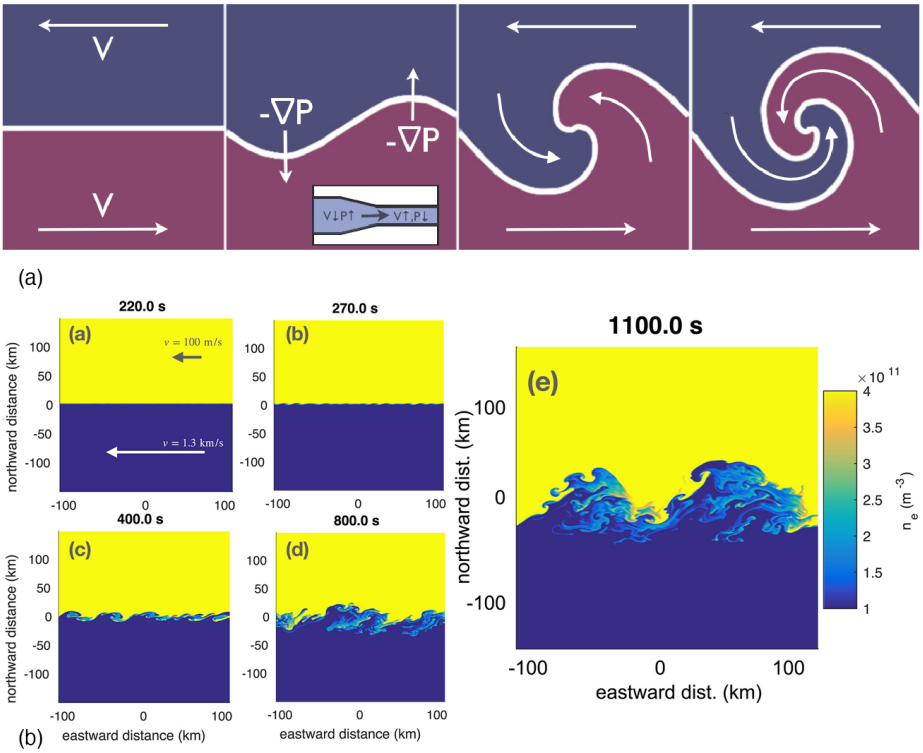

Figure 2.5: a: Schematic of the Kelvin-Helmholtz instability in a fluid. The fluid velocities are directed in opposite direction. Obtained from Gilbert 2017.
b: Simulations of the Kelvin-Helmholtz instability forming at the boundary between two plasmas of varying densities. The plasmas are flowing in the same direction, however, at different velocities. Obtained from Spicher, Deshpande et al. 2020.

Alfvénic energy, will be discussed.
The coupling between the magnetosphere and ionosphere provides the ionosphere with a variety of sources of free energy:

- The precipitation of high-energetic particles along the magnetic field lines, as discussed earlier, is giving rise to large scale irregularities within the F-region ionosphere (S. Basu, S. Basu, MacKenzie et al. 1990; M. C. Kelley et al. 1982; M. J. Keskinen and Ossakow 1983; Tsunoda 1988);
- Softer particle precipitation (100s of eV) from the magnetosheath into the cusp can lead to the formation of large scale structures with long lifetimes (M. C. Kelley et al. 1982; J. Moen, Oksavik, Alfonsi et al. 2013).

Filamentary particle precipitation into the cusp has further been linked to the formation of plasma structures on scale sizes responsible for strong scintillations, rapid fluctuations in the amplitude and phase of trans-ionospheric radio waves, causing errors in satellite positioning systems (L. Clausen et al. 2016; Fæhn Follestad et al. 2020; Jin, J. I. Moen and W. J. Miloch 2015; Kinrade, C. Mitchell et al. 2012; Kinrade, C. N. Mitchell et al. 2013; Oksavik, Meeren et al. 2015);

- Large-scale, quasi-static field-aligned currents (Cowley 2000; Iijima and Potemra 1976a) associated with large scale variations within the Poynting flux;

- Energetic electrons accelerated by the Alfvén waves connected to small scale fluctuations within the Poynting flux (Goertz and Boswell 1979; Hasegawa 1976; D. Knudsen, M. Kelley and J. Vickrey 1992). Alfvén waves are magneto-hydrodynamic waves propagating parallel to and thus along magnetic field lines. The Alfvén velocity is proportional to the magnetic field strength, indicating faster speeds in stronger fields (Chen 2012).

The Poynting flux $\boldsymbol{P}$ describes the energy transfer rate through an area in an electromagnetic field (Ivarsen, Park et al. 2020). For high-latitudes (poleward of 60°) it is given by the surface integral (M. Kelley, D. Knudsen and J. Vickrey 1991)

$$\boldsymbol{P} = -\frac{1}{\mu_0} \int \int_S (\boldsymbol{E}_\perp \times \partial \boldsymbol{B}_\perp) \cdot \hat{\boldsymbol{s}} \tag{2.14}$$

where S is the surface area where the Poynting flux flows through, $\boldsymbol{E}_\perp$ describes the electric field perpendicular to S, $\partial \boldsymbol{B}_\perp$ gives the magnetic field perturbation due to FAC, and μ_0 is the vacuum permeability. As $\hat{\boldsymbol{s}}$ is the unit magnetic field vector parallel to the magnetic field, $\boldsymbol{P}$ will also be field-aligned. The Poynting flux is caused by the variations in electric field and, as outlined before, can be divided into two scales: large-scale variations (>10 km) and small scale variations. **Paper II** analyses variations in the FAC below 10 km, and thus we will focus on fluctuations of these scale sizes.
Small scale fluctuations in FAC have been shown to be linked to the input of Alfvénic energy. Alfvén waves are known to travel along the terrestrial magnetic field, and as their velocity increases with the magnetic field strength (Chen 2012), they get accelerated in the vicinity of the Earth, where the terrestrial magnetic field converges. At the same time, as discussed priorly, particles decelerate due to the magnetic bottle confinement. When, however, the Alfvén speed exceeds the electron thermal velocity, these electrons can essentially be accelerated due to Landau damping[1] and gain sufficient energy to precipitate into the ionosphere (Schroeder et al. 2021). Small scale fluctuations within the FAC can thus be direct

[1]Particles with similar, slightly lower phase velocities than that of a wave can effectively gain energy from the wave by getting pushed alongside said wave. The wave concurrently loses energy and transfers it to the particle. This mechanism is called Landau damping (Chen 2012).

indicators for an onset of energetic electron precipitation, and measurements of Alfvén wave Poynting flux have been linked to accelerated electrons in the aurora (Chaston, J. Bonnell et al. 2003; Chaston, C. Carlson et al. 2007; Keiling et al. 2003).

2.4.4 Energy Cascade

As outlined previously, the plasma in the high-latitude ionosphere is susceptible to instabilities causing plasma density structures on a variety of scale sizes (M. C. Kelley 2009). In order to understand the formation of plasma structures in the ionosphere, it is important to identify the scales of plasma structures, and how these structures are linked and interact with each other.
Generally, a plasma, when examined at large scales, can be characterized by fluid theory. It has thus been suggested that the plasma in the high-latitude ionosphere can be described by fluid-like turbulence (Kintner and Seyler 1985). The general idea for the cascading of energy is that energy is being injected into a system, in this case the ionospheric plasma, at large scales. Instabilities are then able to act on these large scale structures and further break them down into smaller structures until the energy is dissipated at the smallest scales (Frisch and Kolmogorov 1995; Kolmogorov 1941). A schematic of such an energy cascade and Kolmogorov's 5/3-law can be seen in figure 2.6 a. The 5/3-law suggests that the different scales are interacting with each other and that energy is decreasing from larger to smaller scales with a constant slope of $p = -5/3$.

Kolmogorov's energy cascading is based on 3D turbulence in fluids. Under certain conditions, for example in large scale meteorological flows and electrostatic plasmas in strong magnetic fields, 2D turbulence can be applied instead (Kintner and Seyler 1985; Kraichnan 1967). In addition to the cascading of energy per unit mass which is also described in Kolmogorov's theory, another invariant has to be taken into account: the square vorticity, also called enstrophy, which is the kinetic energy stored in vertices in fluid turbulence (Kraichnan 1967). Kraichnan 1967 and Kintner and Seyler 1985 have further suggested that the energy is then injected into the system at a frequency where both regimes meet, and where the initial spectral slope steepens, from now on referred to as the spectral break point, or spectral break frequency. The energy per unit mass is cascading to higher powers, from the injection frequency to lower frequencies. As the energy is thus cascading 'upwards', the cascade is also called inverse cascade. The enstrophy on the other hand is cascading from the spectral break frequency to larger frequencies, which is also called a direct cascade.
One method to access information on turbulence in plasma is through the use of spectral analysis. Thus, plasma instabilities in the ionosphere have been suggested to be described by power laws, where power spectral density (PSD) analysis is used to describe a cascading of energy through a variety of scales (Frisch and Kolmogorov 1995; Kintner and Seyler 1985; Tsunoda 1988). PSD analysis provides a Fourier analysis of a time series, and thus a measure of the energy, or intensity of fluctuations, at a given frequency.
Two different PSD plots obtained from two seconds of electron density data used

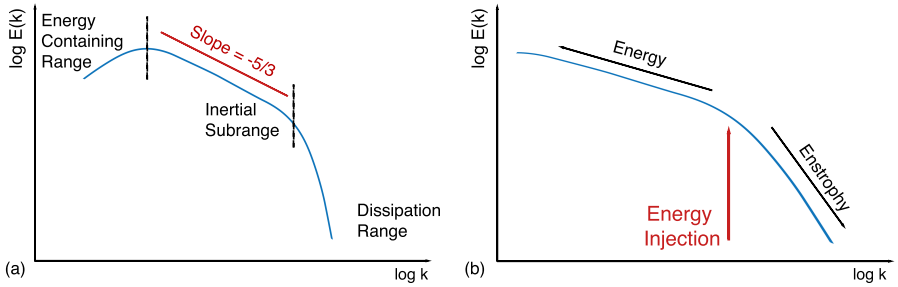

Figure 2.6: (a): Schematic of Kolmogorov's 5/3 – law of 3D turbulence. The graph can be divided into three regions: The energy containing range, where energy is injected at large scales; the inertial subrange, in which the energy is redistributed to smaller scales, and the dissipation region, in which the energy is dissipated into the background plasma. The energy decreases from small to large frequencies with a constant slope of -5/3, before the energy dissipates at high frequencies, or small spatial scales.
(b): Schematic of the energy cascade of 2D turbulence. The energy injection occurs at the spectral break frequency. The energy per unit mass is then cascading upwards in a so-called inverse cascade, while the square vorticity, the enstrophy, is cascading directly (Kintner and Seyler 1985; Kraichnan 1967).

in **Paper I** can be seen in figure 2.7. The density data is shown in the two top panels, while the corresponding PSD is presented in the two bottom panels. The purple area in (a) shows the integrated power in between 10-20 Hz, the hexagon in panel (b) shows the spectral break frequency. Both quantities have been used for extensive analysis in this thesis and will be explained in more detail in the next paragraphs.

It has been observed that these power spectra undergo spectral steepening, where two first-order fits describe the power spectral density when plotted on log-log axes, with a shallow fit at lower frequencies and a steeper fit at higher frequencies (Kintner and Seyler 1985). This spectral steepening can be seen in the bottom right panel of figure 2.7, where the PSD is best described by two fits. First observations of spectral steepening in the low-latitude ionosphere have been achieved by M. Kelley, Pfaff et al. 1982 with sounding rockets and satellites, and have since been observed on several occasions, (e.g. Hysell et al. 1994; Jahn and LaBelle 1998; LaBelle, M. C. Kelley and Seyler 1986). High-resolution in-situ measurements have provided means to observe similar steepening spectra in the high-latitude F-region, and it has been observed that the shallow, initial slope can often be described by $p_1 = -5/3$, while the high-frequency, steeper slope varies in between $-3 \geq p_2 \geq -5$ (S. Basu, S. Basu, MacKenzie et al. 1990; Di Mare et al. 2021; Ivarsen, Jin et al. 2019; Ivarsen, St-Maurice et al. 2021; Spicher, W. Miloch and J. Moen 2014; Villain, Hanuise and Beghin 1986).
Kintner and Seyler 1985 have further provided a summary for spectral slope

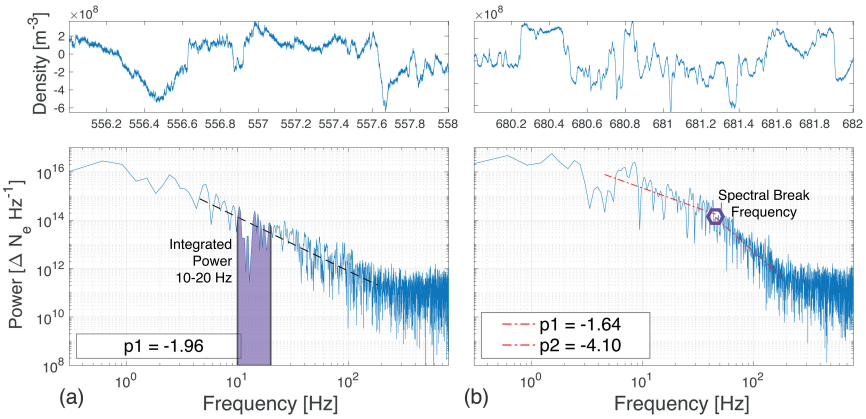

Figure 2.7: Top panels (a) and (b) show two seconds of detrended density from the TRICE-2 low flyer which was analyzed in the scope of **Paper I**. The bottom panels show the PSD for the corresponding density interval, where the PSD in panel (a) is best described by a single fit with $p_1 = -1.96$ and panel (b) is best described by two fits with $p_1 = -1.64$ and $p_2 = -4.10$ for the shallow and steep slope, respectively.
The purple area in (a) shows an example of one of the main analysis tools in **Paper I** and **Paper II**, the integrated power; here integrated between 10 and 20 Hz. The hexagon in (b) indicates the spectral break frequency, which has also been used for analysis in **Paper I** and **Paper II**, and denotes the frequency where the shallow slope changes to a steeper slope.

values of the ionospheric electron density and have linked it to a variety of instabilities. For example, the GDI is associated with $p_1 = -1$ and $p_2 = -5/3$ for the shallow and steep slope (inverse and direct cascade), respectively. The KHI on the other hand is associated with $p_1 = -5/3$ and $p_2 = -3$ for the shallow and steep slope (inverse and direct cascade), respectively.
The spectral break frequency has been observed with sounding rockets and satellites and found to occupy a vast variety of scales between roughly 1 and 100 Hz (Di Mare et al. 2021; Ivarsen, Jin et al. 2019; Ivarsen, St-Maurice et al. 2021; Spicher, W. Miloch and J. Moen 2014). The spectral break frequency has been allocated to a variety of different mechanisms, for example the ion inertial range or oxygen gyrofrequency at corresponding heights or a transition to a regime in which drift waves, diffusion or wave steepening occur (Di Mare et al. 2021; Hysell et al. 1994; Ivarsen, Jin et al. 2019; LaBelle, M. C. Kelley and Seyler 1986); other explanations include a transition between a collisional regime, where Pedersen drifts are dominating due to electron-ion and electron-neutral collisions, and an inertial regime in which the polarization current is mainly responsible for the plasma motion M. Keskinen and Huba 1990; Kintner and Seyler 1985, however, research is still ongoing.
While the analysis of the spectral slopes and break frequencies gives insights

about the redistribution of energy within the plasma and the processes involved, it does not provide the full picture. In order to obtain a measure of the energy contained in certain scales, or how prominent structures of certain scales are, we integrate the irregularity power in the PSD for several frequency intervals (thus measuring the area under the PSD in these frequency intervals). As the sounding rockets and satellites are moving through the ionosphere at (on average) velocities equal or larger than the ionospheric plasma velocities, the plasma is commonly assumed stationary, and we can thus convert the frequency intervals into spatial scales within the plasma. We thus gain a possibility to assess the spatial scales at which plasma structures are predominantly present in different regions within the ionosphere. This may help identifying how the plasma structures are formed, and locating differences in processes that aid plasma structuring in different regions.

Spectral analysis has been used within the scope of **Paper I** and **Paper II**. **Paper I** conducts spectral analysis on the electron density. While a quantification of the slopes is provided, the main focus lies on whether a spectrum steepens, at which frequency the spectral break occurs, and additionally, how much energy is found within a certain scale size by integrating the irregularity power in the PSD in a variety of frequency intervals. **Paper II** uses similar analysis on the electron density and magnetic field data. The main focus lies on whether spectra steepen and how much energy is deposited at frequencies associated with kilometer scales.

A steepening of the spectra has been allocated to different mechanisms in the scope of this thesis. One possible explanation for steepening is an injection of energy at large scales, corresponding to low frequencies. This injection lifts the low-frequency part of the PSD up to higher levels, which consecutively leads to a steepening of the graph as the high frequency PSD remains the same. On the contrary, the same scenario could be achieved by a diminishing of energy in the high frequencies, or small scale structures, which could be caused by a dissipation of energy of small scales. A steeper slope in the high frequency regime is then associated with processes leading to a faster decay of small scale structures, like enhanced turbulence. Another process that leads to the dissipation of small scale structures, and consecutively to a steepened spectrum is an enhanced E-region due to either solar EUV radiation or high-energetic particle precipitation. These processes enhance the Pedersen conductivity in the E-region, which consecutively leads to enhanced diffusion of structures in the F-region, as both regions are coupled.

In order to distinguish between an enhancement of large scales leading to a steepening and a diminishing of small scales, we analyze the integrated power of the PSD for a variety of scale sizes. This gives information on if the low frequency region is enhanced or the high frequency region is diminished if a double slope is observed.

Chapter 3

Instrumentation

The studies that comprise this thesis employ in-situ measurements as their main source of data. The measurements are mainly obtained from sounding rockets and the Swarm satellite constellation. While satellites are able to provide data over a long period of time, the flight time of sounding rockets is comparably short, however, they can obtain data at altitudes below the usual altitudes of satellite orbits, where the satellite would experience too much drag to keep a stable orbit. The primary instrument used is the multi-needle Langmuir probe (mNLP) (Bekkeng et al. 2010; Jacobsen et al. 2010), a system based on an array of cylindrical Langmuir probes which is able to sample the electron density at a high cadence. The following chapter aims to introduce the theory and use of the mNLP, as well as the different sounding rockets and satellites used for the studies.

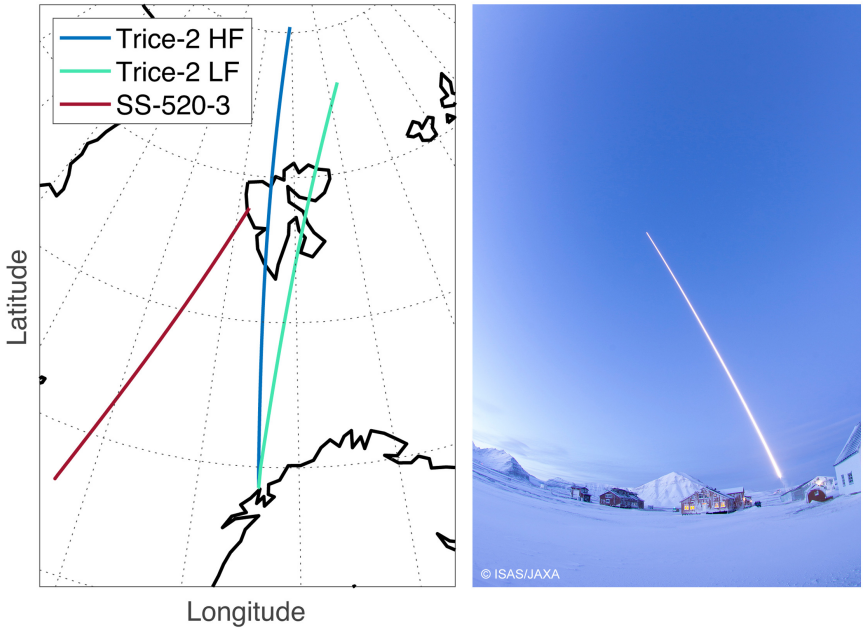

Figure 3.1: Left: Trajectories of the sounding rockets used in this thesis. HF and LF refer to the High and Low Flyer of the TRICE-2 sounding rockets, respectively. Right: Launch of the SS-520-3 sounding rocket from Ny-Ålesund, Svalbard, Norway. Courtesy of Prof. Nonaka at JAXA ISAS who took the picture and generously allowed its use in this thesis.

3.1 Langmuir Probes

A Langmuir probe is one of the simplest ways to obtain characteristics of a plasma. Langmuir probe theory has been discussed in detail in a vast variety of different works (Chen 2003; L. Conde 2011; Schott 1968), and this subsection aims to provide a brief overview.
The most basic implementation of a Langmuir probe is to insert a conducting wire into the plasma and measure the electric current to the wire. The current will then vary with the voltage applied to the probe.
Placing an object into a plasma will lead to charging of said object by the electrons and ions in the plasma. Due to the inequality in velocity between electrons and ions, the much faster electrons lead to a higher electron flux to the object and will thus bias it at a negative potential with respect to the plasma potential. One of the main principles of a plasma is quasi-neutrality, the equality of positive and negative charges when observing the plasma at large scales. As the placed object is biased negatively with respect to the plasma, the plasma aims to shield the negative charges by building up a region of (in this case) positive charge density, the sheath, in the vicinity of the object. The characteristic size of the sheath is related to the Debye length.[1]
If we assume a thin sheath, meaning the sheath building up in front of the probe is small in comparison to the collecting area of the probe, the sheath can be assumed planar. The collected current I to the surface is then determined by the current density j and the collection area A as

$$dI = Adj \tag{3.1}$$

Infinitesimal current densities for ions and electrons are given by

$$\begin{aligned} dj_i &= q_i n_i v_i f(v_i) dv_i \\ dj_e &= q_e n_e v_e f(v_e) dv_e \end{aligned} \tag{3.2}$$

with q, n, v and $f(v)$ being the charge, density, velocity and velocity distribution for ions (i) and electrons (e), respectively (Schott 1968). The current drawn to the probe for either electrons or ions then becomes

$$I = qnA \int_{v_c}^{\infty} v f(v) dv \tag{3.3}$$

where v_c corresponds to the velocity of the particles which have sufficient energy to overcome the sheath potential and are thus collected by the probe.
Another approach, besides the thin-sheath assumption, is considering a thick sheath forming in front of the probe. The sheath can then not be assumed small in comparison to the probe anymore, and the particle trajectories within the

[1] The Debye length λ_D is a characteristic length scale in a plasma. As the plasma is quasi-neutral, a test charge placed into the plasma would be shielded by species of opposite charge. The length at which the potential of the test charge is diminished to $1/e$ is called the Debye length.

Table 3.1: Parameters for planar, cylindrical and spherical probes. r and l are the radius and length of the probe, respectively.

	A	C	β
Planar	–	1	0
Cylindrical	$2\pi rl$	$2/\sqrt{\pi}$	1/2
Spherical	$4\pi r^2$	1	1

sheath have to be taken into account. The simplest approach to describe the current to such a probe is the Orbital Motion Limited (OML) theory (Mott-Smith and Langmuir 1926). When a particle reaches the vicinity of the probe, its trajectory will be altered. This alteration has to obey the laws of conservation of energy and momentum. The distance at which the particles trajectory will deviate is called the impact distance or impact parameter h (Lai 2012) and is given by

$$h = r\sqrt{1 - \frac{2q\Phi}{mv}} \tag{3.4}$$

where r is the probe radius, m, q and v are the particle mass, charge and velocity at the sheath, respectively, and Φ is the probe potential. Combining equations 3.3 and 3.4 under the assumptions of a Maxwellian distribution, and in the thick sheath limit ($r/h \to 0$), the electron current drawn towards the probe can be written as

$$I = \frac{1}{4} n_e q A \bar{v} C \left(1 + \frac{q\Phi}{kT_e}\right)^{\beta} \tag{3.5}$$

where A is the collecting area of the probe, n_e is the electron density, $\bar{v} = \sqrt{8kT_e/\pi m}$ is the average speed of the electrons, k is Boltzmann's constant, T_e is the electron temperature, and C and β are constants depending on the geometry of the probe. An overview of the constants for planar, cylindrical and spherical geometry can be taken from table 3.1.

One of the advantages of OML theory is that it provides generally a good compromise between accuracy and simplicity (Resendiz Lira and Marchand 2021).

A Langmuir probe is usually operated in a "sweep", meaning that the applied voltage is altered from negative to positive biases. The resulting current-voltage (I-V) characteristic will then comprise several regions from which plasma characteristics can be derived. A schematic of such a curve can be seen in figure 3.2 a. If the probe is biased at the **plasma potential** (number 3 in figure 3.2), the electrons and ions within the plasma can reach the probe at their thermal velocity, without the influence of a sheath.

If the probe is biased strongly negative with respect to the plasma potential, the probe only collects positively charged particles, as all negative charges will be repelled. This region is called the **ion saturation region** (region 1 in figure 3.2). When the probe bias becomes sufficiently positive, such that the electron velocity is high enough to overcome the potential that built up in front of the

probe, the **transition region** is reached (region 4 in figure 3.2). Within the transition region lies the **floating potential**, the potential where the currents of positive and negative charges are equal. For the simple case of a simply ionized plasma this equates to equal electron and ion flow, as $dj_e = dj_i$. Once the probe bias becomes sufficiently positive such that all positive charges are repelled from the probe, the **electron saturation region** of the I-V curve (region 5 in figure 3.2) is reached. The characteristics of the curve within this region depend on the effective collection area of the probe. For an infinitely large planar probe, where boundary effects can be neglected, the electron saturation region of the curve is represented by a horizontal line in the plot. With rising bias, the sheath building up in front of the probe grows linearly, however, in this case the collecting area of the probe will remain equal to the actual (planar) probe area. This results in the constant collected electron saturation current. For circular or cylindrical geometries, the developing sheath has a geometry similar to that of the probe. The collecting area will thus grow with the applied voltage corresponding to the surface area of either a sphere or a cylinder. The collecting surface of a cylinder is $2\pi la$; the collecting surface of a sphere is $4\pi a^2$, where a is the sheath thickness, and l is the length of the cylindrical sheath. Thus, the collective area grows $\propto a^2$ for a sphere or $\propto a$ for a cylinder. This leads to a rising I-V-curve, as seen exemplary for cylindrical probes in figure 3.2.
As illustrated above, Langmuir probes are usually operated in sweeps. Typical sweep times can last up to several seconds. With an average rocket velocity of a few $\mathrm{km\,s^{-1}}$, the lowest scale sizes that are resolvable during the sweep are of a few hundred meters. Additionally, the above mentioned I-V curve is heavily

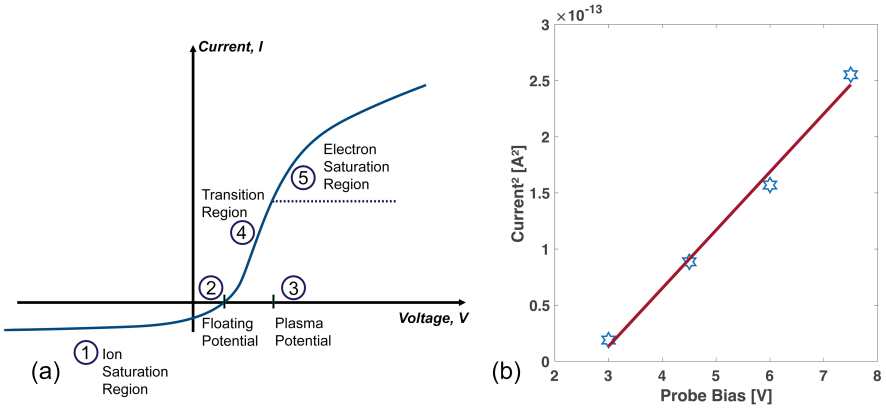

Figure 3.2: (a): Schematic of a typical current-voltage curve. The five regions are as follows: 1 - Ion Saturation Current; 2 - Floating Potential; 3 - Plasma Potential; 4 - Transition Region; 5 - Electron Saturation Current;
(b): Current^2-Voltage plot obtained from the multi-needle Langmuir probe on the SS-520-3 sounding rocket at 10:11:27 UT on November 4th, 2021. The slope of the fit can be used to determine the electron density n_e.

dependant on the reference potential, in this case the potential of the spacecraft.

3.1.1 The multi-needle Langmuir Probe

The multi-needle Langmuir probe makes use of OML theory. In addition to the conservation of energy and momentum, the derivation of the mNLP assumes a probe being much smaller than the Debye length. Furthermore the plasma must (a) follow a Maxwellian velocity distribution and must be (b) collisionless, (c) non-drifting and (d) unmagnetized (Jacobsen et al. 2010). In the F-region ionosphere, these criteria are usually fulfilled. As frequent collisions with neutrals cause electrons to follow a nearly Maxwellian velocity distribution criterion (a) is fulfilled. As the electron mean free path is sufficiently long, the thermal speed of electrons is much larger than the spacecraft speed and the Larmor radius is much larger than the probe radius, (b) – (d) are generally also fulfilled (Guthrie, Marchand and Marholm 2021; Hoang et al. 2018; Ivarsen, Hoang et al. 2019). With these assumptions, the current drawn by a cylindrical Langmuir probe can be obtained from equation 3.5 by

$$I_c = n_e q \sqrt{\frac{kT_e}{2\pi m_e}} 2\pi r l \frac{2}{\sqrt{\pi}} \left[1 + \frac{q(V_f + V_b)}{kT_e}\right]^{\beta} \tag{3.6}$$

where T_e, n_e, m_e and q are the electron temperature, density, mass and charge, respectively, k is Boltzmann's constant, r and l are the probe radius and length, respectively, and V_f and V_b are the floating or reference potential and the bias potential, respectively. β, as mentioned in the last section, is a factor that depends on the probe geometry. For an finite-length probe with $l \gg \lambda_D$, β equates $1/2$. Although finite-length effects often play a role in the implementation of probes on spacecrafts and thus leading to a variation of the factor, $\beta = 1/2$ has been found to be a good estimate (Guthrie, Marchand and Marholm 2021; Hoang et al. 2018; Jacobsen et al. 2010; Marholm and Marchand 2020). For $\beta = 1/2$, the electron density n_e can be rewritten from the above equation to

$$n_e = \left(\frac{m_e}{2q(2qrl)^2)} \frac{d(I_c^2)}{dV_b}\right)^{1/2} \tag{3.7}$$

The resulting equation is thus independent on T_e and V_f, and only depends on known variables, like the probe dimensions and bias (Bekkeng et al. 2010; Jacobsen et al. 2010). For $\beta = 1/2$, the electron density can then be inferred from a first-order fit in a plot of the squared current I_c^2 with respect to the bias V_b, if a minimum of two probes is utilized. An example of such a fit can be seen in figure 3.2 b.

It is important to note that in order to collect the electrons without the influence of collected ions the probe needs to be biased sufficiently positive with respect to the spacecraft potential. This may lead to discrepancies if, e.g., the probe with the lowest bias falls into a voltage regime too close to the spacecraft potential. For redundancy reasons, the mNLP systems used within this thesis all employ four identical, cylindrical Langmuir probes.

3.2 TRICE-2 Sounding Rockets

Paper I utilizes data obtained from the Twin Rockets to Investigate Cusp Electrodynamics (TRICE-2) sounding rockets. The rockets were launched on December 8th, 2018 from Andøya Space, Norway, located at 69°17' N, 16°01' E (geographic coordinates), as part of the Grand Challenge Initiative (GCI) – Cusp (J. Moen, Spicher et al. 2018). The rockets were launched two minutes apart at 08:26 UT and 08:28 UT. Due to the difference in altitudes they will be henceforth called the High Flyer (HF) and Low Flyer (LF), respectively. The HF reached its apogee of 1042.2 km at 08:37:16 UT, or 676 s after launch. The LF reached its apogee of 756.8 km at 08:37:46 UT or 586 s after launch. The rocket trajectories can be seen in figure 3.1. Further information about the launch conditions can be inferred from Moser et al. 2021, S. Fuselier et al. 2022 and Spicher, LaBelle et al. 2022.
Sounding rocket launches usually comprise a single sounding rocket. A unique feature of the TRICE-2 sounding rockets is the simultaneous measurements with two identical payloads at two different altitudes. This allows for a rare opportunity to measure the ionosphere at similar coordinates at the same time, but with a variation in altitude.
The main science goal for the TRICE-2 rockets was to assess whether changes seen in cusp-region ion energies are due to spatial or temporal modulation of magnetic reconnection (M. Conde et al. 2018). The science payload consisted of Electron Energy and Pitch Angle Analyzers (EEPAA), a high frequency electric field receiver, an ion electrostatic analyzer (ESA), a DC/ELF/VLF electric field instrument (DC **E**), a DC magnetometer, and Langmuir probes, of which four were part of the mNLP system (M. Conde et al. 2018).
Within the scope of **Paper I**, we focus on data obtained with the mNLP. The mNLP sampled the electron density at a cadence of 10 kHz. The four cylindrical probes had a length and diameter of 39 mm and 0.51 mm, respectively. The probes were mounted on two booms protruding equidistantly perpendicular from the rocket body with two probes per boom, leading to a distance of 1 m in between the probes on opposite booms when fully deployed. The biases of the probes were fixed to 3 V, 4.5 V, 6 V and 7.5 V.
In addition to the mNLP we also used the DC **E**-field data, which measures the electric field, and data from the on-board magnetometer with sampling frequencies of 2.5 kHz. We also used data from the EEPAA, which consisted of detectors placed in 10° steps around the spacecraft. The data employed in this study uses the 0° EEPAA data, which collects particles downwards along the magnetic field lines.

3.3 SS-520-3 Sounding Rocket

Paper III makes use of in-situ measurements from the SS-520-3 sounding rocket. Like the TRICE-2 sounding rockets, the SS-520-3 sounding rocket is part of the GCI – Cusp (J. Moen, Spicher et al. 2018). The rocket was launched from

SvalRak, Ny-Ålesund, Norway, located at 78°55' N, 11°51' E at 10:09:25 UT. The rocket reached its apogee of 742 km at 10:17:31 s, or 487 s after launch.
The main objective of the SS-520-3 rocket was to study the particle acceleration processes that cause ion outflow by investigating the wave-particle interaction over the cusp. The science payload consisted of a Digital Flux Gate Magnetometer (DFG), the Low Frequency Analyser System (LFAS), the Wave Particle Interaction Analyser (WPIA), the Thermal Ion Spectrum Analyser (TSA), two Low Energy Particle Analysers (LEP), an Ion Mass Spectrometer (IMS), the Sun Aspect Sensor (SAS), the Number density measurement of Electron by Impedance (NEI) probe, and five Langmuir probes, one spherical Fast Langmuir Probe (FLP), and four cylindrical Langmuir probes as part of the mNLP. In this study we make use of data from the mNLP, the NEI, and the two LEP detectors, one for measuring ions and one for measuring electrons.
The mNLP comprised four identical, cylindrical Langmuir probes with a radius of 0.51 mm, and a length of 25 mm each. The probes were mounted on four booms of 422 mm length. The probes, unlike the mNLP system on the TRICE-2 payloads, were not installed axisymmetric. For easier comprehension, a technical drawing of the booms on the rocket payload can be seen in figure 3.4. Two booms were installed on each side of the rocket at an angle of 9.94° from the rocket axis, protruding from the side of the rocket over the tip of the rocket. This lead to an angle in between both sets of booms of 19.88°. The two booms in each structure were angled at 27.54° away from each other. This construction had the advantage that the probes were located in front of the tip of the rocket, which mitigated wake effects.
The probes were biased at the same values as the mNLP system of the TRICE-2

Figure 3.3: Picture of the SS-520-3 sounding rocket. Courtesy of Ms. Ishizaki at JAXA ISAS who took the picture and generously allowed its use in this thesis.

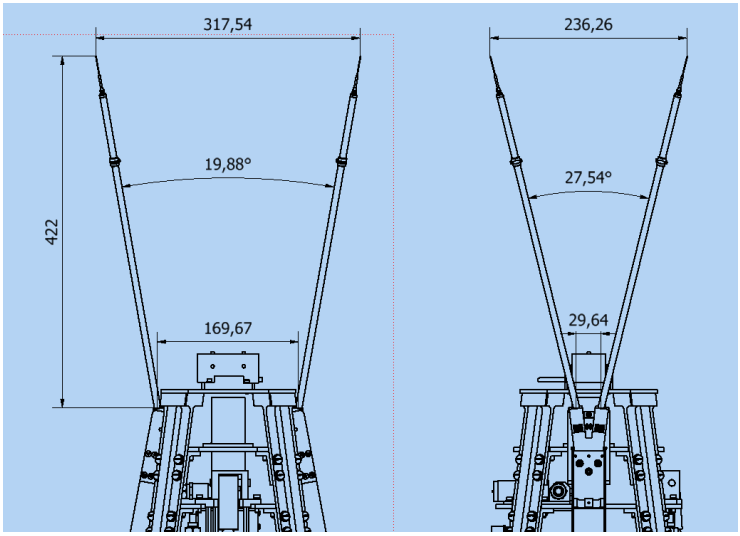

Figure 3.4: Technical drawing of the mNLP and booms installed on the SS-520-3 rocket. Courtesy of the I-Lab, University of Oslo.

rockets, at 3 V, 4.5 V, 6 V and 7.5 V, respectively, and were able to sample the electron density at a cadence of 3.2 kHz.
The NEI consisted of a spherical probe with a length of 1.2 m and a radius of 6 mm that was installed on one side of the rocket towards the tip of the payload. A similar front end of the NEI has been used before and is further described in Suzuki et al. 2010. The NEI measured the minimum of the probe capacitance by a frequency sweep of the AC signal applied to the capacitance bridge located within the NEI. From that, the upper hybrid resonance (UHR) frequency, and thus the electron density, could be determined. The general equation for obtaining the electron density from the UHR is

$$N_e = 1.24 \cdot 10^4 (f_{\mathrm{UHR}}^2 - f_c^2) \tag{3.8}$$

where N_e is the electron density, and f_{UHR} and f_c are the UHR frequency and electron cyclotron frequency, respectively (Wakabayashi, Ono et al. 2005). A more thorough approach of this calculation can be obtained from Oya and Aso 1969 and Wakabayashi, Suzuki et al. 2013. The frequency range of the probe was 0.1–20.4 MHz, and with a sweep time of 125 ms, the probe was able to sample the electron density with values up to $5 \cdot 10^{12}\,\mathrm{m}^{-3}$ at a cadence of 8 Hz.
The LEP instruments comprised two identical top-hat electrostatic analysers along two micro channel plate (MCP) detectors. Two instruments were used in order to sample both electrons and ions, simultaneously. Instead of measuring ions and electrons directly, an ultra-thin carbon foil was added in between the ESA and MCP, in order to measure the current from secondary electrons emitted from the foil. The ultra-thin carbon foil is also used in order to develop a system where

one single instrument is able to quantify both ions and electrons concurrently, as described in Yokota, Saito and Asamura 2023. 16 analyzers were installed around the rocket body to measure particles from different angles. In this study we use data of particles flowing downwards along the magnetic field in a 30° angle.

3.4 The Swarm Satellites

The ESA Swarm satellite constellation was launched on November 22nd, 2013 from Plesetsk Cosmodrome, Russia, located at 62°92' N, 40°57' E into nearly polar circular orbits at an altitude of approximately 490 km (D. Knudsen, Burchill et al. 2017). The constellation consists of three identical satellites, Swarm Alpha (A), Bravo (B), and Charlie (C)[2]. The main scientific objective is the investigation of the Earth's magnetic field and analysing the magnetosphere-ionosphere interactions (Friis-Christensen, Lühr and Hulot 2006; Friis-Christensen, Lühr, D. Knudsen et al. 2008). In April 2014, the constellation was rearranged so that Swarm A and C are now on average flying side-by-side with 1.4° degrees longitudinal separation at the equator in a nearly circular orbit with an inclination of 87.35°, and at an altitude of about 460 km; Swarm B is in an orbit with an inclination of 87.75° at an altitude of roughly 510 km.
In this thesis data from both Swarm A and C from the time intervals 2014-10-01 to 2016-12-31 and 2020-01-01 to 2022-12-31 are analysed. These intervals were chosen to compare conditions close to solar maximum and solar minimum. The main instrument used was the the Electric Field Instrument (EFI) which obtained the 16 Hz plasma density. A detailed description of the EFI is provided in D. Knudsen, Burchill et al. 2017. The density can be obtained from the current carried to the face plate of the EFI. The electron density measurements are only provided for times when the faceplate is biased to values below -2.5 V, which is usually at times when the Thermal Ion Imager (TII), a part of the EFI, is inactive. This leads to data gaps throughout the time intervals.
In addition to the 16 Hz electron density, we used the 50 Hz magnetic field data, the 1 Hz field-aligned current data set, the 1 Hz Rate of Change of TEC (ROTI) data, geographic coordinates and the region flag from the the Ionospheric Plasma Irregularities (IPIR) product (Jin, Kotova et al. 2022).
The IPIR dataset uses the 2 Hz electron density data, magnetic field data from the on-board magnetometer and the on-board GPS receiver to file newly calculated quantities and existing data into one large file. The main quantity used is the ROTI data, obtained from the following equation:

[2]The CAScade Smallsat and Ionospheric Polar Explorer (CASSIOPE) satellite was introduced into the Swarm constellation in 2018 as Swarm Echo (E). The Swarm constellation thus contains four satellites, though Swarm E is not on a circular orbit but rather a highly elliptical orbit.

$$\mathrm{ROTI}(t) = \sqrt{\frac{1}{N-1} \sum_{t_i=t-\Delta t/2}^{t_i=t+\Delta t/2} \left|\mathrm{ROT}(t_i) - \overline{\mathrm{ROT}}\right|^2} \tag{3.9}$$

where t is the time for which the quantity is calculated, Δt is the time interval used for calculation, for the case of this work $\Delta t = 20\,s$, N is the number of steps used for calculation, and ROT and $\overline{\mathrm{ROT}}$ and the rate of change of TEC and the mean, given by the following expressions, respectively (Jin, Spicher et al. 2019):

$$\mathrm{ROT}(t) = \frac{\mathrm{VTEC}(t+\Delta t) - \mathrm{VTEC}(t)}{\Delta t} \tag{3.10}$$

$$\overline{\mathrm{ROT}} = \frac{1}{N} \sqrt{\sum_{t_i=t-\Delta t/2}^{t_i=t+\Delta t/2} \mathrm{ROT}(t_i)} \tag{3.11}$$

with the VTEC being Vertical TEC.
The electron density dataset is calculated from an instrument that directly measures the density in the vicinity of the spacecraft, and thus gives information about the localized plasma density within a close region around the instrument. The ROTI dataset, on the other side, is calculated from the on-board GPS receiver and gains information about the electrons located between the receiver and GPS satellites, and thus covers a larger ionospheric area. It is thus of advantage to use ROTI data as an additional dataset complimenting the in-situ electron density measurements.

3.5 Information about Typical Scale Sizes

Table 3.2 shows the typical scale sizes that can be resolved from the main instruments used in this thesis. The table gives information about the cadence of the instrument, the average velocity of the spacecraft and based on that the smallest scale size that can be resolved. Additionally, it provides the time frame used for PSD calculation and the distance the spacecraft has travelled in that time frame.

There are a few pitfalls that one needs to be cautious about when using a direct conversion between the spacecraft velocity and structures in the plasma. First of all, the plasma needs to be sufficiently time-invariant, especially for the PSD intervals, where a larger ionospheric area is covered within one dataset. Additionally, the lowest resolution possible for the TRICE-2 mNLP would be of sub-meter scales if taken from the direct conversion between rocket speed and sampling frequency alone. However, the distance between the probes is 1 m, and no resolution below this scale is possible, as it is assumed that the probes observe the same plasma.

Table 3.2: Typical scale sizes and resolutions for the main instrumentation. The first column shows the main instruments used. The top row displays the following information: The first column shows the cadence of the instrument; the second column shows the spacecrafts average velocity; the third column shows the smallest scale sizes that are resolvable based on the Nyquist frequency. The second row displays the following: The first column after the instruments displays the time interval that is used to calculate a single PSD; the second column shows the distance that each spacecraft has travelled in that given time frame.

Instrument	Cadence	Velocity	Smallest Scale Size
mNLP (TRICE-2)	10 kHz	$\approx 2 - 3\,\mathrm{km\,s^{-1}}$	$\approx 1\,\mathrm{m}$
mNLP (SS-520-3)	3.2 kHz	$\approx 2 - 3\,\mathrm{km\,s^{-1}}$	$\approx 10\,\mathrm{m}$
N_e (Swarm)	16 Hz	$\approx 8\,\mathrm{km\,s^{-1}}$	$\approx 1\,\mathrm{km}$
B_y (Swarm)	50 Hz	$\approx 8\,\mathrm{km\,s^{-1}}$	$\approx 300\,\mathrm{m}$

Instrument	Interval (PSD)	Distance (PSD)
mNLP (TRICE-2)	2 s	6 km
mNLP (SS-520-3)	2 s	6 km
N_e (Swarm)	1 min	$\approx 480\,\mathrm{km}$
B_y (Swarm)	1 min	$\approx 480\,\mathrm{km}$

3.6 Supporting Instrumentation

Additional instrumentation utilized within the scope of this study comprises a set of ground-based instruments and electron precipitation data from satellites. We employed data from the All-Sky Imager (ASI) from the University of Oslo, located in Longyearbyen, Svalbard, Norway, in **Paper I**. All-Sky Imagers usually consist of a fish-eyed lens directed upwards, and are used to take pictures of the night-sky. The imagers employed were equipped with monochromatic filters, so that the cameras were capturing the aurora at their green (557.7 nm) and red (630.0 nm) emission lines. The green and red aurora were then projected to 150 km and 250 km, respectively.

We further used data from the European Incoherent Scatter (EISCAT) Svalbard radar located in Longyearbyen, Svalbard, Norway, consisting of two antennas. The larger, 42 m antenna is positioned to measure along the magnetic field lines. Within the scope of **Paper III**, we only utilized the smaller, 32 m steerable antenna, to obtain ionospheric conditions close to the trajectory of the SS-520-3 sounding rocket.

Paper III further comprised data from scintillation receivers from the University of Bergen (Oksavik 2020a; Oksavik 2020b), stationed around Svalbard, Norway. These receivers are able to sample disturbances in the phase and amplitude of electromagnetic waves, also known as scintillations (Kintner, Ledvina and De Paula 2007; Yeh and C.-H. Liu 1982). These waves are sent out from

Global Navigation Satellite Services (GNSS) satellites, like GPS, GLONASS and GALILEO satellites for positioning services. In addition to scintillation data, some receivers are also able to provide a measure of the Total Electron Content (TEC). We furthermore employed an additional TEC data set from the Madrigal database, which collects scintillation indices and TEC data from a large collection of receivers around the world.
In addition to supporting ground based instruments we also used precipitating electron data from the Total Electron Detector (TED) and the Medium Energy Proton and Electron Detector (MEPED) on board the NOAA-18 (National Oceanic and Atmospheric Administration) and MetOp-03 (Meteorological Operational) satellites (CEOS EO Handbook and ESA Meteorological Mission 2012; D. S. Evans 2000; Goodrum, Kidwell and Winston 2009). The NOAA-18 satellite is in a sun-synchronous orbit at roughly 850 km orbiting the Earth approximately every 102 minutes. The MetOp-03 satellite is in a sun-synchronous orbits at an altitude of about 825 km. The satellite orbits the Earth roughly every 101 minutes. The TED and MEPED are able to measure electrons and ions at different angles and energies. In **Paper III** we use field-aligned precipitation (0° data) and 30°/90° data for the TED/MEPED, respectively.

Chapter 4

Commentary on the Papers

In this chapter, the three papers that comprise this thesis are presented. Summaries of the main data sets and analysis methods are given, as well as information about the rocket launch conditions, if applicable. Additionally, the main findings of each paper are stated and briefly discussed. As **Paper I** and **Paper III** are easier discussed together as both present data from sounding rockets launched into an active cusp, the discussion of **Paper III** will be moved in front of that of **Paper II**.
After the summary of the three papers has been provided, a brief summary of the novelties this thesis provides is given, followed by an outlook for future work based on the presented studies.

4.1 Summary of the Papers

Paper I aimed to investigate the impact of electron precipitation into the cusp ionosphere on plasma structuring. The study used data from the TRICE-2 sounding rockets, which were launched into the winter cusp ionosphere.
The mNLP data used was processed further and Power Spectral Density plots were made for each two seconds of data. After plotting the PSD with log-log axes we determined if it was best described by one or two fits. The condition for two fits to steepen sufficiently was $p_2 - p_1 \geq 0.8$, where p_2 and p_1 are the slope of the steep and shallow fit, respectively. If the PSD was best described by two fits it was further determined at which frequency the spectral break point occurred. We additionally calculated the integrated power within several frequency intervals in order to obtain a measure of the energy contained in different scales. We further calculated the $\boldsymbol{E} \times \boldsymbol{B}$ drift from the electric and magnetic field instruments.
One of the main findings of the paper was linking an increase in the integrated power from the density PSD within hundred-meter scales to an energy input on these scale sizes by means of particle precipitation. We found that frequencies in the range mentioned above, but especially between 10–30 Hz were elevated when the rockets flew through the cusp and encountered precipitating electrons. Once the rockets exited the poleward side of the cusp, integrated power in frequencies between 100–1000 Hz were enhanced, suggesting that the energy that was injected into the large scale structures was broken down into smaller structures, visible in the higher frequency intervals. Both rockets encountered flow shears just poleward of the cusp, where instabilities can act on the plasma structures to further redistribute the energy.
Furthermore, we analyzed the occurrence of spectral steepening and the

corresponding break frequencies. While the first parts of both flights showed little steepening, we saw a sudden increase in steepening when the rockets entered the cusp and encountered particle precipitation. As explained above, an increase in lower frequencies within the precipitation region was observed. This increase elevated the low frequency part of the PSD, which could lead to a higher probability of steepening within a PSD. We additionally found that the average break frequency was close to the oxygen gyrofrequency at corresponding altitudes, however, the spectral break frequency was rising with an increase in $\boldsymbol{E} \times \boldsymbol{B}$-drift velocity, which could possibly be explained with a phenomenon similar to a Doppler shift, shifting the break points to higher frequencies.
Moreover, comparison of the electron precipitation data from the EEPAA and the electron density fluctuations showed that enhancements within the electron density fall within gaps in the particle precipitation, and vice versa. Particles entering the ionosphere into the lower F or E-region enhanced the conductivity in these regions. As both regions were coupled, the enhanced conductivity in a region below the rocket lead to faster dissipation of irregularities at the rocket location. As mentioned earlier, we observed an overall increase in density fluctuations on large scales within the cusp in comparison to the region equatorward of the cusp. However, when comparing regions within the cusp, stronger electron density fluctuations appeared in gaps of precipitation.
As mentioned in the first introduction of the TRICE-2 campaign, the simultaneous launch of two rockets gives a rare opportunity to investigate the ionosphere simultaneously in similar locations at different altitudes. While the above mentioned results were obtained for both altitudes, differences were identified as well. The integrated power calculated from the HF showed very little fluctuations throughout the majority of the flight, a strong rise in all frequencies was observed coinciding with the enhanced drift velocity poleward of the cusp. The LF, on the other hand, showed enhancements throughout a larger flight interval. Though this enhancement was also co-located with the rise in drift velocity, the magnitude of enhancement between the drift velocity and rise in integrated power does not match. Additionally, while the HF integrated power was enhanced throughout all frequencies, the LF integrated power mainly rose in frequencies below 200 Hz, and could partially depend on the impact of particle precipitation. It is thus possible that plasma structuring in the ionosphere is influenced by different drivers at different altitudes.

Paper III aimed to analyze the flight conditions for the JAXA SS-520-3 sounding rocket launch, and investigate the variations of electron density within different structures: polar cap patches, a cusp patch and a tongue-of-ionization partially located within the cusp. It was identified that the rocket was launched into the main phase of a geomagnetic storm and entered the poleward region of the cusp at 74° of northern geographic latitude. The rocket stayed within the cusp for nearly the remaining time

of the flight, until it crossed the equatorward boundary at 68° of northern geographic latitude. This corresponded to a more equatorward cusp than usually seen during more quiet conditions.
OMNI data showed a shift in magnetic field configurations approximately at 09:00 UT, where the IMF B_y changed from negative values to strongly positive values (up to 20 nT), which stayed at similar values until after the end of the rocket flight. Additionally, the B_x and B_z indices changed polarity several times during the interval, with B_z dropping to negative values just before launch, indicating a southward IMF. The changes in IMF caused a change in the ionospheric convection cell pattern. Thus two TOI were observed, one moving from the dayside over the dusk-sector into the nightside, detaching from the dayside region of enhanced TEC at approximately 09:40 UT. A second, dawnwards convecting TOI formed around magnetic noon at approximately the same time. The newly formed TOI was crossed by the rocket towards the end of the flight, at approximately 10:23 UT.
The convection of the first TOI was likely also observed with the EISCAT radar as two regions of convecting plasma with north-east components were identified. It is important to mention here that a flow registered towards the radar, thus in north-east direction, could not only indicate a flow in this direction. As the radar is tilted, and thus pointing upwards at an angle, a downwards flowing structure would result in similar findings. Additionally, in the submitted version of the manuscript that is implemented in this thesis, it was concluded that the region convecting towards the south-west was linked to the newly formed TOI. Further investigations have shown that the radar beam does not reach the poleward edge of the TOI. However, as previously discussed, the change of the IMF leads to a change in the convection cell pattern. The resulting variation in flow will not only affect the TOI but also the background plasma, which will consecutively be observed with the radar. The points discussed in this paragraph will be amended in a future version of the manuscript, however, the EISCAT data set still provides invaluable information on the ionospheric plasma flow and shall remain in the paper.
Analysis of the electron density showed that the rocket encountered five density enhancements, which were categorized into three regions: polar cap patches, a cusp patch, and the newly formed tongue-of-ionization, which was described above. We further processed data from the mNLP by determining the variations of the electron density fluctuations on 10 m, 100 m and 1000 m scales. The analysis of these electron density variations showed that the strongest enhancements on all scales were observed on the poleward edge of the TOI. Differential convection of the TOI and background plasma can lead to flow shears that can trigger instabilities like the KHI, leading to an increase of plasma structures along the edge of the TOI. While the PCP was encountered at similar altitudes as the CP and TOI, overall structures within the cusp (the CP and part of the TOI located within the cusp) showed more enhanced variations when compared

to the PCP density variations, especially on kilometer scales. The kilometer and hundred meter scales were additionally more enhanced within the cusp-part of the TOI in comparison to the equatorward part of the TOI. This suggests stronger fluctuations within the cusp structures, especially on kilometer and hundred meter scales, which is concurring to results of **Paper I**.

Additionally, enhanced phase scintillation indices and TEC values were observed when the rocket entered the cusp, however, the electron density showed little fluctuations. The scintillation indices were mapped onto 250 km altitude, while the rocket flew above 500 km in this region. Scintillations are connected to structures in the plasma density of hundreds of meters and should thus show up in the electron density variations of the corresponding scale sizes. It was thus concluded that the structures were localized several hundred kilometers below the rocket and were thus not measured.

It is interesting to note, that while both the sounding rockets described in **Paper I** and **Paper III** were launched into active cusp aurora, the SS-520-3 rocket encountered little fluctuations above 500 km, even if located within an active cusp, while the TRICE-2 rockets measured strong fluctuations in the electron density at higher altitudes. Both rocket launches were naturally not occurring on the same date and were separated by several years and operated under different conditions, all of which could have an influence on the altitude of observed structures. The TRICE-2 rockets were launched on December 8th, 2018 at roughly 08:30 UT, while the SS-520-3 rocket was launched on November 4th, 2021 at roughly 10:10 UT. This could for example indicate different influences of solar EUV on the regions the rockets flew through. Generally, the ionosphere is a highly dynamic region as outlined on several occasions throughout this introduction, and thus it may not be unlikely that differences in observations occur. It does, however, leave open questions. The outlook in the next section will elaborate on some of those unanswered questions.

Paper II aimed to provide long-term statistics of the results obtained in **Paper I**. Similar to **Paper I**, we used PSD plots to obtain information about the fluctuations and energy distribution on kilometer scales in the electron density and magnetic field data. From the magnetic field data set, we only employed the B_y component, which gave a measure of the magnetic field perpendicular to the FAC, and thus was used as a proxy for FAC filamentation (Fæhn Follestad et al. 2020). We chose to use the 50 Hz data instead of the FAC data, as the 1 Hz cadence of the FAC data was not sufficient for the analysis employed in this study. For each one-minute interval for both quantities we calculated the PSD with the Logarithmic frequency axis Power Spectral Density (LPSD) method, a modified method based on the original Welch's method (Tröbs and Heinzel 2006; Welch 1967). Just as in **Paper I**, we calculated if the PSD plot was best described with a single fit or two fits. In order to achieve that, we used an automated

slope detection method, which had been previously developed by Ivarsen, Jin et al. 2019 for use on the 16 Hz faceplate density. The method is in further detail described in Ivarsen, Jin et al. 2019 and Ivarsen, St-Maurice et al. 2021. In addition to the slope analysis, we calculated the integrated power between 1–2 Hz from both the density and magnetic field PSD, which corresponded to spatial scales of 3.6–7.2 km.
In order to display the data in an easily accessible way, it was divided into the northern and southern hemisphere, and further into the four seasons. The data was then binned into regions corresponding to 2° magnetic latitude (MLat), and 1 hour of magnetic local time (MLT). For the conversion between geographic to magnetic coordinates magnetic apex coordinates were used (Emmert, Richmond and Drob 2010). In order to display the data, we chose two different analysis methods. The slope probability showed how likely it was in each given bin to obtain a double slope or a single slope. The values thus varied between 100 % single slope probability and 100 % double slope probability. For all other values (integrated power, ROTI, and FAC data) we calculated the median in each given bin. The quantities displayed in the main part of the paper were thus the following: the double slope probability from the electron density and B_y PSD, the corresponding integrated power in the frequency regions 1–2 Hz, and the ROTI data, for the interval 2014–2016. Due to data gaps stemming from the usage limitations of the faceplate for obtaining the density (see section 3), the data for the timeframe 2020–2022 was not deemed sufficient and was thus placed within the appendix. We additionally analyzed the integrated power from the density PSD for the intervals 0.1–0.6 Hz and 6–7 Hz, and from the B_y PSD for 21–22 Hz. Due to the large similarity within the data sets, the plots were not displayed within the paper but rather used for discussion. The overall number of passes we used for the data corresponded to roughly 12500, which provided over 400 000 PSDs for analysis.
One of the inspirations for the work of **Paper II** was to provide long-term statistics of the results obtained in **Paper I**, especially the enhancements in electron density fluctuations on the poleward edge of the cusp. It became clear after the analysis of the data that due to the dynamic nature of the ionosphere, this was not possible, as the results from **Paper I** depended largely on the position of the poleward boundary of the cusp. As the location of the cusp varies, a long-term statistical approach for evaluating fluctuations on the edge of the cusp was not suited for this kind of work. The results from the data were, however, interesting and novel in themselves and further analysis was thus pursued.
The results showed that the integrated power from the density PSD exhibited seasonal dependencies, as the integrated power around the equinoxes, especially for the northern hemisphere, was enhanced. Moreover, a strong interhemispheric variation was seen. The higher power around the equinoxes may be explained by the tilt of the Earth's magnetic field, leading to a better alignment with the IMF.

Comparison between the integrated power of the density PSD and the ROTI data showed similar features in both data sets, however ROTI data showed larger enhancements within the cusp and the nightside auroral oval. This may indicate different drivers for the formation of instabilities within these regions.
Moreover, the electron density slope probability within the polar cap exhibited a seasonal dependency on solar EUV radiation. The highest probability for a double slope in the polar cap was thus found in local summer, for both hemispheres. A higher solar EUV influence can lead to enhanced conductivity in the E-region, and, similar to the results in **Paper I**, the higher conductance leads faster diffusion of plasma within the F-region, as both regions were intimately coupled. The dissipation of energy at small scales lead to a region with less irregularity power within the higher frequencies of the PSD. The occurrence of a steepening of slopes became thus more likely. These results corroborated previous results from Ivarsen, St-Maurice et al. 2021.
The analysis of the B_y data showed that the residual magnetic field data had the largest fluctuations within the cusp for both hemispheres and all seasons. The data analyzed generally represented scales below 10 km. An enhancement at these scales indicates an increase in Poynting flux connected to the input of Alfvénic energy. These Alfvén waves can contribute directly to an energy input into the auroral acceleration region, which can consequently trigger an onset of particle precipitation into the ionosphere and thus the formation of aurora.

To sum up the research and results of these studies, this thesis presents the following findings and novelties on high-latitude F-region plasma structuring in arbitrary order

- Cusp particle precipitation functions as a source of free energy, mainly depositing this energy in scales of hectometers to kilometers, which consecutively lifts the low frequency region of the electron density PSD. This subsequently leads to slope steepening in the region.

- Strong flow shears on the poleward boundary of the cusp structure the plasma due to flow shear instabilities, prompting strong enhancements in electron density fluctuations. The structured plasma then enters the PC pre-structured, where it is susceptible to a variety of other instabilities, e.g., the GDI. This suggests further evidence of the two-step process suggested by H. C. Carlson et al. 2007, Hosokawa, Shiokawa et al. 2009 and J. Moen, Oksavik, Alfonsi et al. 2013, where the KHI pre-structures the plasma when first entering the PC, on which the GDI can then effectively act to further structure the plasma.

- Large flow shears in the plasma lead to a rise in spectral break frequency in the electron density PSD. The rise in spectral break frequency aligns with

the rise in $\mathbf{E} \times \mathbf{B}$-drift velocity, and could be allocated to a phenomenon similar to a Doppler shift making the break frequency effectively appear higher to the observer.

- Seasonal climatologies of ROTI, the electron density and small-scale fluctuations of the FAC make it possible to compare these quantities over the span of several years. We showed that enhancements in ROTI and plasma structures with scales of several hundred meters are co-located, but that ROTI is more enhanced in the cusp and midnight auroral oval, indicating further structuring in these regions.

- The same climatologies show enhancements in Poynting flux through the investigation of fluctuations on hectometer to kilometer scales in the FAC. These enhancements are co-located with enhanced ROTI values, further supporting earlier studies who have found enhancements in scintillation indices in the cusp co-located with filamentary FAC.

- First results of the SS-520-3 sounding rocket provide in-situ measurements within an expanded PC and cusp during a geomagnetic storm. In-situ measurements of polar cap patches, a cusp patch and a newly formed TOI show that fluctuations of cusp structures are larger than that of structures in the polar cap.

- Comparison between the mNLP and an impedance probe show a good agreement between the densities obtained from both probes. Several regions show larger deviations between the mNLP and the impedance probe, though never more than a factor of 1.5. Though the β-factor used in the calculation of the mNLP density has been shown to vary from $\beta = 1/2$ used in this thesis, the strong agreement between the densities further strengthens the use and accuracy of the mNLP system.

4.2 Future Work and Issues yet to be Resolved

Two of the studies in this thesis were based on sounding rocket experiments, which usually comprise data sets taken over a limited amount of time, e.g. 15-20 minutes. Thus, the phenomena observed with sounding rockets are usually of local nature and it is of interest to figure out whether they are of reoccurring nature as well. For example, the findings of **Paper I** showed that the strongest density fluctuations where observed just on the poleward edge of the cusp, which left the question if this was due to the high flow shear observed within this region, or was occurring regularly. Additionally, we observed an onset of slope steepening when the TRICE-2 rockets entered the cusp. The second paper aimed to statistically analyze the results obtained in **Paper I**, however, as mentioned in the summary of **Paper II**, due to the dynamic nature of the ionosphere the location of the cusp shifts, which makes a statistical approach difficult. While **Paper II** achieved novel results based on climatology of the high-latitude ionosphere, the results did not quantify phenomena occurring at

the borders of the cusp. In a future study, knowing the location of the cusp would be beneficial, though not easily achieved. Generally, the IPIR product gives the possibility to distinguish between the auroral oval and the polar cap, which would enable studies on the edges of the nightside auroral oval. Further studies on the statistical approach done with the Swarm satellite could also distinguish between active and inactive days, e.g. based on the KP index, or utilize the IPIR index, giving information about the fluctuations within the ionospheric plasma density. The data could then be further divided into regions of high and low activity.

The electron density data used from the Swarm satellites in **Paper II** has a cadence of 16 Hz. The maximum resolution in a spectral analysis that could be obtained is then 8 Hz, which corresponds to the Nyquist frequency. The Swarm satellite speed is close to the first cosmic speed, just below $8\,\mathrm{km\,s^{-1}}$. The smallest scale sizes we can thus obtain information on is of kilometer scales. It would be of interest to do similar statistical analyses of fluctuations within the electron density and small scale variations in the field-aligned currents at a higher cadence, allowing access to information concerning smaller scale structures. This may provide valuable information on the forecasting of e.g., the S4 amplitude scintillation indices, which are affected by structures in the electron density of a few hundreds of meters. One of the possible missions for a higher cadence in electron density measurements could be the NorSat-1 mission, allowing a measure of the density with the mNLP at 1 kHz. A higher cadence could also shed light onto the nature of the spectral break point frequency in the plasma density PSD. Observations with sounding rockets (e.g., **Paper I** and prior non-published analysis done within the scope of **Paper III**) observe a break frequency between 15-100 Hz, with a median value close to the oxygen gyrofrequency at corresponding altitudes. The data from the Swarm satellites has too low sampling frequencies to analyze these breakpoints, and the break point is rather seen at frequencies around 1 Hz. The energy cascade described in Kolmogorov 1941 predicts three regions within the PSD, a shallow region where energy is injected, the inertial subrange, in which nonlinear processes transfer energy from larger to smaller scales, and the dissipation region, in which the energy is dissipated. The break points observed with the sounding rockets are mostly allocated to the break between the second and third region. It would thus be interesting to see if the break point observed with Swarm at lower frequencies could be connected to the transition between the energy injection region and the inertial subrange.

Paper III laid the ground work for future studies, by giving an in-depth description of the SS-520-3 sounding rocket launch. Additionally, the variations in the electron density on several scales were analyzed and quantified. Overall, the quantification of the variations was done for larger regions (PCP, CP and TOI), while it was clear that the largest fluctuations were found on the poleward edge of the TOI. It would be of interest to look at the different density enhancements in-depth and distinguish between the poleward and equatorward edges, and quantify the density fluctuations within the structures in more depth. Once the electric field data becomes available, detailed studies of the KHI and

GDI and calculation of growth rates could be undertaken, further investigating the onset of how these instabilities structure the plasma in the PC and cusp. Furthermore, within the scope of **Paper III**, we utilized the electron density from the NEI probe. The probe data was mainly used as a comparison for the mNLP. As outlined in section 3, the calculation of the electron density from the mNLP depends on a variety of factors, however, a good fit between the densities obtained with both probes was found. The equivalence between both densities was identified to vary in regions with enhancements in electron density fluctuations, with differences of up to a factor of 1.5. Another interesting study would be quantifying the difference in density on certain phenomena with the use of additional sets of instruments, like the electric field data from the rocket payload. This could function as the further development of Langmuir probe systems for ionospheric research.

Bibliography

Basu, B. and Coppi, B. (1988). 'Fluctuations associated with sheared velocity regions near auroral arcs'. In: *Geophysical research letters* vol. 15, no. 5, pp. 417–420.

Basu, S., Basu, S., Chaturvedi, P. et al. (1994). 'Irregularity structures in the cusp/cleft and polar cap regions'. In: *Radio science* vol. 29, no. 1, pp. 195–207.

Basu, S., Basu, S., MacKenzie, E. et al. (1990). 'Plasma structuring by the gradient drift instability at high latitudes and comparison with velocity shear driven processes'. In: *Journal of Geophysical Research: Space Physics* vol. 95, no. A6, pp. 7799–7818.

Bekkeng, T. et al. (2010). 'Design of a multi-needle Langmuir probe system'. In: *Measurement science and technology* vol. 21, no. 8, p. 085903.

Berger, T. et al. (2023). 'The thermosphere is a drag: The 2022 Starlink incident and the threat of geomagnetic storms to low earth orbit space operations'. In: *Space Weather* vol. 21, no. 3, e2022SW003330.

Brekke, A. (2012). *Physics of the upper polar atmosphere*. Springer Science & Business Media.

Carlson, H. C. (2012). 'Sharpening our thinking about polar cap ionospheric patch morphology, research, and mitigation techniques'. In: *Radio Science* vol. 47, no. 4.

Carlson, H. C. et al. (2007). 'Case for a new process, not mechanism, for cusp irregularity production'. In: *Journal of Geophysical Research: Space Physics* vol. 112, no. A11.

CEOS EO Handbook and ESA Meteorological Mission (2012). 'MetOp (Meteorological Operational Satellite Program of Europe)'. In: *Sea*.

Chaston, C., Bonnell, J. et al. (2003). 'Properties of small-scale Alfvén waves and accelerated electrons from FAST'. In: *Journal of Geophysical Research: Space Physics* vol. 108, no. A4.

Chaston, C., Carlson, C. et al. (2007). 'How important are dispersive Alfvén waves for auroral particle acceleration?' In: *Geophysical Research Letters* vol. 34, no. 7.

Chen, F. F. (2012). *Introduction to plasma physics*. Springer Science & Business Media.

— (2003). 'Langmuir probe diagnostics'. In: *IEEE-ICOPS Meeting, Jeju, Korea*. Vol. 2. 6. Citeseer.

Clausen, L. B. N. and Moen, J. (2015). 'Electron density enhancements in the polar cap during periods of dayside reconnection'. In: *Journal of Geophysical Research: Space Physics* vol. 120, no. 6, pp. 4452–4464.

Clausen, L. et al. (2016). 'GPS scintillations in the high latitudes during periods of dayside and nightside reconnection'. In: *Journal of Geophysical Research: Space Physics* vol. 121, no. 4, pp. 3293–3309.

Conde, L. (2011). 'An introduction to Langmuir probe diagnostics of plasmas'. In: *Madrid: Dept. Física. ETSI Aeronáut ngenieros Aeronáuticos Universidad Politécnica de Madrid*, pp. 1–28.

Conde, M. et al. (2018). *The Grand Challenge Initiative - Cusp: A campaign of sounding rocket missions to study the multi-scale physics occurring in Earth's geomagnetic cusps*.

Cowley, S. (2000). 'Magnetosphere-ionosphere interactions: A tutorial review'. In: *Magnetospheric Current Systems, Geophys. Monogr. Ser* vol. 118, pp. 91–106.

Crowley, G. et al. (1996). 'Cellular structures in the high-latitude thermosphere'. In: *Journal of Geophysical Research: Space Physics* vol. 101, no. A1, pp. 211–223.

Di Mare, F. et al. (2021). 'Turbulence and Intermittency in the Winter Cusp Ionosphere Studied With the ICI Sounding Rockets'. In: *Journal of Geophysical Research: Space Physics* vol. 126, no. 8, e2021JA029150.

Dungey, J. W. (1961). 'Interplanetary magnetic field and the auroral zones'. In: *Physical Review Letters* vol. 6, no. 2, p. 47.

Dyson, P. and Winningham, J. (1974). 'Top side ionospheric spread F and particle precipitation in the day side magnetospheric clefts'. In: *Journal of Geophysical Research* vol. 79, no. 34, pp. 5219–5230.

Emmert, J., Richmond, A. and Drob, D. (2010). 'A computationally compact representation of Magnetic-Apex and Quasi-Dipole coordinates with smooth base vectors'. In: *Journal of Geophysical Research: Space Physics* vol. 115, no. A8.

ESA and Russell, C. (2023-12-02). *Schematic of the Earth's magnetosphere*.

Evans, D. S. (2000). 'Polar orbiting environmental satellite space environment monitor-2: Instrument descriptions and archive data documentation'. In: *NOAA Technical Memorandum*.

Fæhn Follestad, A. et al. (2020). 'Dayside Field-Aligned Current Impacts on Ionospheric Irregularities'. In: *Geophysical Research Letters* vol. 47, no. 11, e2019GL086722.

Fang, T.-W. et al. (2022). 'Space weather environment during the SpaceX Starlink satellite loss in February 2022'. In: *Space weather* vol. 20, no. 11, e2022SW003193.

Friis-Christensen, E., Lühr, H. and Hulot, G. (2006). 'Swarm: A constellation to study the Earth's magnetic field'. In: *Earth, planets and space* vol. 58, pp. 351–358.

Friis-Christensen, E., Lühr, H., Knudsen, D. et al. (2008). 'Swarm–an Earth observation mission investigating geospace'. In: *Advances in Space Research* vol. 41, no. 1, pp. 210–216.

Frisch, U. and Kolmogorov, A. N. (1995). *Turbulence: the legacy of AN Kolmogorov*. Cambridge university press, Cambridge.

Fuselier, S. et al. (2022). 'Multiple reconnection X-lines at the magnetopause and overlapping cusp ion Injections'. In: *Journal of Geophysical Research: Space Physics* vol. 127, no. 5, e2022JA030354.

Ganguli, G. et al. (1994). 'Coupling of microprocesses and macroprocesses due to velocity shear: An application to the low-altitude ionosphere'. In: *Journal of Geophysical Research: Space Physics* vol. 99, no. A5, pp. 8873–8889.

Gilbert, C. (2017). 'The Kelvin-Helmholtz Instability in Space'. In.

Goertz, C. and Boswell, R. (1979). 'Magnetosphere-ionosphere coupling'. In: *Journal of Geophysical Research: Space Physics* vol. 84, no. A12, pp. 7239–7246.

Goodrum, G., Kidwell, K. and Winston, W. (2009). 'NOAA KLM users guide with NOAA-N,-N-Prime supplement, report'. In: *NOAA, Silver Spring, Md.(Available at http://www2. ncdc. noaa. gov/docs/klm/cover. htm.)*, pp. 488–494.

Guthrie, J., Marchand, R. and Marholm, S. (2021). 'Inference of plasma parameters from fixed-bias multi-needle Langmuir probes (m-NLP)'. In: *Measurement Science and Technology* vol. 32, no. 9, p. 095906.

Hasegawa, A. (1976). 'Particle acceleration by MHD surface wave and formation of aurora'. In: *Journal of Geophysical Research* vol. 81, no. 28, pp. 5083–5090.

Hoang, H. et al. (2018). 'A study of data analysis techniques for the multi-needle Langmuir probe'. In: *Measurement Science and Technology* vol. 29, no. 6, p. 065906.

Hosokawa, K., Moen, J. et al. (2011). 'Decay of polar cap patch'. In: *Journal of Geophysical Research: Space Physics* vol. 116, no. A5.

Hosokawa, K., Shiokawa, K. et al. (2009). 'Relationship between polar cap patches and field-aligned irregularities as observed with an all-sky airglow imager at Resolute Bay and the PolarDARN radar at Rankin Inlet'. In: *Journal of Geophysical Research: Space Physics* vol. 114, no. A3.

Hosokawa, K., Taguchi, S. et al. (2013). 'Two-dimensional direct imaging of structuring of polar cap patches'. In: *Journal of Geophysical Research: Space Physics* vol. 118, no. 10, pp. 6536–6543.

Hysell, D. et al. (1994). 'Steepened structures in equatorial spread F: 1. New observations'. In: *Journal of Geophysical Research: Space Physics* vol. 99, no. A5, pp. 8827–8840.

Iijima, T., Fujii, R. et al. (1978). 'Field-aligned currents in the south polar cusp and their relationship to the interplanetary magnetic field'. In: *Journal of Geophysical Research: Space Physics* vol. 83, no. A12, pp. 5595–5603.

Iijima, T. and Potemra, T. A. (1976a). 'Field-aligned currents in the dayside cusp observed by Triad'. In: *Journal of Geophysical Research* vol. 81, no. 34, pp. 5971–5979.

— (1976b). 'The amplitude distribution of field-aligned currents at northern high latitudes observed by Triad'. In: *Journal of Geophysical Research* vol. 81, no. 13, pp. 2165–2174.

Ivarsen, M. F., Hoang, H. et al. (2019). 'Multineedle langmuir probe operation and acute probe current susceptibility to spacecraft potential'. In: *IEEE Transactions on Plasma Science* vol. 47, no. 8, pp. 3816–3823.

Ivarsen, M. F., Jin, Y. et al. (2019). 'Direct evidence for the dissipation of small-scale ionospheric plasma structures by a conductive E region'. In: *Journal of Geophysical Research: Space Physics* vol. 124, no. 4, pp. 2935–2942.

Ivarsen, M. F., St-Maurice, J.-P. et al. (2021). 'Steepening Plasma Density Spectra in the Ionosphere: The Crucial Role Played by a Strong E-Region'. In: *Journal of Geophysical Research: Space Physics* vol. 126, no. 8, e2021JA029401.

Ivarsen, M. F., Park, J. et al. (2020). 'Observational evidence for the role of Hall conductance in Alfvén wave reflection'. In: *Journal of Geophysical Research: Space Physics* vol. 125, no. 12, e2020JA028119.

Jacobsen, K. et al. (2010). 'A new Langmuir probe concept for rapid sampling of space plasma electron density'. In: *Measurement Science and Technology* vol. 21, no. 8, p. 085902.

Jahn, J.-M. and LaBelle, J. (1998). 'Rocket measurements of high-altitude spread F irregularities at the magnetic dip equator'. In: *Journal of Geophysical Research: Space Physics* vol. 103, no. A10, pp. 23427–23441.

Jin, Y., Kotova, D. et al. (2022). 'Ionospheric Plasma IRregularities-IPIR-data product based on data from the Swarm satellites'. In: *Journal of Geophysical Research: Space Physics* vol. 127, no. 4, e2021JA030183.

Jin, Y., Moen, J. I. and Miloch, W. J. (2014). 'GPS scintillation effects associated with polar cap patches and substorm auroral activity: Direct comparison'. In: *Journal of Space Weather and Space Climate* vol. 4, A23.

— (2015). 'On the collocation of the cusp aurora and the GPS phase scintillation: A statistical study'. In: *Journal of Geophysical Research: Space Physics* vol. 120, no. 10, pp. 9176–9191.

Jin, Y., Moen, J. I., Oksavik, K. et al. (2017). 'GPS scintillations associated with cusp dynamics and polar cap patches'. In: *Journal of Space Weather and Space Climate* vol. 7, A23.

Jin, Y., Spicher, A. et al. (2019). 'Ionospheric plasma irregularities characterized by the Swarm satellites: Statistics at high latitudes'. In: *Journal of Geophysical Research: Space Physics* vol. 124, no. 2, pp. 1262–1282.

Keiling, A. et al. (2003). 'The global morphology of wave Poynting flux: Powering the aurora'. In: *Science* vol. 299, no. 5605, pp. 383–386.

Kelley, M., Knudsen, D. and Vickrey, J. (1991). 'Poynting flux measurements on a satellite: A diagnostic tool for space research'. In: *Journal of Geophysical Research: Space Physics* vol. 96, no. A1, pp. 201–207.

Kelley, M., Pfaff, R. et al. (1982). 'Simultaneous rocket probe and radar measurements of equatorial spread F—Transitional and short wavelength results'. In: *Journal of Geophysical Research: Space Physics* vol. 87, no. A3, pp. 1575–1588.

Kelley, M. C. (2009). *The Earth's ionosphere: Plasma physics and electrodynamics*. Academic press.

Kelley, M. C. et al. (1982). 'On the origin and spatial extent of high-latitude F region irregularities'. In: *Journal of Geophysical Research: Space Physics* vol. 87, no. A6, pp. 4469–4475.

Keskinen, M. J. and Ossakow, S. (1983). 'Theories of high-latitude ionospheric irregularities: A review'. In: *Radio science* vol. 18, no. 06, pp. 1077–1091.

Keskinen, M. and Huba, J. (1990). 'Nonlinear evolution of high-latitude ionospheric interchange instabilities with scale-size-dependent magnetospheric coupling'. In: *Journal of Geophysical Research: Space Physics* vol. 95, no. A9, pp. 15157–15166.

Keskinen, M., Mitchell, H. et al. (1988). 'Nonlinear evolution of the Kelvin-Helmholtz instability in the high-latitude ionosphere'. In: *Journal of Geophysical Research: Space Physics* vol. 93, no. A1, pp. 137–152.

Kinrade, J., Mitchell, C. et al. (2012). 'Ionospheric scintillation over Antarctica during the storm of 5–6 April 2010'. In: *Journal of Geophysical Research: Space Physics* vol. 117, no. A5.

Kinrade, J., Mitchell, C. N. et al. (2013). 'GPS phase scintillation associated with optical auroral emissions: First statistical results from the geographic South Pole'. In: *Journal of Geophysical Research: Space Physics* vol. 118, no. 5, pp. 2490–2502.

Kintner, P. M., Ledvina, B. M. and De Paula, E. (2007). 'GPS and ionospheric scintillations'. In: *Space weather* vol. 5, no. 9.

Kintner, P. M. and Seyler, C. E. (1985). 'The status of observations and theory of high latitude ionospheric and magnetospheric plasma turbulence'. In: *Space science reviews* vol. 41, no. 1, pp. 91–129.

Kivelson, M. G. and Russell, C. T. (1995). *Introduction to space physics*. Cambridge university press.

Knudsen, D., Burchill, J. et al. (2017). 'Thermal ion imagers and Langmuir probes in the Swarm electric field instruments'. In: *Journal of Geophysical Research: Space Physics* vol. 122, no. 2, pp. 2655–2673.

Knudsen, D., Kelley, M. and Vickrey, J. (1992). 'Alfvén waves in the auroral ionosphere: A numerical model compared with measurements'. In: *Journal of Geophysical Research: Space Physics* vol. 97, no. A1, pp. 77–90.

Knudsen, W. (1974). 'Magnetospheric convection and the high-latitude F 2 ionosphere'. In: *Journal of Geophysical Research* vol. 79, no. 7, pp. 1046–1055.

Kolmogorov, A. N. (1941). 'Dissipation of energy in the locally isotropic turbulence'. In: *Dokl. Akad. Nauk. SSSR*. Vol. 32, pp. 19–21.

Kraichnan, R. H. (1967). 'Inertial ranges in two-dimensional turbulence'. In: *The Physics of Fluids* vol. 10, no. 7, pp. 1417–1423.

LaBelle, J., Kelley, M. C. and Seyler, C. E. (1986). 'An analysis of the role of drift waves in equatorial spread F'. In: *Journal of Geophysical Research: Space Physics* vol. 91, no. A5, pp. 5513–5525.

Lai, S. T. (2012). *Fundamentals of spacecraft charging: spacecraft interactions with space plasmas*. Princeton University Press.

Le, G., Slavin, J. and Strangeway, R. (2010). 'Space Technology 5 observations of the imbalance of regions 1 and 2 field-aligned currents and its implication to the cross-polar cap Pedersen currents'. In: *Journal of Geophysical Research: Space Physics* vol. 115, no. A7.

Lilensten, J. and Belehaki, A. (2009). 'Developing the scientific basis for monitoring, modelling and predicting space weather'. In: *Acta Geophysica* vol. 57, no. 1, p. 1.

Lockwood, M. and Carlson Jr, H. (1992). 'Production of polar cap electron density patches by transient magnetopause reconnection'. In: *Geophysical research letters* vol. 19, no. 17, pp. 1731–1734.

Marholm, S. and Marchand, R. (2020). 'Finite-length effects on cylindrical Langmuir probes'. In: *Physical Review Research* vol. 2, no. 2, p. 023016.

Milan, S. E., Lester, M. and Yeoman, T. K. (2002). 'HF radar polar patch formation revisited: Summer and winter variations in dayside plasma structuring'. In: *Annales Geophysicae*. Vol. 20. 4. Copernicus Publications Göttingen, Germany, pp. 487–499.

Moen, J., Carlson, H. et al. (2006). 'EISCAT observations of plasma patches at sub-auroral cusp latitudes'. In: *Annales geophysicae*. Vol. 24. 9. Copernicus GmbH, pp. 2363–2374.

Moen, J., Evans, D. et al. (1996). 'Dayside moving auroral transients related to LLBL dynamics'. In: *Geophysical research letters* vol. 23, no. 22, pp. 3247–3250.

Moen, J., Oksavik, K., Abe, T. et al. (2012). 'First in-situ measurements of HF radar echoing targets'. In: *Geophysical Research Letters* vol. 39, no. 7.

Moen, J., Qiu, X. et al. (2008). 'On the diurnal variability in F2-region plasma density above the EISCAT Svalbard radar'. In: *Annales geophysicae*. Vol. 26. 8. Copernicus GmbH, pp. 2427–2433.

Moen, J., Spicher, A. et al. (2018). 'Grand challenge initiative-cusp: Rockets to explore solar wind-driven dynamics of the top side polar atmosphere'. In: *SESS 2018 The State of Environmental Science in Svalbard*, pp. 184–204.

Moen, J., Oksavik, K., Alfonsi, L. et al. (2013). 'Space weather challenges of the polar cap ionosphere'. In: *Journal of Space Weather and Space Climate* vol. 3, A02.

Moser, C. et al. (2021). 'Modulated Upper-Hybrid Waves Coincident With Lower-Hybrid Waves in the Cusp'. In: *Journal of Geophysical Research: Space Physics* vol. 126, no. 9, e2021JA029590.

Mott-Smith, H. M. and Langmuir, I. (1926). 'The theory of collectors in gaseous discharges'. In: *Physical review* vol. 28, no. 4, p. 727.

Nishimura, Y. et al. (2021). *Cross-scale Coupling and Energy Transfer in the Magnetosphere-ionosphere-thermosphere System*. Elsevier.

Oksavik, K. (2020a). *The University of Bergen global navigation satellite system data collection*.

Oksavik, K., Moen, J., Rekaa, E. et al. (2011). 'Reversed flow events in the cusp ionosphere detected by SuperDARN HF radars'. In: *Journal of Geophysical Research: Space Physics* vol. 116, no. A12.

Oksavik, K., Søraas, F. et al. (2000). 'Optical and particle signatures of magnetospheric boundary layers near magnetic noon: Satellite and ground-based observations'. In: *Journal of Geophysical Research: Space Physics* vol. 105, no. A12, pp. 27555–27568.

Oksavik, K., Moen, J., Lester, M. et al. (Nov. 2012). 'In situ measurements of plasma irregularity growth in the cusp ionosphere'. In: *Journal of Geophysical Research: Space Physics* vol. 117, no. A11, n/a–n/a.

Oksavik, K. (2020b). *Documentation of GNSS Total Electron Content and Scintillation Data (60 s) at Svalbard*. Version V1. DOI: 10.18710/EA5BYX.

Oksavik, K., Meeren, C. van der et al. (2015). 'Scintillation and loss of signal lock from poleward moving auroral forms in the cusp ionosphere'. In: *Journal of Geophysical Research: Space Physics* vol. 120, no. 10, pp. 9161–9175.

Oya, H. and Aso, T. (1969). 'Rocket Observations of Winter Ionosphere by Gyro-Plasma Probe'. In: *Space Technology and Science*, p. 1111.

Ray, V. et al. (2022). 'The impact of space weather on very low Earth orbit (VLEO) satellites'. In.

Resendiz Lira, P. A. and Marchand, R. (2021). 'Simulation inference of plasma parameters from Langmuir probe measurements'. In: *Earth and Space Science* vol. 8, no. 3, e2020EA001344.

Rideout, W. and Coster, A. (2006). 'Automated GPS processing for global total electron content data'. In: *GPS solutions* vol. 10, pp. 219–228.

Rinne, Y. et al. (2007). 'Reversed flow events in the winter cusp ionosphere observed by the European Incoherent Scatter (EISCAT) Svalbard radar'. In: *Journal of Geophysical Research: Space Physics* vol. 112, no. A10.

Sato, T. and Rourke, G. (1964). 'F-region enhancements in the Antarctic'. In: *Journal of Geophysical Research* vol. 69, no. 21, pp. 4591–4607.

Sato, T. (1959). 'Morphology of ionospheric F2 disturbances in the polar regions: A linkage between polar patches and plasmaspheric drainage plumes'. In: *Report of ionosphere and space research in Japan* vol. 13, p. 91.

Schott, L. (1968). 'Electrical probes(Metallic single and double plasma probes, discussing floating potential and ion saturation current)'. In.

Schroeder, J. W. et al. (2021). 'Laboratory measurements of the physics of auroral electron acceleration by Alfvén waves'. In: *Nature communications* vol. 12, no. 1, p. 3103.

Sojka, J. J., Bowline, M. and Schunk, R. W. (1994). 'Patches in the polar ionosphere: UT and seasonal dependence'. In: *Journal of Geophysical Research: Space Physics* vol. 99, no. A8, pp. 14959–14970.

Spicher, A., Deshpande, K. et al. (2020). 'On the production of ionospheric irregularities via Kelvin-Helmholtz instability associated with cusp flow channels'. In: *Journal of Geophysical Research: Space Physics* vol. 125, no. 6, e2019JA027734.

Spicher, A., LaBelle, J. et al. (2022). 'Interferometric study of ionospheric plasma irregularities in regions of phase scintillations and HF backscatter'. In: *Geophysical Research Letters* vol. 49, no. 12, e2021GL097013.

Spicher, A., Miloch, W. and Moen, J. (2014). 'Direct evidence of double-slope power spectra in the high-latitude ionospheric plasma'. In: *Geophysical Research Letters* vol. 41, no. 5, pp. 1406–1412.

Suzuki, T. et al. (2010). 'Sheath capacitance observed by impedance probes onboard sounding rockets: Its application to ionospheric plasma diagnostics'. In: *Earth, planets and space* vol. 62, pp. 579–587.

Treumann, R. A. and Baumjohann, W. (1997). *Advanced space plasma physics*. Vol. 30. Imperial College Press London.

Tröbs, M. and Heinzel, G. (2006). 'Improved spectrum estimation from digitized time series on a logarithmic frequency axis'. In: *Measurement* vol. 39, no. 2, pp. 120–129.

Tsunoda, R. T. (1988). 'High-latitude F region irregularities: A review and synthesis'. In: *Reviews of Geophysics* vol. 26, no. 4, pp. 719–760.

Vickrey, J. F. and Kelley, M. C. (1982). 'The effects of a conducting E layer on classical F region cross-field plasma diffusion'. In: *Journal of Geophysical Research: Space Physics* vol. 87, no. A6, pp. 4461–4468.

Vierinen, J. et al. (2016). 'Statistical framework for estimating GNSS bias'. In: *Atmospheric Measurement Techniques* vol. 9, no. 3, pp. 1303–1312.

Villain, J., Hanuise, C. and Beghin, C. (1986). 'ARCAD3-SAFARI coordinated study of auroral and polar F-region ionospheric irregularities'. In: *Annales Geophysicae*. Vol. 4, pp. 61–68.

Wakabayashi, M., Ono, T. et al. (2005). 'Electron density and plasma waves in mid-latitude sporadic-E layer observed during the SEEK-2 campaign'. In: *Annales Geophysicae*. Vol. 23. 7. Copernicus GmbH, pp. 2335–2345.

Wakabayashi, M., Suzuki, T. et al. (2013). 'Impedance probe technique to detect the absolute number density of electrons on-board spacecraft'. In: *An Introduction to Space Instrumentation*, pp. 107–123.

Weber, E. J. et al. (1984). 'F layer ionization patches in the polar cap'. In: *Journal of Geophysical Research: Space Physics* vol. 89, no. A3, pp. 1683–1694.

Weber, E. et al. (1986). 'Polar cap F layer patches: Structure and dynamics'. In: *Journal of Geophysical Research: Space Physics* vol. 91, no. A11, pp. 12121–12129.

Welch, P. (1967). 'The use of fast Fourier transform for the estimation of power spectra: a method based on time averaging over short, modified periodograms'. In: *IEEE Transactions on audio and electroacoustics* vol. 15, no. 2, pp. 70–73.

Wilhjelm, J., Friis-Christensen, E. and Potemra, T. A. (1978). 'The relationship between ionospheric and field-aligned currents in the dayside cusp'. In: *Journal of Geophysical Research: Space Physics* vol. 83, no. A12, pp. 5586–5594.

Yeh, K. C. and Liu, C.-H. (1982). 'Radio wave scintillations in the ionosphere'. In: *Proceedings of the IEEE* vol. 70, no. 4, pp. 324–360.

Yokota, S., Saito, Y. and Asamura, K. (2023). 'A low-energy particle experiment for both ion and electron measurements using a single microchannel plate detector'. In.

Zhang, Q.-H., Zhang, B.-C., Liu, R.-Y. et al. (2011). 'On the importance of interplanetary magnetic field By on polar cap patch formation'. In: *Journal of Geophysical Research: Space Physics* vol. 116, no. A5.

Zhang, Q.-H., Zhang, B.-C., Moen, J. et al. (2013). 'Polar cap patch segmentation of the tongue of ionization in the morning convection cell'. In: *Geophysical Research Letters* vol. 40, no. 12, pp. 2918–2922.

Chapter 5

Data Acknowledgements

- This dissertation was supported in part by the European Research Council under the European Union's Horizon 2020 research and innovation programme grant 866 357.
- The author acknowledges use of NASA/GSFC's Space Physics Data Facility's OMNIWeb service, and OMNI data.
- GPS TEC data products and access through the Madrigal distributed data system are provided to the community by the Massachusetts Institute of Technology under support from US National Science Foundation grant AGS-1242204. Data for the TEC processing is provided from the following organizations: UNAVCO, Scripps Orbit and Permanent Array Center, Institut Geographique National, France, International GNSS Service, The Crustal Dynamics Data Information System (CDDIS), National Geodetic Survey, Instituto Brasileiro de Geografia e Estatística, RAMSAC CORS of Instituto Geográfico Nacional de la República Argentina, Arecibo Observatory, Low-Latitude Ionospheric Sensor Network (LISN), Topcon Positioning Systems, Inc., Canadian High Arctic Ionospheric Network, Institute of Geology and Geophysics, Chinese Academy of Sciences, China Meteorology Administration, Centro di Ricerche Sismologiche, Système d'Observation du Niveau des Eaux Littorales (SONEL), RENAG : REseau NAtional GPS permanent, GeoNet - the official source of geological hazard information for New Zealand, GNSS Reference Networks, Finnish Meteorological Institute, SWEPOS - Sweden, Hartebeesthoek Radio Astronomy Observatory, Crustal Dynamics Data Information System (CDDIS), Astronomical Institute of the University of Bern, TrigNet Web Application, South Africa, Australian Space Weather Services, RETE INTEGRATA NAZIONALE GPS, Estonian Land Board, and Virginia Tech Center for Space Science and Engineering Research (Rideout and Coster 2006; Vierinen et al. 2016).
- EISCAT is an international association supported by research organisations in China (CRIRP), Finland (SA), Japan (NIPR and ISEE), Norway (NFR), Sweden (VR), and the United Kingdom (UKRI).
- The Swarm data, including the IPIR data set, can be accessed at https://swarm-diss.eo.esa.int. Information about the data sets can be taken from the Swarm Data Handbook at https://swarmhandbook.earth.esa.int.
- The Total Electron Content (TEC) and scintillation data is from The University of Bergen Global Navigation Satellite System Data Collection

(Oksavik 2020a). Documentation of the data products is given by Oksavik 2020b.

- Data from Hornsund have been acquired at the Polish Polar Station Hornsund in collaboration with the Institute of Geophysics, Polish Academy of Sciences.

Papers

Paper I

The role of particle precipitation on plasma structuring at different altitudes by in-situ measurements

Lisa M. Buschmann, John W. Bonnell, Scott Bounds, Lasse B.N. Clausen, Craig Kletzing, Sigvald Marholm, Wojciech J. Miloch, Roger Roglans, Andres Spicher

Published in Journal for Space Weather and Space Climate.
https://doi.org/10.1051/swsc/2023012

J. Space Weather Space Clim. 2023, **13**, 13
© L.M. Buschmann et al., Published by EDP Sciences 2023
https://doi.org/10.1051/swsc/2023012

JSWSC
Available online at:
www.swsc-journal.org

Topical Issue - Ionospheric plasma irregularities and their impact on radio systems

RESEARCH ARTICLE OPEN ACCESS

The role of particle precipitation on plasma structuring at different altitudes by in-situ measurements

Lisa M. Buschmann[1,*], John W. Bonnell[2], Scott Bounds[3], Lasse B.N. Clausen[1], Craig Kletzing[3], Sigvald Marholm[1,4], Wojciech J. Miloch[1], Roger Roglans[2], and Andres Spicher[5]

[1] Department of Physics, University of Oslo, Problemveien 7, 0315 Oslo, Norway
[2] Space Sciences Laboratory, University of California Berkeley, 7 Gauss Way, Berkeley, CA 94720, USA
[3] University of Iowa, Iowa City, IA 52242, USA
[4] Department of Computational Materials Processing, Institute for Energy Technology, Instituttveien 18, 2007 Kjeller, Norway
[5] Department of Physics and Technology, The Arctic University of Norway, Klokkargårdsbakken 35, 9019 Tromsø, Norway

Received 21 September 2022 / Accepted 21 April 2023

Abstract – The plasma in the cusp ionosphere is subject to particle precipitation, which is important for the development of large-scale irregularities in the plasma density. These irregularities can be broken down into smaller scales which have been linked to strong scintillations in the Global Navigation Satellite System (GNSS) signals. We present power spectra for the plasma density irregularities in the cusp ionosphere for regions with and without auroral particle precipitation based on in-situ measurements from the Twin Rockets to Investigate Cusp Electrodynamics-2 (TRICE-2) mission, consisting of two sounding rockets flying simultaneously at different altitudes. The electron density measurements taken from the multi-needle Langmuir probe system (m-NLP) were analyzed for the whole flight duration for both rockets. Due to their high sampling rates, the probes allow for a study of plasma irregularities down to kinetic scales. A steepening of the slope in the power spectra may indicate two regimes, a frequency interval with a shallow slope, where fluid-like processes are dominating, and an interval with a steeper slope which can be addressed with kinetic theory. The steepening occurs at frequencies between 20 Hz and 100 Hz with a median similar to the oxygen gyrofrequency. Additionally, the occurrence of double slopes increases where precipitation starts and throughout the rest of the flight. In addition, strong electron density fluctuations were found in regions poleward of the cusp, thus in regions immediately after precipitation. Furthermore, by investigating the integrated power of the fluctuations within different frequency ranges, we show that at low frequencies (10–100 Hz), the power is pronounced more evenly while the rocket encounters particle precipitation, while at high frequencies (100–1000 Hz) fluctuations essentially coincide with the passing through a flow channel.

Keywords: Energetic particle precipitation / Ionosphere / Ionospheric irregularities / Plasma density / Power spectral density

1 Introduction

The high-latitude ionosphere is subject to plasma structures over a wide range of scales from 100 km down to meter-sized structures (Basu et al., 1990; Tsunoda, 1988). Smaller scale irregularities can modulate trans-ionospheric radio waves, leading to rapid fluctuations in the received phase and amplitude which are often referred to as scintillations (Carlson, 2012). Thereby, plasma structuring can disturb satellite communication systems, which may cause navigation errors or a failure of signal acquisition (Kintner et al., 2007; Yeh and Liu, 1982). Global navigation satellite systems (GNSS) play an important role in operating aviation and marine traffic and are becoming more and more important due to higher human activity in the polar regions. Thus, more effort has been put into understanding the formation of plasma irregularities on small scales in the ionosphere in recent years (e.g. Jin et al., 2014; Kintner et al., 2007; Moen et al., 2013; Oksavik et al., 2012).

A number of different sources have been suggested for the formation of irregularities, for example, the gradient drift instability (GDI) and the Kelvin-Helmholtz instability (KHI) (Kintner & Seyler,1985; Tsunoda, 1988; Basu et al., 1990; Keskinen & Ossakow, 1983). The GDI has its origin in the different drifts of ions and electrons in steep density gradients and is

*Corresponding author: lisa.buschmann@fys.uio.no

the dominant instability occurring in polar cap patches, regions of 100 km scale with at least twice the density as the background plasma (Crowley et al., 1996; Tsunoda, 1988). The KHI is rather driven by velocity shears in the plasma and, on the dayside, a two-step process has been proposed, where the KHI is first structuring the plasma patch entering the polar cap on which the GDI can then effectively act and further structure the patch (Carlson et al., 2007; Moen et al., 2013).

The plasma in the cusp ionosphere is subject to auroral particle precipitation, which is thought to be an important source of large-scale irregularities with long lifetimes (Kelley et al., 1982b; Moen et al., 2002, 2013). These irregularities are able to convect over large areas and can thus be further structured by the GDI and KHI (Moen et al., 2012). Recently Jin et al. (2015) found that strong scintillations can be related to particle precipitation and the cusp aurora.

Power spectra are a common tool to analyze instabilities and turbulence in a plasma, describing the cascading of the energy in the system (Frisch & Kolmogorov, 1995). It has been suggested that ionospheric plasma instabilities should be described by power laws (Kintner & Seyler, 1985; Tsunoda, 1988) and different mechanisms are thought to result in different slopes in the spectra. Past observations suggested a slope of $p \approx -5/3$ for the initial spectral index before the steepening occurs (Kintner & Seyler, 1985). In situ measurements of the ionosphere made it possible to show that power spectra of plasma fluctuations exhibit a steeper slope for higher frequencies when plotted logarithmically. This slope steepening has been first documented for the low-latitude ionosphere with sounding rockets and satellites (Kelley et al., 1982b) and is well observed in this region (e.g. LaBelle et al. 1986; Hysell et al. 1994; Jahn & LaBelle, 1998). High-resolution measurements made it possible to show this steepening for the high-latitude F-region (Villain et al., 1986; Basu et al., 1990; Spicher et al., 2014; Ivarsen et al., 2019; Di Mare et al., 2021). The spectral index in the high-latitude ionosphere has been shown to be close to $p_1 \approx -5/3$ at low frequencies and around $p_2 \approx -3$ to $p_2 \approx -5$ for high frequencies in these works. The frequencies of the spectral break have been studied for decades along with the steepening of the spectrum, but observed at a variety of different frequencies. It is still mostly unknown as to what frequency the break occurs (Tsunoda,1988), thus, this is still of importance.

A conducting E region was found to speed up the diffusion of plasma structures in the F region (Kelley et al., 1982a, 1982b; Basu & Coppi, 1988). Additionally, electric coupling between the two regions along the magnetic field lines leads to a way for electrons to transfer between them. It was found that this coupling with a highly conductive E-region leads to a faster decay of plasma structures in the F-region compared to a less conducting E-region (Kelley et al., 1982b; Ivarsen et al., 2019). In this paper, we present results from the TRICE-2 flights, consisting of two sounding rockets flying simultaneously at different altitudes. We compare intervals with and without particle precipitation for both altitudes and investigate the differences in power spectra between these regions. While power spectra with double slopes in regions of strong fluctuations have been investigated before, the TRICE-2 campaign allows for the first time a simultaneous study at two different altitudes. We were able to confirm the spectral indices for power spectra in the ionosphere mentioned above. Additionally, we show that a double slope starts appearing when the rocket enters the cusp, but the spectral break frequency rather follows a variation in the electric field. Furthermore, through analysis of the integrated power within the power spectra analysis, we can show that lower frequencies, thus larger scales, are more elevated during precipitation, while higher frequencies, or smaller scales, are elevated during a rise in an electric field.

The paper is divided as follows: Section 2 presents the TRICE-2 sounding rockets and the instruments on board used in this work, with an emphasis on the multi-needle Langmuir probe. Section 3 gives a brief overview of the flight conditions and the results which focus on spectral analysis of the electron density data placed in the context of observations from other instruments. Finally, the results are discussed in Section 4 and a conclusion is given in Section 5.

2 Instrumentation

2.1 TRICE-2 Sounding Rockets

The Twin Rockets to Investigate Cusp Electrodynamics (TRICE-2) mission is a NASA mission that is part of the Grand Challenge Initiative – Cusp (GCI – Cusp) (Moen et al., 2018). The mission consists of two rockets flying simultaneously, and shall hence be called the low flyer (52.004) and high flyer (52.003), with respect to their altitudes. The rockets were launched on December 8th, 2018 from Andøya Space Center in Andøya, Norway, located at 69°17' N, 16°01' E. The high flyer was launched at 08:26:00 UT and reached its apogee at 1042.2 km at 08:37:16 UT or 676 s after launch. The low flyer was launched at 08:28:00 UT and reached its apogee at 756.8 km at 08:37:46 UT or 586 s after launch.

2.2 Multi-Needle Langmuir Probe (m-NLP)

We used data from the multi-needle Langmuir probe (m-NLP), which can be used to calculate the electron density with very high sampling rates. For a set of cylindrical probes, the electron density n_e can be acquired from

$$n_e = \left(\frac{m_e}{2e(2erl)^2} \frac{d\left(I_c^2\right)}{dV} \right)^{\frac{1}{2}}, \quad (1)$$

where m_e is the electron mass, e the elementary charge, r and l the probe radius and length, respectively, I_c the current collected by a single probe, and V the respective probe bias (Jacobsen et al., 2010; Bekkeng et al., 2010). The factor $\beta = 1/2$ is for an infinitely long, cylindrical probe, thus if the squared currents drawn to each probe are plotted against the corresponding probe biases, the electron density can be obtained from the slope of a line in this plot. For a probe deviating from this geometry, the factor differs from $\beta = 1/2$ (Marholm & Marchand, 2020). The obtained electron density for a probe with $\beta = 1/2$ is then independent of the spacecraft potential and the electron temperature. However, for $\beta \neq 1/2$, n_e may be affected by changes in the floating potential and temperatures. The absolute density obtained with a $\beta \neq 1/2$ has been observed to be off by 20–45% compared with $\beta = 1/2$, while simulations have found an overestimation of the density by up to an order of magnitude (Hoang et al., 2018; Guthrie et al., 2021).

Both rockets used in this work were equipped with one probe system each, which consisted of four cylindrical probes with a diameter and length of 0.51 mm and 39 mm, respectively. The probes allowed to calculate the electron density at a sampling rate of 10 kHz using probes with fixed biases of 3 V, 4.5 V, 6 V, and 7.5 V. The probes were mounted in a cross-like formation perpendicular to the spacecraft axis with a distance of 1 m between oppositely mounted probes.

In addition to the m-NLP, we present data from the DC electric field instruments (DC **E**), an on-board magnetometer, and the Energy and Pitch Angle Analyzer (EEPAA) on both rockets and 557.7 nm and 630 nm emission lines from the all-sky imager (ASI) which is based in Ny Ålesund, Norway. The ASI was calibrated at the UNIS calibration lab in Longyearbyen in January 2013. Further information about the brightness and orientation calibration is given on the ASI data page of the University of Oslo.[1]

The DC **E** is composed of four spherical probes in a similar formation as the m-NLP with a distance of 6.5 m between two opposing probes, the probes were able to measure the electric field with a cadence of 2.5 kHz. The filtered data used is in geographic coordinates and was filtered with a lowpass Butterworth filter at 1 Hz. The magnetic field was measured by a magnetometer that measured the three-axis magnetic field components for the duration of the flight in geographic coordinates. We assume both measurements to have an error of around 5%, which arises due to uncertainties in the geometries, the deployment of the instruments, and noise. The EEPAA consisted of several detectors mounted in 10° steps around the spacecraft axis, where 0° corresponded to the upward direction. We used the 0° data from the EEPAA, which shows the electrons precipitating downwards along the magnetic field lines.

3 Observations

Measurements of the interplanetary magnetic field show a steady negative B_z of ≈ -5 nT prior to launch (Moser et al., 2021). The background auroral observations can be seen in Figure 1, which shows the ASI data for the 630 nm (upper row) and 557.7 nm (lower row) emission from Ny Ålesund at different times while the rockets were intersecting the cusp region. The data were projected onto a height of 250 km for the red (630 nm) and 150 km for the green (557.7 nm) emission line. The green and dark blue for the upper panel and orange and magenta lines lower panel indicate the trajectories and the colored triangles and squares for the low and high flyers, respectively, show the current position of the rockets. The trajectory of the high flyer is the left trajectory, and the low flyer trajectory is the right trajectory. The black arrows protruding from the trajectories in the two left panels show the electric field vector in the E_E-E_N-plane in geographic coordinates taken from the DC **E** instrument with a cadence of 2.5 kHz. The arrow lengths show the magnitude of the electric field in arbitrary units but are both scaled with the same factors, and the length can therefore be taken as an indicator of the field strength. For visibility reasons, the electric field for the high flyer is only depicted in the upper panel, while the field vectors for the low flyer are only depicted in the lower panel. While it was partly cloudy, it can be seen that both flyers were launched into dayside aurora and intersected the cusp regions, which are dominated by red emission. The high flyer entered the cusp around 08:35 UT and the low flyer around 08:37 UT. The rockets exit the region again towards the end of the flight. The electric field vectors show a mostly westward electric field for both rockets with a growing northward component for the low flyer until the rockets enter the cusp, where the field abruptly changes to a south-eastward direction and intensifies.

Figure 2 shows the electron densities and detrended electron densities of the high and low flyer, respectively, obtained from the m-NLP. For the calculation of the electron density, the spin frequency and harmonic frequencies were removed using bandpass filters. The data was then detrended using a 5th-order Savitzky-Golay filter with a 3-second interval. Note that two intervals in each panel are marked in transparent blue. Due to attitude changes of the rockets, the data collected in these intervals includes artificial spikes in density fluctuations. These transparent overlays will be used for all data sets derived from the density in this work. The electron density for the high flyer (Fig. 2a) shows values between 2 and 9×10^9 m^{-3} with peaks starting around 08:35 UT and ending around 08:39:30 UT. The detrended density for the high flyer (Fig. 2b) shows fluctuating values up to 3×10^9 m^{-3}, with small fluctuations up until 08:37 UT and larger fluctuations until 08:39:30 UT. The electron density for the low flyer (Fig. 2c) shows higher densities between 4×10^9 m^{-3} and 2×10^{10} m^{-3} with two peaks around 08:38 UT and 08:40 UT with densities up to 1.5 and 2×10^{10} m^{-3}, respectively. The detrended density (Fig. 2d) shows fluctuating values up to 5×10^9 m^{-3} with smaller fluctuations until 08:35:30 UT followed by stronger fluctuations until 08:42 UT.

In order to analyze the electron density fluctuations, the detrended density was Fourier transformed using the Fast Fourier Transform (FFT) and a Hanning window with intervals of 2 s each, which corresponds to 20,000 collected samples and to a flight distance up to 8 km, and an overlap of 50% for the windows. Typical power spectra obtained for these intervals plotted in log-log scale can be seen in Figure 3 in the bottom panels. The figure also shows the current collected by each of the Langmuir probes (upper panels) and the corresponding detrended electron density (middle panels). For each 2 s interval, we analyzed if the best fit was one or two straight lines and, in the latter case, at which frequency the spectral break occurred. The fitting was done using a first-order polynomial fit on log-log axes. The start and end points of the fitted interval and a possible break point were first chosen through manual iteration of possible values to get a frequency range in which breakpoints occur. Afterwards, the start, break, and endpoints were chosen from a range of frequencies deemed possible for each of the points. The ranges for each point were between 1 Hz and 10 Hz, between 20 Hz and 100 Hz, and 120 Hz and 250 Hz for the start, break, and endpoints, respectively. The points were chosen by a loop of iterations over the possible frequencies. Then it was examined if the slopes of the two fits were deviating by more than 0.8, and if the low-frequency (LF) slope p_1 had a lower absolute value than the high-frequency (HF) slope p_2. If this was the case, the power spectrum was considered to show a double slope. If the deviation was smaller

[1] All-Sky Imager Data from Ny Ålesund, Svalbard, University of Oslo, http://tid.uio.no/plasma/aurora/tech.html, Date accessed: 2022-11-29.

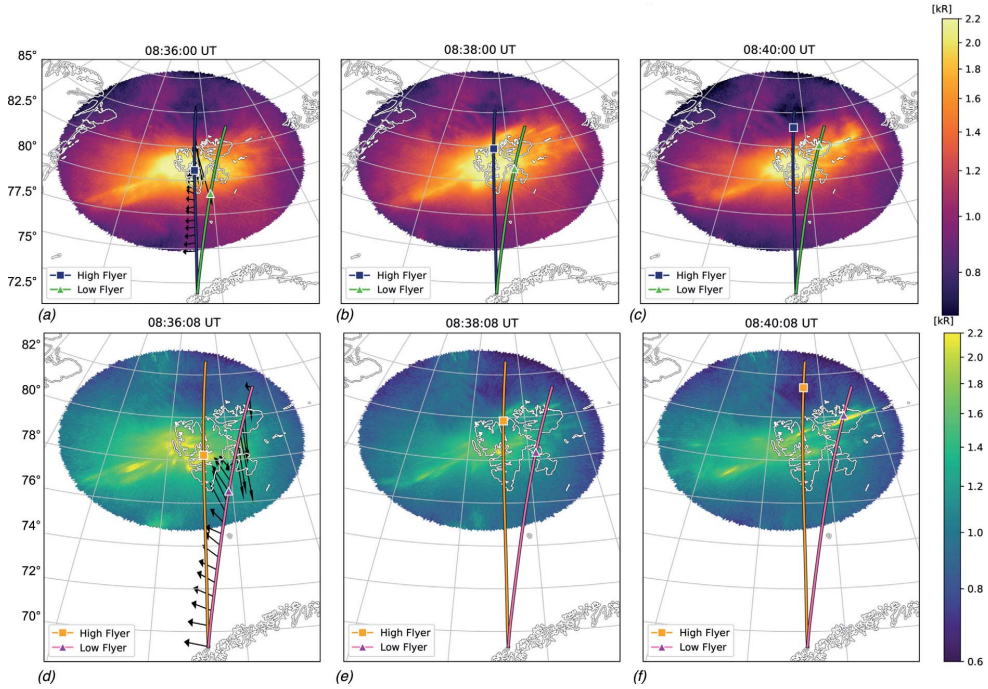

Figure 1. 630 nm (upper row) and 557.7 nm (lower row) All-Sky Imager Data from Ny Ålesund projected to 250 km at 08:36 UT (a), 08:38 UT (b), and 08:40 UT (c) for the 630 nm emission, and projected to 150 km at 08:36 UT (d), 08:38 UT (e), and 08:40 UT(f) for the 557.7 nm emission; the rocket trajectories are shown in dark blue and orange for the high flyer and in green and magenta for the low flyer, respectively. A filled square and filled triangle is indicating the current position for the high and low flyer, respectively. The black arrows indicate the electric field vector obtained from the DC **E** for the high flyer (upper left panel) and the low flyer (lower left panel).

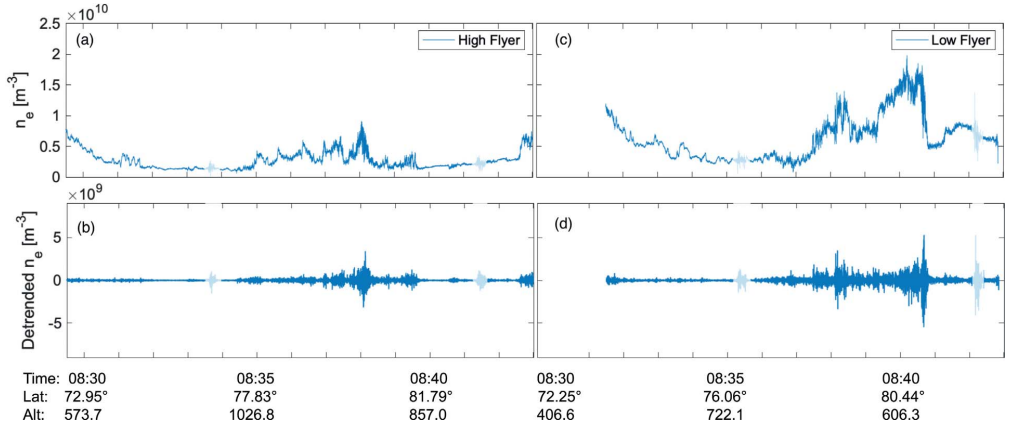

Figure 2. (a) Electron density of the high flyer measured with the m-NLP, (b) detrended electron density of the high flyer, (c) electron density of the low flyer, measured with the m-NLP, (d) detrended electron density of the low flyer; the density was detrended using a 5th-order Savitzky-Golay filter. The transparent data intervals correspond to attitude changes of the spacecraft. The *x*-axes correspond to UT (upper line), the magnetic footprint of the spacecraft (middle line), and the altitude of the rocket (bottom line).

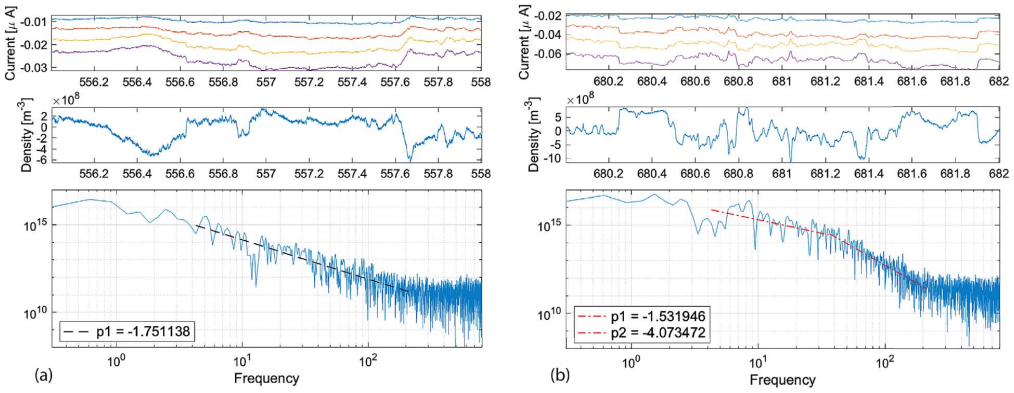

Figure 3. Detrended electron density obtained from the m-NLP, and the corresponding power spectrum for the flight interval between 556 s and 558 s (a) and 680 s and 682 s (b) of the low flyer. The bottom panel in (a) shows a power spectrum with a single slope of $p = -1.97$, while the bottom panel in (b) shows a power spectrum fitted with two slopes $p_1 = -1.64$ and $p_2 = -4.10$.

than 0.8 the spectrum was best described by a single slope. $|p_1| + 0.8 \leq |p_2|$ was found to be a good condition to distinguish between a double and single slope fit and was used as a condition in previous works (Ivarsen et al., 2021). Figure 3a shows the power spectrum of the low flyer at 08:37:16–08:37:18 UT, which corresponds to a time shortly after the rocket entered the cusp. This power spectrum was best described by a single slope fit calculated to be $p_1 = -1.97$. Figure 3b shows the power spectrum of the low flyer at 08:39:20–08:39:22 UT, which corresponds to the rocket being in the middle of the auroral region. This power spectrum exhibited a spectral break at $f \approx 38$ Hz and was thus best described by two different first-order fits calculated to be $p_1 = -1.64$ and $p_2 = -4.10$.

In order to analyze the entire flight and compare data from different instruments, Figure 4 shows the data obtained from the high flyer (left) and low flyer (right). For completeness, Figures 4a and 4b show the detrended electron density for the flight duration (compare Fig. 2). Figures 4c and 4d show the corresponding spectrograms obtained with an FFT and a Hanning window using 20,000 data points, which corresponds to 2 s intervals. The spectrogram shows the frequency range 15–1000 Hz. It can be seen that a high PSD up to 1000 Hz is reached in distinct areas corresponding to the electron density fluctuations mentioned above for both rockets. The white crosses show the frequencies of the spectral knee of the corresponding power spectrum, where a double slope fit was best to fit the spectrum. A clear connection between strong electron density fluctuations and the appearance of a double slope can be seen and generally, the power spectra of the low flyer show more double slopes compared to the high flyer. The spectral breaks for both rockets are located between 20 Hz and 105 Hz. While the highest frequencies are around 90 Hz or 100 Hz, the median spectral break for high and low flyers are located at $f_{\mathrm{HighFlyer}} \approx 45$ Hz and $f_{\mathrm{LowFlyer}} \approx 46$ Hz, respectively. The spectral break at around 08:33:30 UT in Figure 4c falls into the transparent interval indicating the attitude change and could therefore be artificial. Note also that the spectrogram does not show values below 15 Hz. The low flyer showed one spectral break below 15 Hz, which is thus not depicted in this figure. For the low flyer the spectral break frequency exhibits a local maximum of ≈80 Hz at around 08:38:00 UT and a global maximum of ≈104 Hz at roughly 08:40:00 UT. Then the occurrence of double slopes abruptly stops for about half a minute, until at around 08:41:00 UT when the rocket encounters another small region of double slopes. Then, for the rest of the flight, the power spectra only exhibit single slopes. For the high flyer, the spectral break frequencies exhibit one maximum of ≈100 Hz at roughly 08:38:00 UT, similar to the first maximum of the low flyer. While the occurrence of double slopes more or less abruptly stops around 08:40:00 UT, a region with double slopes exists at the very end of the flight, exhibiting very large discrepancies in their fitted slopes (see Fig. 4e). Figures 4e and 4f show the HF and LF slopes for the fit of the power spectra in blue and red, respectively. If only the HF slope is seen with no corresponding LF slope, a single slope was detected. The median slopes for the high and low flyers, respectively, were found to be −1.83 and −1.85 for the low-frequency slope and −3.03 and −3.07 for the HF slope. The median for the single slope spectra is −1.98 and −2.08 for the high and low flyers, respectively. While for the high flyer, the slopes seem to fluctuate around $p = -2$, with no larger intervals of consecutive double slopes, the low flyer shows larger regions, where several double slopes are detected in a row, see Figure 4f between 08:38 and 08:39 UT and around 08:40 UT. The appearance of a double slope naturally coincides with the spectral breaks seen in the previous Figures 4c and 4d. The appearance of double slopes and thus, spectral breaks rises with the beginning of electron precipitation (see Figs. 4k and 4l), but does not subside right after the rockets leave the auroral region.

In addition to the slope of the fitted power spectrum, we investigated the power associated with different frequency regimes for each power spectrum, in order to understand how the power is distributed in the different frequency bands at different altitudes. For this, we integrated the power spectra with respect to frequency. Figures 4g, 4h, 4i, and 4j show the normalized integrated power spectra for 10 Hz and 100 Hz intervals, respectively. For each power spectrum, the power was integrated for 10 Hz intervals between 10 Hz and 100 Hz

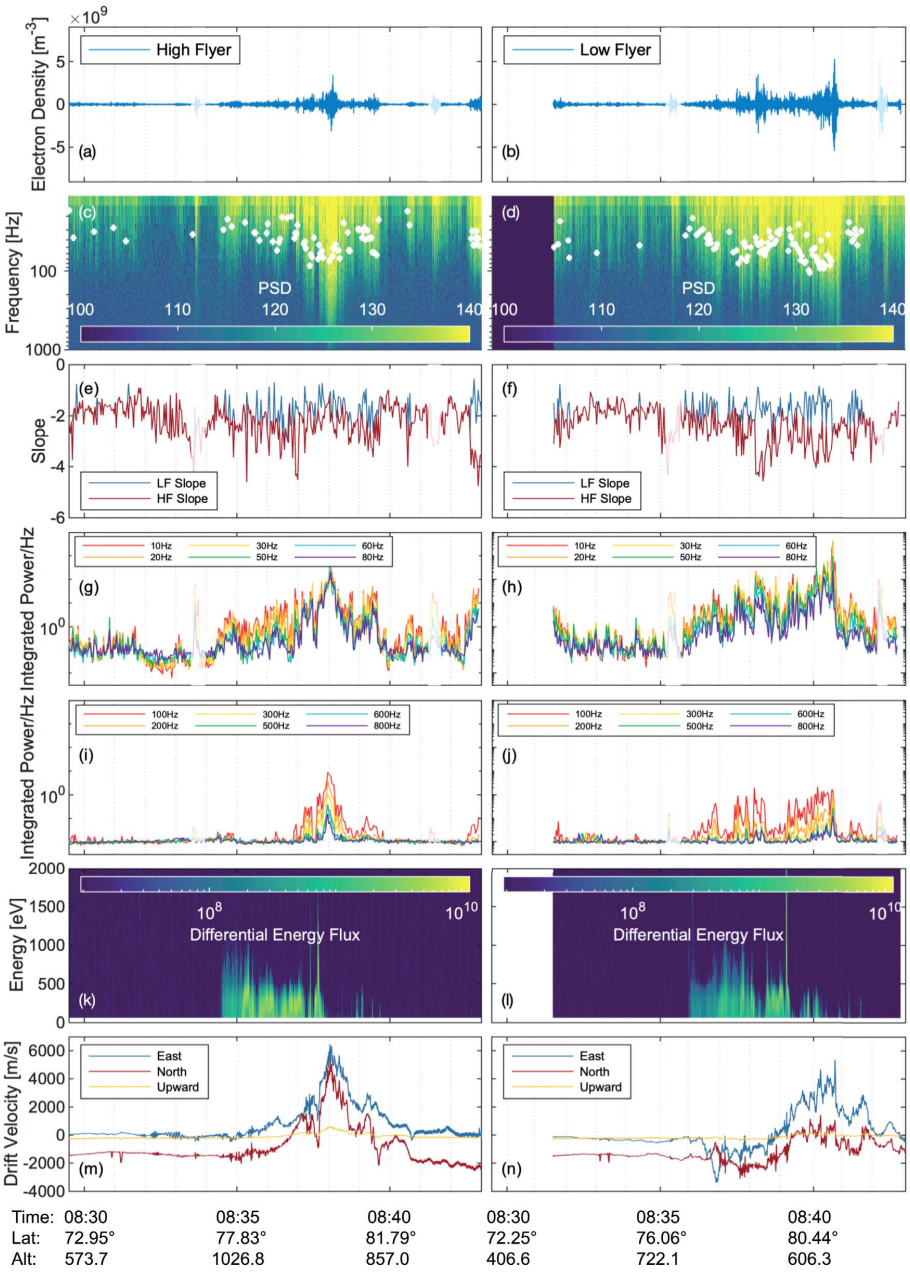

Figure 4. Detrended n_e (**a**, *b*), PSD of the m-NLP n_e fluctuations with the spectral break frequency (**c**, *d*), LF ad HF slopes of the corresponding PSD (**e**, *f*), integrated power from the PSD for frequency intervals of 10 Hz (**g**, *h*) and for intervals of 100 Hz (**i**, *j*), electron precipitation measured with the EEPAA (**k**, *l*) $E \times B$-drift velocity v_D in ENU-coordinates (**m**, *n*) of the **high flyer** and *low flyer*, respectively. The transparent data intervals correspond to attitude changes of the spacecraft. The *x*-axes correspond to UT (upper line), the magnetic footprint of the spacecraft (middle line), and the altitude of the rocket (bottom line).

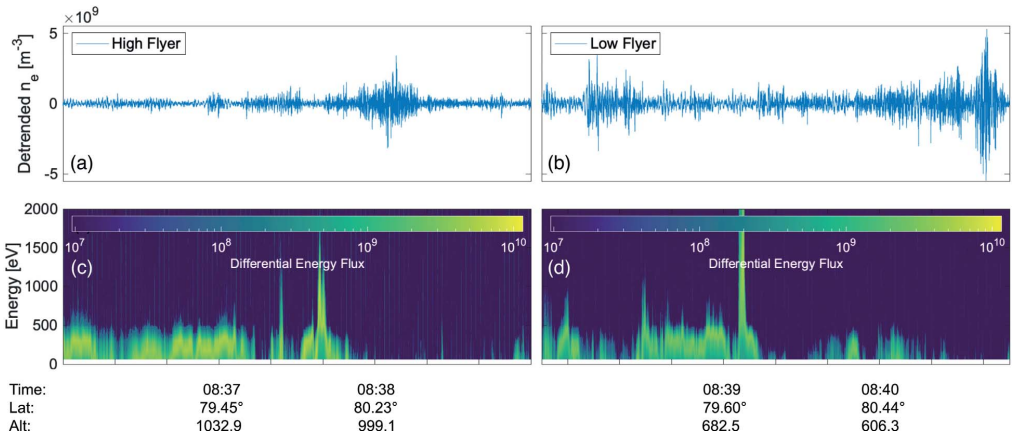

Figure 5. Detrended electron density and electron precipitation of the high flyer (a, c) and the low flyer (b, d) between 08:36:30 and 08:39:00 UT and between 08:38:00 and 08:41:00 UT, respectively. The *x*-axes correspond to UT (upper line), the magnetic footprint of the spacecraft (middle line), and the altitude of the rocket (bottom line).

(Figs. 4g and 4h), and 100 Hz intervals between 100 Hz and 1000 Hz (Figs. 4i and 4l). The values were then normalized with two different factors. The first factor was the length of the integration interval, which was 10 Hz for Figures 4g and 4h and 100 Hz for Figures 4i and 4j. This was done in order to normalize power to power per Hz, so all four panels could be compared in an easier manner. As the power in the spectrum falls off, naturally intervals with lower frequencies have higher powers. In order to compare all frequency intervals with each other, the intervals were normalized by a median power value which was obtained from the whole flight duration used. The normalization factors for each frequency interval for both flyers and a detailed description of the normalization process can be seen in Table A1 in Appendix.

As seen in Figures 4g and 4h, the integrated power at frequencies between 10 Hz and 100 Hz shows similar relative fluctuations, but overall more elevated power with more fluctuations throughout the flight, especially while the rocket is flying through the cusp. While for the low flyer, the power rises for all frequencies, the high flyer shows a rise in power mainly in the lower frequencies. The frequency intervals between 100 Hz and 1000 Hz behave differently (Figs. 4i and 4j). For the high flyer (Figs. 4i) the strongest relative fluctuations are found right after particle precipitation ends at 08:38:00 UT (Fig. 4k), which shows the differential energy flux of precipitating electrons) and coincide with entering a flow channel (see Fig. 4m showing the $\mathbf{E} \times \mathbf{B}$-drift velocity in ENU-coordinates). Outside of that time interval, there are hardly any fluctuations seen for intervals above 100 Hz. For the low flyer (Fig. 4j), the 100 and 200 Hz frequencies are enhanced much stronger than frequencies between 300 Hz and 1000 Hz the strongest fluctuations exist between 08:36 UT and 08:41 UT. While some of the peaks in integrated power fall into regions with little detected particle precipitation, the overall region where the integrated power is elevated coincides well with electron precipitation and, similar to the high flyer, the immediate region afterwards. Additionally, the integrated power of the low flyer correlates with a change in electric field and a change in particle velocity, especially for the second rise of integrated power around 08:39 UT.

Figures 4k and 4l show the electron particle precipitation for the high and low flyers, respectively. For the high flyer, the precipitation starts around 08:34:30 UT with values up to 1000 eV which drops to around 500 eV roughly a minute later. The region of precipitation ends around 08:38:00 UT, except for a few low energetic detected particles around 08:39:00 UT. Precipitation for the low flyer starts at 08:36:00 UT with energies around 500 eV and raises to energies around 1000 eV at 08:37:00 UT. The region of precipitation lasts until about 08:39:00 UT, and just like the high flyer, small regions with low energetic precipitation show up until 08:41:30 UT. Both the high and low flyer have precipitation gaps in the regions of strongest precipitation, and just before the rocket leaves the regions, a strong, thin peak is found with energies up to 2000 eV for the high flyer and 4000 eV for the low flyer. Figures 4m and 4n show the E × B-drift velocity in ENU-coordinates for the high and low flyer, respectively. The drift velocity was calculated from the DC *E* instrument and the magnetometer on board each of the rockets. As the magnetic field and electric field measurements were not taken at the exact same time, the magnetic field was interpolated to estimate the magnetic field values at the time the electric field was obtained. Due to the high cadence and thus low distance between the measurement points, the interpolation was one using a first-order polynomial between each point. The drift velocity was then obtained from $\mathbf{v_D} = \mathbf{E} \times \mathbf{B}/B^2$ the drift velocity for the high flyer (Fig. 4m) shows a southward flow of around 1.5 km s^{-1} with a small eastward component. At about 08:36:00 UT the flow turns into the north-east directions with a drift velocity up to 7 km s^{-1} which is reached at 08:38:00 UT. Afterwards, the flow goes back into the original southeast direction with a velocity of 2 km s^{-1} for the rest of the flight. The drift velocity for the low flyer starts similar to the high flyer with a southward flow of around 1.5 km s^{-1}. The direction of flow turns southwest around

08:36:30 UT and then changes to an eastward flow with peaks between 08:40:00 and 08:41:00 UT with a velocity of roughly 6 km s^{-1}. Afterwards, similarly to the high flyer, it goes back to the original direction and speed.

Figure 5 shows the detrended electron density and the electron precipitation for the high and low flyer. The strongest electron density fluctuations can be seen around 8:38:00 UT for the high flyer and around 08:40:40 UT for the low flyer. The low flyer also exhibits density fluctuations around 08:38 UT. It can be seen that there is a correlation between high electron density fluctuations and low detected precipitation and the largest density fluctuations happen right after the rockets leave the auroral region.

4 Discussion

Irregularities can occur in the ionosphere when free energy is introduced into the system and is then redistributed over a variety of scales until the free energy is dissipating on small spatial scales. One source of free energy in the ionosphere is the influx of energetic particle precipitation (Kelley et al., 1982b; Moen et al., 2002, 2013).

The TRICE-2 sounding rockets encountered energetic electrons at different altitudes. In order to analyze fluctuations in the electron density, power spectra were made for both flights. It has been shown that power spectra of plasma fluctuations in the high-latitude ionosphere display a steeper slope for higher frequencies if plotted logarithmically (Villain et al., 1986; Basu et al., 1990; Spicher et al., 2014; Ivarsen et al., 2019; Di Mare et al., 2021). We found that a double slope for the PSD started appearing at the same time that both the high and low flyers entered the region where particle precipitation was encountered. While particle precipitation seems to in a way trigger the presence of double slopes, the overall distribution of their appearance and the corresponding spectral break frequency does not seem to follow the precipitation. Instead, the frequency of the break in the double slope seems to follow the magnitude of the measured electric field. While the frequencies of the spectral breaks fall between 20 and 105 Hz, the largest values are reached when the electric field also reaches its maximum. This holds true for both the high and low flyers. While the appearance of double slopes seems to coincide with the beginning of precipitation, there are still double slopes found minutes after the rocket leaves the auroral region again, though the rate of occurrence lessens. The low flyer shows a gap around 08:41 UT for about half a minute where no double slopes are detected before another set of double slopes is found. While there are no double slopes registered at the end of the flight interval for the low flyer, the high flyer exhibits an increase of double slopes with a very steep p_2. This corresponds to a region where the rocket encounters a highly structured plasma with an increased density far into the polar cap. The appearance of double slopes during strong electron density fluctuations is in accordance with earlier measurements (Spicher et al., 2014; Ivarsen et al., 2019; Di Mare et al., 2021).

The median values of the LF and HF slopes are −1.83 and −3.03 for the high flyer and −1.85 and −3.07 for the low flyer, respectively. These slopes are in accordance with earlier results that found an LF slope of ≈5/3 and an HF slope between 3 and 5 (Villain et al., 1986; Basu et al., 1990; Spicher et al., 2014; Ivarsen et al., 2019; Di Mare et al., 2021). The median frequencies of the spectral breaks are found to be around 45 Hz for both rockets and are reasonably close and could correlate to the oxygen gyrofrequency found at these heights, which are between $\omega_{\mathrm{HighFlyer}} \approx 33$–$38$ Hz and $\omega_{\mathrm{LowFlyer}} \approx 39$–$45$ Hz for the main duration of the flights for the high and low flyer, respectively. However, the frequencies of the spectral breaks have been observed for decades and found at several different frequencies, thus it is difficult to assume the physical meaning behind the break frequency. The rise in spectral break frequency along with the rise in electric field magnitude or drift velocity can be due to a Doppler shift correlated to the large drift velocity. When the drift velocity rises, the power spectra can be shifted to higher frequencies for the observer, which results in a higher frequency of the spectral break. This is consistent with Spicher et al. (2022), who showed that small-scale structures were convected with the $\mathbf{E} \times \mathbf{B}$ flow.

Particle precipitation is believed to be an important source of large-scale irregularities, and we found that for both rockets the strongest electron density fluctuations were in regions just outside electron precipitation, thus poleward of the cusp, or in regions with low detected electron precipitation.

Additionally, a lot of enhancements in the electron density fluctuations fall into gaps of particle precipitations. In regions of strong particle precipitation, a strong E-region conductivity can result in a channel between the E- and F-region, where electrons can move between the regions. It was found that in the case of a strongly conducting E-region, the electrons lead to a faster decay in electron density irregularities in the F-region (Kelley et al., 1982b; Basu & Coppi, 1988; Takahashi et al., 2022). Enhancements in conductivity below the rockets could thus explain the stronger electron density fluctuations in regions where no or very little precipitation was detected. Note, that while low precipitation seems to coincide with higher density irregularities, there are no enhanced density fluctuations in regions southward of the cusp.

Another explanation for increased electron density fluctuations poleward of the cusp could be that particle precipitation is structuring the plasma within the cusp. This leads to the convection of the structured plasma poleward out of the cusp into the polar cap. Due to the relative movement of the structured density patch through the background plasma in the polar cap, this movement can then be responsible for an increase in irregularities just beyond the cusp, for example, the GDI (Carlson et al., 2007; Moen et al., 2013). Spicher et al. (2014) have found the largest fluctuations in electron density irregularities for the low flyer poleward of the cusp. We can now also show that this is the case for the high flyer as well.

In addition to an analysis of the slopes in the power spectra, we looked at integrated power in order to understand in which frequency interval the most and least power exist. For frequencies between 10 Hz and 100 Hz, the relative fluctuations in integrated power are uniformly elevated throughout the flight for both flyers, however, they show a raise in a region with precipitation. While the low flyer shows a rise in power for all frequencies, the power for the high flyer rises mainly in the lower frequencies between 10 Hz and 30 Hz during the period when the rocket encounters particle precipitation. This could show that energetic particle precipitation is depositing energy into lower frequencies, where the free energy can be used to further structure the plasma.

While the power for the low frequencies is elevated more evenly, especially within regions of precipitation, there is a difference at higher frequencies. For the high flyer, there are few fluctuations throughout the flight, except a spike around 08:38 UT, which occurs immediately after the rocket leaves the region where electron precipitation is detected. This spike coincides with a large change in the electric field and thus a strong increase in the drift velocity corresponding to a flow channel. The strong rise in fluctuations at 08:38 UT occurs in all frequency intervals between 100 Hz and 1000 Hz.

The low flyer data show strong fluctuations in the integrated power between 08:36 UT and 08:41 UT. This mainly coincides with the strong rise in the electric field and the corresponding drift velocity, similar to the high flyer. While the high flyer data show a strong correlation between electric field and integrated power, however, the integrated power for the low flyer deviates slightly from the drift velocity measurements. While the region of elevated power starting around 08:39 UT correlates with a rise in drift velocity up to 6 km s^{-1}, the first region of elevated power starting around 08:37 UT shows nearly the same elevation in integrated power as the second elevation region does, but the drift velocity only raises to about 1/2 of the velocity of the second interval. Additionally, the low flyer exhibits another rise in integrated power before the other two intervals, starting around 08:36 UT, which falls together with the beginning of particle precipitation and a momentary change of drift velocity in the western direction. It seems that similar to the electron density fluctuations, peaks of the integrated power seem to fall into gaps in the precipitation. This becomes especially obvious for the double peak in power observed for the low flyer starting right after 08:38 UT which falls exactly into a double gap of precipitation at the same time. This again can be explained with a quenching of instabilities due to a highly conducting region below the rocket, similar to the explanation of the occurrence of electron density fluctuations.

Important to notice that, while the high flyer shows a rise in integrated power in all frequency intervals, the low flyer mainly exhibits a rise in power in the frequency range below 200 Hz. The integrated power of the high flyer agrees with the change in drift velocity while the integrated power of the low flyer only agrees to a certain degree, and could partially depend on the onset of precipitation similar to the lower frequencies. Thus, there is a possibility that plasma density irregularities are driven by different mechanisms at different altitudes.

For the purpose of this paper, we were interested in changes in the electron density with respect to precipitating particles and changes in the plasma drift. As described in Section 2, we estimate the error of both the electric and magnetic field instruments to be around 5%, which arises due to uncertainties mainly in the geometry and due to noise. While noise is affecting very small or fast signals, we only look at the overall trend in the drift velocity. Thus, we assume that noise has little effect on our results. The error in the geometry has been minimized by repeatedly deploying the booms before launch and measuring that the booms are in fact pointed in the direction they should. The distance between the booms was measured accurately to about a cm, while the direction was measured to an accuracy of about arc seconds of a degree. With a distance of 3 m per boom, these lead to errors that are smaller than 1%. Additionally, slight inaccuracies in the orientation of the probes towards the magnetic field may lead to uncertainties when calculating the electric field. As these errors are again small, we estimate the total error to not be bigger than 5% in total for both magnetic and electric field measurements. The key finding obtained from relating the spectra and the drift velocity is a rise in the frequency of the spectral break with increased velocity, which is unaffected by the errors mentioned above. For the errors in the electron density, we know the error in the sampling of the currents drawn to the m-NLP to be of the order of nA, which results in errors in density due to measurement uncertainties of less than a percent. Our main analysis tool in this work is the use of power spectra which are taken from 20,000 data points in 2-second intervals, and we used a Hamming window with 50% overlap to reduce the effect of taking a specific time interval for the spectrum. Additionally, smaller uncertainties in the spectra for frequency ranges at both ends of the power spectra are being considered. As we assume that all four probes in the mNLP system are measuring the same plasma at the same time, the high frequencies in the spectra may be affected for those higher than the frequency corresponding to the distance between the probes and the speed of the rocket. With a distance between the probes of 1 m, and assuming an average speed of the rocket of 3 km s^{-3}, spectral components below about 350 Hz should not suffer large errors from calculating the electron density with this inter-probe separation. On the other hand, the low-frequency side of the spectrum may be prone to errors due to the spin of the rocket and influenced by the detrending process. We have removed the spin frequency of around 0.6 Hz and harmonics with band-pass filters. As the detrending process was done with a Savitzky-Golay filter, the frequency may vary but should not reach more than 2 Hz. However, as we only use values between 3 Hz and 300 Hz for the analysis of the slope, these should have a minor impact. The last error we shall consider is the uncertainty that comes from $\beta = 0.5$. This error has been estimated to be 25–40% (Hoang et al., 2018), while simulations showed deviations of up to an order of magnitude (Guthrie et al., 2021). We are mainly interested in the relative fluctuations of the density and not in absolute densities, thus systematic uncertainties that lead to an overall over- or underestimation of the density are not crucial for the work in this paper (Marholm, 2020). Furthermore, we try to counter uncertainties in the electron density PSD by using overlapping windows for the Fourier transform of 50% and takes a large sampling size for each spectrum of 20,000 sampling points. If there are uncertainties in the electron density, it may shift the spectrum for certain frequencies. As we do not try to make an analysis by quantifying the slopes in detail but rather analyzing the trend of the slope and integrated power with respect to precipitating electrons and drift velocity, we assume the uncertainties due to the measurement of the electron density do not alter any of the main points discussed in this paper.

5 Conclusion

In this work, we show that particle precipitation in the cusp ionosphere is of importance for the formation of large-scale irregularities. Electron density fluctuations and the corresponding power spectra obtained from both rockets in the TRICE-2 campaign were analyzed. The largest fluctuations in the electron density were found in regions immediately after the rockets left

the region of precipitation, thus poleward of the cusp. Strong electron density fluctuations fall into gaps of detected precipitation. This could be due to a higher conductance below the rockets resulting from energetic particle precipitation which leads to a faster decay of irregularities in the F-region. Another reason may be that the rocket encounters structured plasma that travels poleward out of the cusp into the polar cap, where the relative movement of the high-density plasma gives rise to instabilities.

Furthermore, we found that the power spectra in the cusp region were best described by a double slope. We found frequencies for the break frequency of the slope that may coincide with the oxygen gyrofrequencies at these altitudes. Shifts of the break frequency to higher frequencies are correlating with a rise in the $\mathbf{E} \times \mathbf{B}$-drift velocity. This correlation could be due to a Doppler shift, moving the power spectrum up to higher frequencies. The break frequencies have been analyzed for decades and have been found at several different scales, thus making a physical explanation difficult. In addition to the slopes of the power spectra, we also analyzed the relative integrated power in different frequency intervals. For low frequencies, the whole flight interval is elevated with larger fluctuations throughout the flight for both rockets. This elevation is pronounced specially for regions of particle precipitation, suggesting that precipitation deposits energy into larger scales. For higher frequencies, the integrated power for the high flyer is quiet for most of the flight, except for a sharp peak right after the rocket left the cusp, which correlates to a large peak in drift velocity. The high-frequency integrated power for the low flyer is enhanced for a longer time interval. While it mostly overlaps with a rise in drift velocity, it is not proportional as seen for the high flyer, and the integrated power starts rising with an onset of precipitation, before the drift velocity changes. This could indicate that different mechanisms are dominant at different altitudes. For further studies on how particle precipitation influences the formation of irregularities, it would be beneficial to examine these results statistically for longer periods of time and a larger range of altitudes.

Acknowledgements. The m-NLP experiment and the University of Oslo (UiO) participation in the Grand Challenge Initiative Cusp rocket campaign were funded through the Research Council of Norway (RCN) grant 275653. The authors thank Espen Trondsen, David Michael Bang-Hauge, and the Mechanical Workshop at UiO for the m-NLP instrument. This work was partially conducted within the 4DSpace research initiative at UiO. The study was supported in part by the European Research Council (ERC) under the European Union's Horizon 2020 research and innovation program (grant agreement No 866357). Data from the TRICE-2 missions can be found at: https://phi.physics.uiowa.edu/science/tau/data0/rocket/SCIENCE/TRICEII_Mission/. The authors thank the Andøya Space Center for launch operations, KHO/UNIS/UiO for support with ground-based observations, and all the personnel involved in the mission. S.M. acknowledges Øyvind Jensen and the Institute for Energy Technology (IFE) for permission to see this work through to the end while at IFE. A.S. acknowledges funding from RCN grant 326039. The editor thanks P. Thayyil Jayachandran and Weijia Zhan for their assistance in evaluating this paper.

References

Basu B, Coppi B. 1988. Fluctuations associated with sheared velocity regions near auroral arcs. *Geophys Res Lett* **15(5)**: 417–420. https://doi.org/10.1029/gl015i005p00417.

Basu S, Basu S, MacKenzie E, Coley W, Sharber J, Hoegy W. 1990. Plasma structuring by the gradient drift instability at high latitudes and comparison with velocity shear driven processes. *J Geophys Res Space Phys* **95(A6)**: 7799–7818. https://doi.org/10.1029/JA095iA06p07799.

Bekkeng T, Jacobsen K, Bekkeng J, Pedersen A, Lindem T, Lebreton J, Moen J. 2010. Design of a multi-needle Langmuir probe system. *Meas Sci Technol* **21(8)**: 085903. https://doi.org/10.1088/0957-0233/21/8/085903.

Carlson HC. 2012. Sharpening our thinking about polar cap ionospheric patch morphology, research, and mitigation techniques. *Radio Sci* **47(4)**: 1–16. https://doi.org/10.1029/2011RS004946.

Carlson HC, Pedersen T, Basu S, Keskinen M, Moen J. 2007. Case for a new process, not mechanism, for cusp irregularity production. *J Geophys Res Space Phys* **112(A11)**. https://doi.org/10.1029/2007JA012384.

Crowley G, Schoendorf J, Roble RG, Marcos FA. 1996. Cellular structures in the high-latitude thermosphere. *J Geophys Res Space Phys* **101(A1)**: 211–223. https://doi.org/10.1029/95JA02584.

Di Mare F, Spicher A, Clausen LBN, Miloch WJ, Moen JI. 2021. Turbulence and intermittency in the Winter cusp ionosphere studied with the ICI sounding rockets. *J Geophys Res Space Phys* **126(8)**: e2021JA029150. https://doi.org/10.1029/2021JA029150.

Frisch U, Kolmogorov AN. 1995. *Turbulence: the legacy of AN Kolmogorov*. Cambridge University Press.

Guthrie J, Marchand R, Marholm S. 2021. Inference of plasma parameters from fixed-bias multi-needle Langmuir probes (m-NLP). *Meas Sci Technol* **32(9)**:095906. https://doi.org/10.1088/1361-6501/abf804.

Hoang H, Røed K, Bekkeng T, Moen J, Spicher A, Clausen L, Miloch W, Trondsen E, Pedersen A. 2018. A study of data analysis techniques for the multi-needle Langmuir probe. *Meas Sci Technol* **29(6)**: 065906.

Hysell D, Kelley M, Swartz W, Pfaff R, Swenson C. 1994. Steepened structures in equatorial spread F: 1. *New observations. J Geophys Res Space Phys* **99(A5)**: 8827–8840. https://doi.org/10.1029/93JA02961.

Ivarsen MF, Jin Y, Spicher A, Clausen LB. 2019. Direct evidence for the dissipation of small-scale ionospheric plasma structures by a conductive E region. *J Geophys Res Space Phys* **124(4)**: 2935–2942. https://doi.org/10.1029/2019JA026500.

Ivarsen MF, St-Maurice J-P, Jin Y, Park J, Miloch W, Spicher A, Kwak Y-S, Clausen LB. 2021. Steepening plasma density spectra in the ionosphere: The crucial role played by a strong E-region. *J Geophys Res Space Phys* **126(8)**: e2021JA029401. https://doi.org/10.1029/2021JA029401.

Jacobsen K, Pedersen A, Moen J, Bekkeng T. 2010. A new Langmuir probe concept for rapid sampling of space plasma electron density. *Meas Sci Technol* **21(8)**: 085902. https://doi.org/10.1088/0957-0233/21/8/085902.

Jahn J-M, LaBelle J. 1998. Rocket measurements of high-altitude spread F irregularities at the magnetic dip equator. *J Geophys Res Space Phys* **103(A10)**: 23427–23441. https://doi.org/10.1029/97JA02636.

Jin Y, Moen JI, Miloch WJ. 2014. GPS scintillation effects associated with polar cap patches and substorm auroral activity: Direct comparison. *J Space Weather Space Clim* **4**: A23. https://doi.org/10.1051/swsc/2014019.

Jin Y, Moen JI, Miloch WJ. 2015. On the collocation of the cusp aurora and the GPS phase scintillation: A statistical study. *J Geophys Res Space Phys* **120(10)**: 9176–9191. https://doi.org/10.1002/2015JA021449.

Kelley M, Pfaff R, Baker K, Ulwick J, Livingston R, Rino C, Tsunoda R. 1982a. Simultaneous rocket probe and radar measurements of equatorial spread F – Transitional and short wavelength results. *J Geophys Res Space Phys* **87(A3)**: 1575–1588. https://doi.org/10.1029/JA087iA03p01575.

Kelley MC, Vickrey JF, Carlson C, Torbert R. 1982b. On the origin and spatial extent of high-latitude F region irregularities. *J Geophys Res Space Phys* **87(A6)**: 4469–4475. https://doi.org/10.1029/JA087iA06p04469.

Keskinen MJ, Ossakow S. 1983. Theories of high-latitude ionospheric irregularities: A review. *Radio Sci* **18(06)**: 1077–1091. https://doi.org/10.1029/rs018i006p01077.

Kintner PM, Ledvina BM, De Paula E. 2007. GPS and ionospheric scintillations. *Space Weather* **5(9)**. https://doi.org/10.1029/2006SW000260.

Kintner PM, Seyler CE. 1985. The status of observations and theory of high latitude ionospheric and magnetospheric plasma turbulence. *Space Sci Rev* **41(1)**: 91–129. https://doi.org/10.1007/bf00241347.

LaBelle J, Kelley M, Seyler C. 1986. An analysis of the role of drift waves in equatorial spread F. *J Geophys Res Space Phys* **91(A5)**: 5513–5525. https://doi.org/10.1029/JA091iA05p05513.

Marholm S. 2020. *The unstructured particle-in-cell method with applications for objects in ionospheric plasmas*. Available at http://urn.nb.no/URN:NBN:no-76155.

Marholm S, Marchand R. 2020. Finite-length effects on cylindrical Langmuir probes. *Phys Rev Res* **2(2)**: 023016. https://doi.org/10.1103/PhysRevResearch.2.023016.

Moen J, Oksavik K, Abe T, Lester M, Saito Y, Bekkeng T, Jacobsen K. 2012. First in-situ measurements of HF radar echoing targets. *Geophys Res Lett* **39(7)**. https://doi.org/10.1029/2012GL051407.

Moen J, Oksavik K, Alfonsi L, Daabakk Y, Romano V, Spogli L. 2013. Space weather challenges of the polar cap ionosphere. *J Space Weather Space Clim* **3**: A02. https://doi.org/10.1051/swsc/2013025.

Moen J, Spicher A, Rowland D, Kletzing C, LaBelle J. 2018. *Grand Challenge Initiative – Cusp: Rockets to explore solar wind-driven dynamics of the top side polar atmosphere*. Available at https:// sios-svalbard.org/sites/sios-svalbard.org/files/common/SESS_2018_09_GCI_Cusp.pdf.

Moen J, Walker I, Kersley L, Milan S. 2002. On the generation of cusp HF backscatter irregularities. *J Geophys Res Space Phys* **107(A4)**: SIA 3-1–3-5. https://doi.org/10.1029/2001JA000111.

Moser C, LaBelle J, Roglans R, Bonnell J, Cairns I, Feltman C, Kletzing C, Bounds S, Sawyer R, Fuselier S. 2021. Modulated upper-hybrid waves coincident with lower-hybrid waves in the cusp. *J Geophys Res Space Phys* **126(9)**: e2021JA029590. https://doi.org/10.1029/2021JA029590.

Oksavik K, Moen J, Lester M, Bekkeng TA, Bekkeng JK. 2012. In situ measurements of plasma irregularity growth in the cusp ionosphere. *J Geophys Res Space Phys* **117(A11)**: n/a–n/a. https://doi.org/10.1029/2012ja017835.

Spicher A, LaBelle J, Bonnell JW, Roglans R, Moser C, et al. 2022. Interferometric study of ionospheric plasma irregularities in regions of phase scintillations and HF backscatter. *Geophys Res Lett* **49(12)**: e2021GL097013. https://doi.org/10.1029/2021GL097013.

Spicher A, Miloch W, Moen J. 2014. Direct evidence of double-slope power spectra in the high-latitude ionospheric plasma. *Geophys Res Lett* **41(5)**: 1406–1412. https://doi.org/10.1002/2014GL059214.

Takahashi T, Spicher A, Di Mare F, Rowland DE, Pfaff RF, Collier MR, Clausen LBN, Moen JI. 2022. Suppression of ionospheric irregularity due to auroral particle impact. *J Geophys Res Space Phys* **127(1)**: e2020JA028725. https://doi.org/10.1029/2020JA028725.

Tsunoda RT. 1988. High-latitude F region irregularities: A review and synthesis. *Rev Geophys* **26(4)**: 719–760. https://doi.org/10.1029/RG026i004p00719.

Villain J, Hanuise C, Beghin C. 1986. ARCAD3-SAFARI coordinated study of auroral and polar F-region ionospheric irregularities. *Ann Geophys* **4**: 61–68.

Yeh KC, Liu C-H. 1982. Radio wave scintillations in the ionosphere. *Proc IEEE* **70(4)**: 324–360. https://doi.org/10.1109/PROC.1982.12313.

Appendix

Normalization factors

Table A1 in Appendix shows the normalization factors of order 10^{15} for the integrated power plots (Figs. 4g–4j). As the power was integrated with respect to different frequency intervals of different sizes (10 and 100 Hz), we decided to make the four plots more compatible. This was achieved by first dividing the integrated power by the length of the frequency interval (namely by a factor 10 for the frequencies between 10 Hz and 100 Hz (Figs. 4g and 4h) and a factor 100 for the frequencies between 100 Hz and 1000 Hz (Figs. 4i and 4j). This provided a result in power/Hz. As a power spectrum is naturally cascading to lower values for higher frequencies, we were interested in a change of integrated power instead of absolute power. Due to the cascading and integrated power for 10 Hz would naturally always be higher than for 20 Hz and so forth. In order to look at the relative fluctuations in integrated power we divided each graph (corresponding to the integrated power/Hz for each frequency interval) by the median of a "quiet area" of the same graph.

The 50 Hz graph of the high flyer (green graph in Figs. 4g) shall be taken as an example. In order to compare the intervals of 10 Hz length to the intervals of 100 Hz length, we first divide this graph by 10. The integral of a power spectrum between 50 Hz and 60 Hz would naturally be much smaller than the integral between 20 Hz and 30 Hz but much bigger than an interval between 70 Hz and 80 Hz. In order to compare these intervals in a better way with each other, we divide every graph by the median of itself in a quiet interval (an interval without many fluctuations in integrated power). This way, all graphs should be normalized to a similar "base line" (this means that the quiet areas of the integrated power all have roughly the same value. If no normalization was done, all graphs would have different values for the quiet areas). All graphs were normalized with a median taken from the same time interval, which corresponds to a minute of data 300–360 s into the flight. This is the interval between 08:31:00 and 08:32:00 UT for the high flyer and between 08:33:00 and 08:34:00 UT for the low flyer. Each graph was then divided by its corresponding normalization factor, all factors can be found in Table A1.

Table A1. Normalization factors for integrated power as seen in Figure 4g, 4h, 4i, and 4j. The normalization factors consist of the median of each frequency interval and the interval length, the factors are of order 10^{15}.

	High flyer	Low flyer		High flyer	Low flyer
10–19 Hz	1.07	1.07	100–199 Hz	7.42	7.50
20–29 Hz	0.49	0.38	200–299 Hz	6.50	6.43
30–39 Hz	0.36	0.24	300–399 Hz	6.48	6.29
40–49 Hz	0.22	0.25	400–499 Hz	6.50	6.18
50–59 Hz	0.22	0.14	500–599 Hz	6.50	6.41
60–69 Hz	0.17	0.14	600–699 Hz	6.24	6.44
70–79 Hz	0.13	0.11	700–799 Hz	6.26	6.53
80–89 Hz	0.11	0.11	800–899 Hz	6.00	6.13
90–99 Hz	0.11	0.09	900–999 Hz	5.69	5.71

Cite this article as: Buschmann LM, Bonnell JW, Bounds S, Clausen LBN, Kletzing C, et al. 2023. The role of particle precipitation on plasma structuring at different altitudes by in-situ measurements. *J. Space Weather Space Clim.* **13**, 13. https://doi.org/10.1051/swsc/2023012.

Paper II

Statistical Studies of Plasma Structuring in the Auroral Ionosphere by the Swarm Satellites

Lisa M. Buschmann, Lasse B.N. Clausen, Andres Spicher, Magnus F. Ivarsen, Wojciech J. Miloch

Published in Journal of Geophysical Research: Space Physics
https://doi.org/10.1029/2023JA032097

II

JGR Space Physics

RESEARCH ARTICLE
10.1029/2023JA032097

Statistical Studies of Plasma Structuring in the Auroral Ionosphere by the Swarm Satellites

L. M. Buschmann[1], L. B. N. Clausen[1], A. Spicher[2], M. F. Ivarsen[1,3], and W. J. Miloch[1]

[1]Department of Physics, University of Oslo, Oslo, Norway, [2]Institute for Physics and Technology, UiT—The Arctic University of Norway, Tromsø, Norway, [3]Department of Physics and Engineering Physics, University of Saskatchewan, Saskatoon, SK, Canada

Key Points:

- Analysis of the power spectral density suggests no connection of double slope occurrence rate and irregularity power within certain scales
- ROTI data are similar to the integrated power from the PSD but show larger enhancements within the cusp and nightside auroral oval
- The strongest B_y fluctuations are found within the cusp. These enhancement may indicate an increase in Poynting flux on km-scales

Correspondence to:
L. M. Buschmann,
lisa.buschmann@fys.uio.no

Citation:
Buschmann, L. M., Clausen, L. B. N., Spicher, A., Ivarsen, M. F., & Miloch, W. J. (2024). Statistical studies of plasma structuring in the auroral ionosphere by the Swarm satellites. *Journal of Geophysical Research: Space Physics*, *129*, e2023JA032097. https://doi.org/10.1029/2023JA032097

Received 18 SEP 2023
Accepted 31 JAN 2024

Abstract This study uses over 2 years of 16 Hz density measurements, 50 Hz magnetic field data and ROTI data from the Swarm mission to perform long term statistics of plasma structuring in the polar ionosphere. The timeframe covers more than 2 years near the 24th solar cycle peak. We additionally use 3 years of data obtained from a timeframe close to solar minimum for discussion. We present power spectral densities (PSD) of electron density irregularities and magnetic field for 1-min intervals. These PSD have been characterized by the probability of a slope steepening, and by integrating the power deposited within frequency intervals corresponding to kilometer scales. For the electron density, we observe seasonal dependencies for both the integrated power and slope characteristics. While the dual slope probability, especially within the polar cap, varies with solar EUV-radiation, the integrated power is strongest around the equinoxes. Additionally, while we found similar results for the slope probability for both hemispheres, the integrated power exhibits strong hemispheric asymmetries with stronger enhancements within local summer in the southern hemisphere. The ROTI data shows a similar seasonal variability as the density PSD integrated power, in both seasonal dependency and interhemispheric variability. However, for the ROTI data the strongest fluctuations were found within the nightside auroral oval and the cusp. For the PSD of the magnetic field data, we obtain the strongest enhancements within the cusp for all seasons and all hemispheres. The fluctuations may indicate an increase in Alfvénic energy associated with a downward Poynting flux.

1. Introduction

Auroral particle precipitation is believed to be a major source of large scale irregularities in the plasma of the cusp and night-side auroral oval (M. C. Kelley et al., 1982; Moen et al., 2013, 2002). Precipitating electrons can protrude into the ionosphere in these regions and function as a source of free energy. Large-scale irregularities that evolve in the cusp can follow the polar convection pattern toward the night side through the polar cap (PC) and constitute a crucial factor for the development of structures in the polar cap. The most noteworthy among these structures are polar cap patches (PCP).

PCP can be defined as areas with scales between 100 and 1,000 km which have at least twice the density of the background plasma. These patches are generated when high density solar-EUV produced plasma on the dayside ionosphere enters the polar cap (Carlson, 2012; Crowley et al., 1996 and references therein). When these structures travel through the PC, they can be broken down to smaller scales, in a so-called turbulent cascade. Several sources have been proposed to explain the formation of these irregularities, including the gradient drift instability (GDI) and the Kelvin-Helmholtz instability (KHI) (S. Basu et al., 1990; Carlson, 2012; M. J. Keskinen & Ossakow, 1983; Kintner & Seyler, 1985; Tsunoda, 1988). The GDI affects primarily the trailing edge of PCP as the background plasma flow is parallel to the gradient of the electron density (Tsunoda, 1988). On the other hand, the KHI is driven by velocity shears in the plasma. Lately, a two-step process has been proposed in which patches are first structured by shear driven instabilities (e.g., the KHI) in the first minutes after the patch enters the PC. In a second step the GDI is then taking over and is further structuring the patch into decameter scale irregularities (Carlson, 2012; Carlson et al., 2007; Hosokawa et al., 2013; Moen et al., 2012, 2013).

Several studies have been conducted with focus on PCP, showing a seasonal dependency of the occurrence of irregularities. Generally, a higher occurrence of patches has been found in the northern hemisphere (NH) during winter season (Chartier et al., 2018; Jin & Xiong, 2020). Overall, polar cap patches are more subdued in summer due to the background plasma from elevated EUV ionization (Spicher et al., 2017). As the majority of these

studies have been conducted in the NH, less studies involve the southern hemisphere with contradictory results (Chartier et al., 2018, 2019; David et al., 2019; Jin & Xiong, 2020; Kagawa et al., 2021; Spicher et al., 2017).

When these larger scale structures are broken down to smaller scales, they can cause problems for global navigation satellite systems (GNSS). Scintillations, which are rapid temporal fluctuations in phase and amplitude in trans-ionospheric GNSS signals, can be detrimental for navigation accuracy or signal acquisition (S. Basu et al., 1990; Kintner et al., 2007; Tsunoda, 1988; Yeh & Liu, 1982). Below the Fresnel's scale, which is of the order of few hundreds of meters for GNSS signals, the scintillations of phase and amplitude are of stochastic nature and due to diffractive effects (Kintner et al., 2007). Above the Fresnel scale, refraction effects, which are of deterministic nature, become important and can result in enhanced values of phase scintillation index σ_Φ (McCaffrey & Jayachandran, 2019). They can often be removed by applying ionospheric free-linear combination (IFLC), where a combination of two carrier phases of two signals with different frequencies are used to remove refractive effects on the signals (Carrano et al., 2013; Zheng et al., 2022). Enhancements in σ_Φ indices have also been shown to be adequately represented by ROTI on larger scales above the Fresnel scale (Rino et al., 2019), and can additionally be dependent on the plasma flow and rate of change of TEC (ROT) at high latitudes (Y. Wang et al., 2018, 2022). Recent literature has proposed that only fluctuations of the former nature, namely of stochastic nature, are deemed scintillations (De Franceschi et al., 2019; Ghobadi et al., 2020; McCaffrey & Jayachandran, 2019; Spogli et al., 2021).

It has been shown that high levels of σ_Φ can be related to particle precipitation in the cusp aurora (Clausen et al., 2016; Jin et al., 2015, 2017) and that filamentary field-aligned currents (FAC), are co-located with strong enhancements in σ_Φ in the cusp (Fæhn Follestad et al., 2020). As GNSS have become increasingly important, research on plasma irregularities in the ionosphere and associated effects has intensified in recent years (Jin et al., 2014, 2017; Kintner et al., 2007; Moen et al., 2012, 2013; Oksavik et al., 2012; van der Meeren et al., 2015).

One method to investigate instabilities and turbulence in plasmas comprises the use of spectral analysis (Frisch & Kolmogorov, 1995). Ionospheric plasma instabilities have been suggested to follow power laws with different mechanisms resulting in different slopes when fitted in a plot with double logarithmic axes (Kintner & Seyler, 1985; Tsunoda, 1988). Previous observations suggest an initial slope, or spectral index, between 1 and 2.2, depending on the altitude and region (B. Basu & Coppi, 1988; S. Basu et al., 1990; M. Kelley et al., 1982; M. C. Kelley et al., 1982; Kintner & Seyler, 1985; LaBelle et al., 1986; Pfaff et al., 1997; Prakash et al., 1971). In situ measurements of the ionosphere reveal that plasma fluctuations exhibit a steeper slope at higher frequencies. This slope steepening was first documented for the low-latitude ionosphere using sounding rockets and satellites (M. C. Kelley et al., 1982) and is commonly observed in this region (Hysell et al., 1994; Jahn & LaBelle, 1998; LaBelle et al., 1986). The high-latitude F-region has also shown this steepening (S. Basu et al., 1990; Buschmann et al., 2023; Di Mare et al., 2021; Ivarsen et al., 2019, 2021; Spicher et al., 2014; Villain et al., 1986). The spectral index in the high-latitude ionosphere has been shown to be approximately $-5/3$ at low frequencies and around -3 to -5 at high frequencies. Spectral breakpoints, or the frequency at which the spectral steepening occurs, have been observed on a variety of scales ranging up to 100 Hz (Buschmann et al., 2023; Di Mare et al., 2021; Ivarsen et al., 2019, 2021; Spicher et al., 2014). Spectral break points at different scale sizes may indicate different mechanisms happening at different scales. Spectral breaks that have been observed by sounding rockets have often been linked to the oxygen gyrofrequency at the corresponding altitudes, a transition between the inertial regime to a collisional regime (M. Keskinen & Huba, 1990), the ion-inertial range (Di Mare et al., 2021; Ivarsen et al., 2019), or where diffusion, drift waves, or wave steepening dominate (Hysell et al., 1994; LaBelle et al., 1986). Another approach, in contrast to the dissipation of energy, links the spectral break to an injection of energy within these scales (Kintner & Seyler, 1985). The frequency at which the spectral break occurs has been studied for decades, but is still not fully understood (Tsunoda, 1988).

Recently, Ivarsen et al. (2021) used an automated spectral breakpoint algorithm to characterize power spectra from several years of electron density data showing a spectral index of -1.6 on average at larger scales throughout the F-region ionosphere. Additionally, they linked the occurrence of spectral steepening in the polar ionosphere to the level of solar extreme ultraviolet (EUV) radiation and thus the solar zenith angle (SZA), presenting evidence for the dependency of plasma irregularities in the polar cap on the SZA.

Lately it has been found that the occurrence of double slopes in the electron density was most prominent in the cusp and immediately poleward of the cusp, while the strongest electron density fluctuations were found just poleward of the cusp (Buschmann et al., 2023; Spicher et al., 2022). Additionally, an analysis of the integrated

spectral power in the power spectral density (PSD) showed an increased energy within lower frequencies in presence of particle precipitation, while power in higher frequencies is elevated poleward of the precipitation, suggesting an energy input from electron precipitation into the cusp in frequencies corresponding to kilometer scales, while the energy is cascading to smaller scales in the polar cap.

This study is conducted by using data from the Swarm satellites. An advantage of the Swarm mission, or polar orbiting satellites in general, is that there is coverage over all latitudes. This gives the opportunity to conduct statistical research for large time periods and different latitudes.

Section 3 of this study gives the results for high solar activity. We have analyzed data between 01 October 2014 and 31 December 2016, and between 01 January 2020 and 31 December 2022, to distinguish between differences in the processes for solar maximum and minimum, respectively. However, due to a larger amount of data gaps within the time frame 2020 to 2022 we decided to mainly focus on the years 2014–2016, a period that directly follows the 24th solar cycle peak. For completeness, the results for low solar activity will be given in Appendix A.

2. Methodology and Instrumentation

This study uses data from the Swarm mission, a satellite constellation consisting of three identical satellites (A, B, and C) (Friis-Christensen et al., 2006, 2008). We make use of data from satellites A and C, which are flying side-by-side (1.4° separation in longitude at the equator) at an altitude of around 460 km. The employed data includes the 16 Hz face-plate electron density (N_e), the 50 Hz magnetic field data (B), the field-aligned current (FAC) data, and the Rate of Change of TEC index (ROTI) from the Ionospheric Plasma Irregularities (IPIR) data set (Jin et al., 2022). The data set used covers a period of more than 5 years, from 01.10.2014 to 31.12.2016, and from 01.01.2020 to 31.12.2022, to distinguish between differences in the processes for solar maximum and minimum, respectively. For our analysis, we only use time intervals where all data sets are available, thus ensuring that N_e, B, FAC, and IPIR data are present for all intervals. We thus cover the majority of the chosen time frame, however, some larger data gaps can be found throughout the data. Moreover, in the statistical analysis we additionally only use data poleward of ±50° magnetic latitude. For conversion from geographic coordinates to magnetic latitude (MLat) and magnetic local time (MLT) we use magnetic apex coordinates (AD, 1995; Emmert et al., 2010). Additionally, we divide the data into 4 seasonal intervals, comprising 4 time spans between 91 and 92 days around the equinoxes and solstices. This leads to the following seasonal intervals: spring, utilizing data between 4 February and 5 May, summer between 6 May and 5 August, autumn between 6 August and 5 November, and winter between 6 November and 3 February.

For the 16 Hz N_e and 50 Hz B data, we conduct a spectral analysis using the Logarithmic frequency axis Power Spectral Density (LPSD) method as described in Tröbs and Heinzel (2006). This procedure utilizes the Welch power spectral method. The Welch power spectra is a method of estimating PSD by averaging modified periodograms (Welch, 1967). However, while the original Welch method is utilizing the same frequency resolution for every Fourier frequency, the LPSD method is adjusting the frequency resolution instead (Tröbs & Heinzel, 2006). As we are mainly interested in fluctuations of B and N_e rather than absolute values, we apply a first-order linear trend to both quantities for each 1-min interval prior to the spectral analysis, in order to get information about the small-scale fluctuations only and eliminate influence of seasonal dependencies in N_e. We then perform the spectral analysis mentioned above using a Hanning window for a 1-min interval. The resulting power spectrum can then be described by either one or two linear slopes in a plot with double logarithmic axes, with

$$\mathrm{PSD}(f) \propto f^{-p} \tag{1}$$

where p is the slope of the fit and thus $p > 0$. For a power spectrum that is better described with two fits, the equation changes to

$$\mathrm{PSD}(f) \propto \begin{cases} f^{-p_1}, & for\ f \leq f_{sb} \\ f^{-p_2}, & for\ f \geq f_{sb} \end{cases} \tag{2}$$

where f_{sb} is the break point frequency where the slopes p_1 and p_2 of the PSD change, with $p_2 > p_1$. We plot the power spectra for each interval using a logarithmic scale and then use an automated slope detection method, which fits one or two slopes to the spectrum using a piece-wise linear Hermite function as a least-square fit as described in

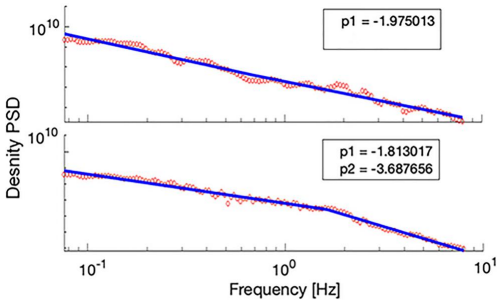

Figure 1. Power-spectral density plot of the electron density N_e. The top plot shows a PSD that is best approximated by a single linear trend (single slope, SS), while the bottom plot shows a PSD that is best approximated by a combination of two linear trends (double slope, DS).

D'Errico (2017). The method is minimizing the rms error in order to localize the spectral break frequency and is further described in Ivarsen et al. (2019, 2021). The threshold which is used to determine if two fitted slopes are considered a double slope is $p_2 - p_1 \geq 0.8$. This threshold has been used in previous works (Buschmann et al., 2023; Ivarsen et al., 2019) and has been determined by repeated testing. The range in which a break point could be found is set to frequencies between 0.19 and 7 Hz, which corresponds to spatial scales between 1.1 and 40 km, respectively. As N_e is measured at a cadence of 16 Hz, we are not able to obtain any information above 8 Hz within the PSD, which corresponds to the Nyquist frequency. Two examples of density PSD plots with either a single or double slope are shown in Figure 1.

In addition to the slopes and break-point, we analyze the integrated power within certain frequency intervals in order to compare the power within different spatial scales in different regions. For the analysis of N_e we choose a 1 Hz frequency interval between 1 and 2 Hz, which corresponds to spatial scales between 3.8 and 7.6 km. Additional intervals between 0.1 and 0.6 Hz and 6 and 7 Hz are analyzed for comparison. We also utilize the 10 s ROTI data obtained from the IPIR data set. ROTI is the standard deviation of Total Electron Content (TEC) for a given running window, in this case 10 s. The ROTI is calculated from the Vertical TEC (VTEC) values, the exact calculation and methodology for the ROTI derivation is documented in Jin et al. (2022).

We have added the ROTI data in addition to the integrated power analysis in order to get an additional source of data for comparison. The integrated power is calculated from the in situ measurements of the 16 Hz N_e PSD and thus provides a measure of the energy deposited within different frequency ranges. While this study mainly focuses on frequencies between 1 and 2 Hz, we also analyze the energy deposited within 0.1–0.6 Hz and 6–7 Hz for comparison. The integrated power thus provides a measure of the amplitude of fluctuations of certain scales. The ROTI data, on the other hand, covers a large ionospheric area as it is calculated from the GNSS receivers on board of the satellites and is thus not a direct measurement within the plasma, as it calculates the TEC based on the signals obtained from GNSS satellites. Thus, the ROTI data provides a measure of fluctuations within the plasma density and gives a measure of the amount of structuring.

The main FAC data used within this study stems from the B_y component of the 50 Hz B data, as described further in the next paragraph. In addition, for the first run of analyses we use the 1 Hz FAC product. This product uses simultaneous measurements of the constellation of both Swarm A and C. The calculation is based on the vertical current density using Ampere's law, the FAC is then obtained from the magnetic field residuals. A more in-depth calculation can be obtained from Ritter et al. (2013).

The 50 Hz B data analysis uses a similar technique as the analysis of N_e, only varying in the frequency interval used for detecting break points. As the sampling frequency for B is much higher than for the N_e sampling frequency, we set the interval to frequencies between 0.5 and 23 Hz, corresponding to spatial scales between 0.33 and 15.2 km. The interval chosen for the integrated power analysis is once more a 1 Hz interval, again between 1 and 2 Hz, corresponding to spatial scales between 3.8 and 7.6 km. We decided to use the B_y-component, or geographic east component in NEC-coordinates, as a proxy for the FAC, as it is not feasible to conduct a spectral analysis on the 1 Hz FAC data in this case, while the B data is provided at 50 Hz resolution. The magnetic field may be converted to the FAC density j_z according to Fæhn Follestad et al. (2020) and Ritter et al. (2013)

$$j_z = \frac{1}{\mu_0 \nu_x} \frac{\Delta B_y}{\Delta t} \tag{3}$$

where ν_x is the velocity perpendicular to the FAC and ΔB_y is the detrended magnetic component parallel to the current sheet (Fæhn Follestad et al., 2020; H. Wang et al., 2005). We then use the fluctuations is B_y as a mean of analyzing the FAC.

Figure 2 shows a sample pass of Swarm A over the northern hemisphere on the 2nd November 2014 between 13:09 and 13:41 UT. The trajectory of the satellite can be seen in the upper right corner of Figure 2. The figure shows N_e (panel a), FAC (panel b), B_y (panel c), slopes obtained from the N_e PSD and the corresponding spectral

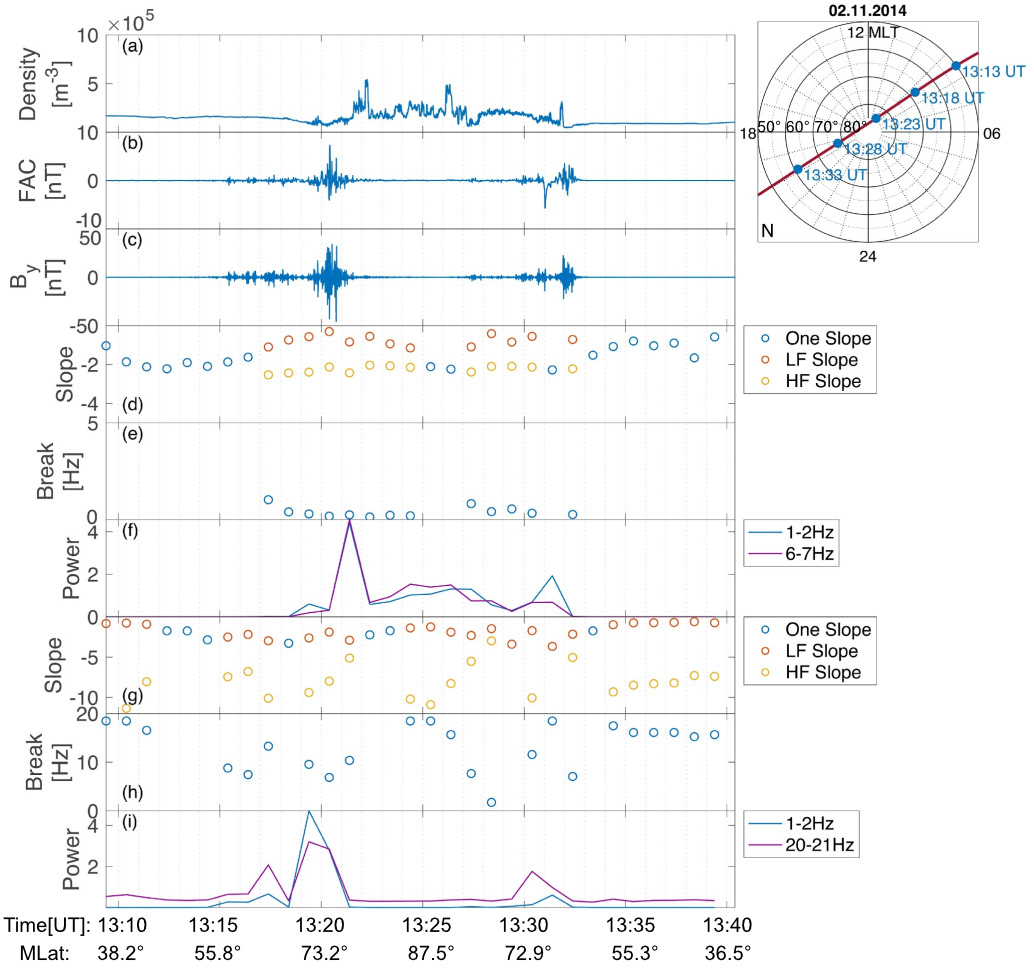

Figure 2. One pass of Swarm A over the polar region in the northern hemisphere on 02.11.2014 between 13:09 UT and 13:41 UT. The panels show the following from top to bottom, with frequencies giving the cadence of the corresponding signal: (a): the absolute 16 Hz electron density N_e, (b): the absolute 1 Hz FAC, (c): the detrended 50 Hz B_y-component, (d): the slopes obtained from the N_e PSD, and (e): the corresponding spectral break frequencies, (f): the integrated power from the N_e PSD between 1–2 and 6–7 Hz, (g): the slopes obtained from the B_y PSD, and (h): the corresponding spectral break frequencies, and (i): the integrated power from the B_y PSD between 4–5 and 20–21 Hz. The plot in the top right corner shows the trajectory in MLat/MLT coordinates. The magenta line is the trajectory, the blue dots correspond to the times given in the plot in UT.

break frequency (panels d and e) and the integrated power within 1–2 Hz and 6–7 Hz from the same PSD. Panels g–i show the slopes, spectral break frequency if applicable and the integrated power between 1–2 Hz and 20–21 Hz for 1-min intervals from the B_y PSD, respectively.

The satellite encounters very little density fluctuations in both mid-latitude (MidLat) regions. This is linked with a single slope and little integrated power in the corresponding power spectra. One way to distinguish the auroral oval (AO) from the PC and MidLat regions is by looking at the FAC graph (panel b) and the B_y graph (panel c). When the satellite passes the AO, north of 67° MLat, the N_e power spectra (panels d and e) start being best

described by a double slope instead of a single slope and the integrated power (panel f) rises. Within the PC, recognizable by the region in between the strong fluctuations in the FAC and B_y, N_e shows several increases, for example, at 13:26 UT, which can be associated with polar cap patches. The strongest N_e fluctuations occur between 13:21 UT and 13:28 UT. After that, the N_e fluctuations diminish slightly. While the integrated power from the N_e PSD (panel f) clearly exhibits peaks within the AO during strong FAC fluctuations, a third peak can be seen within the PC. This third peak around 13:26–13:27 UT occurs simultaneously and could thus be linked to the polar cap patch at 13:27 UT. However, it should be mentioned that the two PSD at that time are described by a single fit rather than two fits as seen from the two blue circles. The slopes from the B_y PSD (panel g) are best described by a double slope throughout the majority of the pass, while the integrated power from the same PSD (panel i) is enhanced within the AO.

For the duration of the time interval chosen for the analysis we analyze 12,490 passes over the poles, roughly equally distributed over both hemispheres. This corresponds to about 400,000 power spectra for N_e and about the same amount for the B_y data.

In order to do a statistical approach, we bin the data into several regions between 50 and 90° MLat in 2° steps and between 0 and 24 hr MLT in 1 hr steps. If the satellites have several passes within a given region, leading to more than one data point within the bin, the mean of all data points within the bin is calculated for the graphs depicting the integrated power of N_e and B_y, as well as the ROTI data. For the slope probability plots we calculate the chance for a single slope by dividing the number of single slopes by the total number of passes within a bin. The double slope probability is calculated in a similar way. These two quantities are merged into a probability scale ranging from 100% single slope probability (SS probability) to 100% double slope probability (DS probability).

3. Results

We use all passes Swarm A and C made between October 2014 and December 2016 where N_e, B, and FAC data are available. Additionally, we use all passes between January 2020 and December 2022 with the same requirements. The data from the low activity timeframe (2020–2022) does not vary greatly from the high activity data (2014–2016). Additionally, the passes between 2020 and 2022 are limited by the 16 Hz N_e data which is only collected for short intervals within the given timeframe. Thus, this data can be found in Appendix A for comparison. Figure 3 shows slope probability and integrated power for high solar activity (2014–2016) obtained from the electron density PSD. The plot is divided into four seasons from spring to winter in column 1–4, respectively. The first two rows, rows a and b, show the slope probability and integrated power of the northern hemisphere (NH), respectively, while the two bottom rows, rows c and d, show the same quantities for the southern hemisphere (SH). The slope probability ranges from 100% DS probability (dark red) to 100% SS probability (dark blue). If it is equally likely to obtain a single or double slope in the corresponding bin, the bin is yellow.

Both the northern and southern hemisphere slope probability (rows a and c) show a seasonal dependency. In local summer the slope probability for a DS throughout the AO, which is typically found in around 70° MLat, and PC is close to one, especially in the PC. For both spring and autumn, the probability for a double slope is still very close to 1, however, compared to the summer, the probability in the AO becomes higher than in the PC. This ratio grows further during winter time, where the probability in the PC is nearly similar for a spectrum to exhibit a double slope as it is to exhibit a single slope. Note that the probability for a double slope stays high in the AO for all seasons. While a higher DS probability is found mostly throughout the AO and PC regions, the dayside MidLat below approximately 60° MLat shows a very high SS probability, which is also the only region where we consistently find a higher probability for a SS than a DS. In the night time below 60° MLat we rather encounter an equal slope probability. These findings hold true for both northern and southern hemisphere, though the contrast between summer and the other seasons seems to be more pronounced in the SH. Additionally, we find similar results for low solar activity (2020–2022), which can be seen in Appendix A, see Figure A1. Furthermore, the autumn season shows a higher double slope probability at lower latitudes for the midnight sector in comparison to the other seasons. Note that all seasons are local seasons, which means that the autumn data from the northern hemisphere corresponds to the same time frame as the spring data of the southern hemisphere. As both hemispheres show a higher double slope probability around midnight for lower latitudes in the autumn, this is not related to a small number of events leading to higher probabilities, but rather is to be related to the season itself.

Rows b and d show the integrated power between 1 and 2 Hz. Again, we find a seasonal dependency, though this time we find differences in the northern and southern hemisphere. In the NH the integrated power is more

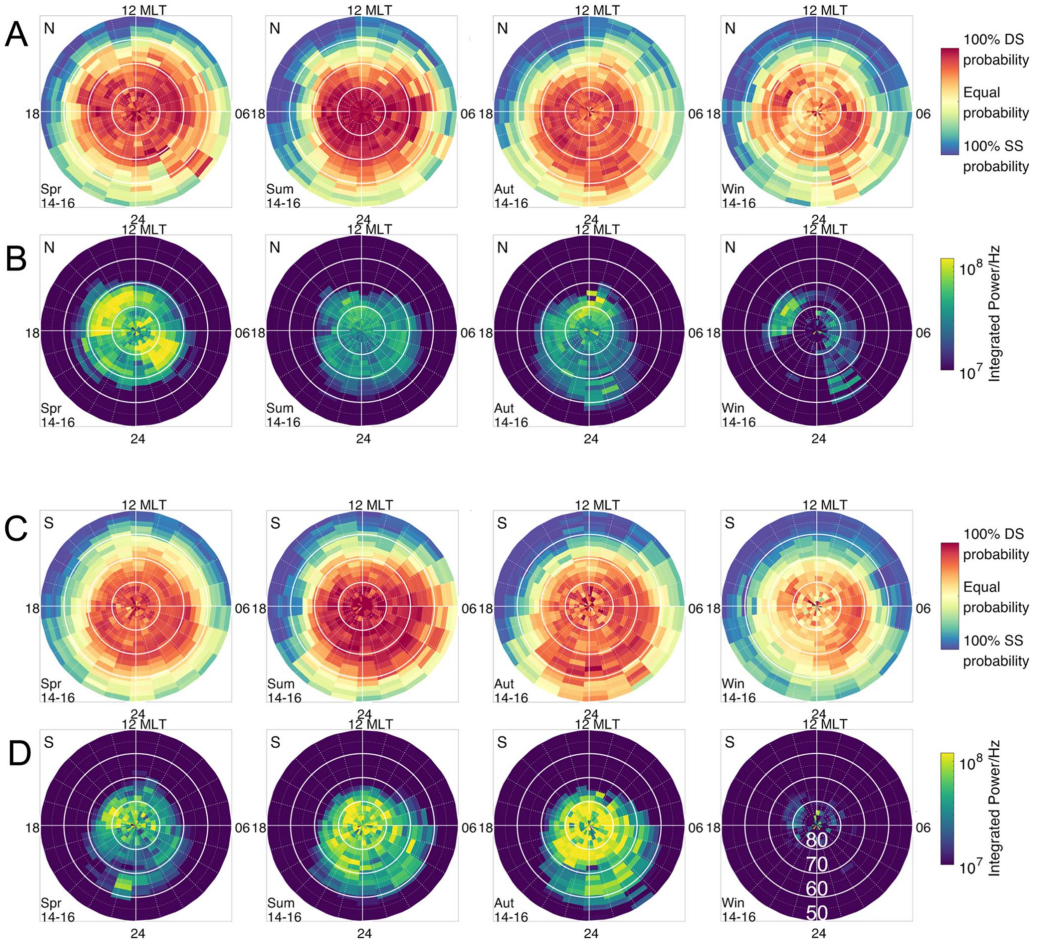

Figure 3. Slope probability and integrated power for the interval between 1 and 2 Hz obtained from the N_e PSD. The four columns contain the four seasons from spring to winter, while the four rows, rows (a–d), show the slope probability and integrated power for the northern hemisphere (rows a and b) and for the southern hemisphere (c and d) for high solar activity (years 2014–2016). All seasons are local seasons. The magnetic latitude is indicated on the bottom right plot.

pronounced around the spring and autumn equinoxes than the summer, with little integrated power throughout the winter. However, the SH has a higher integrated power in summer than spring, though autumn still exhibits the highest power. In both cases, the integrated power in local winter is significantly lower when compared to other seasons. This also holds true for low solar activity in Figures A1b and A1d. For the slope probability we obtain a lower probability for a double slope in the PC during autumn, spring and winter compared to summer, though the probability in the AO stays high. The integrated power, however, stays elevated in the PC compared to the AO, even if the overall power diminishes. Notable is also the high integrated power northward of 60° MLat around midnight during spring in the southern hemisphere (bottom left panel), which does not correspond with a higher probability for either a single or double slope. Generally, while both the double slope probability and integrated power are more pronounced throughout the AO and PC, a high integrated power is not necessarily followed by a higher double slope probability.

Another important aspect is the asymmetry between the hemispheres. The slope probability shows a high similarity for all seasons with high probabilities in the summer and diminishing probabilities for the equinoxes and winter for both high and low solar activity. However, the integrated power shows no such resemblances. Generally, the SH summer integrated power is enhanced in comparison to the other seasons, while in the northern hemisphere the integrated power around the equinoxes is more pronounced.

Figure 4 shows ROTI obtained from the IPIR data set, for the northern and southern hemispheres (row a and b, respectively). The four columns show the four seasons from spring to winter going from left to right. The northern hemisphere shows an elevated ROTI in the spring and autumn mainly in the night side auroral oval and between 70 and 80° MLat around noon. While the same areas are also enhanced during summer, the overall index is lower than around the equinoxes. Note, that the index in the NH polar cap is generally more enhanced than the index in the MidLat, though the largest enhancements are found within the AO. The southern hemisphere is generally more enhanced than the NH, though, similar to the electron density results, a difference during seasons can be observed. The local summer and autumn seasons are overall more enhanced than the other seasons, especially within the polar cap. During local spring, ROTI is mainly enhanced within the nightside auroral oval around midnight and northward of 70° MLat around noon. For both hemispheres local winter shows comparably low enhancement within all regions.

Figure 5 is displayed similar to Figure 3 and shows the slope probability and integrated power obtained from the PSD of the B_y component. The plot is divided into four seasons from spring to winter in column 1–4, respectively. The first two rows, rows a and b, show the slope probability and integrated power of the NH, respectively, while the two bottom rows, rows c and d, show the same quantities for the SH.

In both the northern and southern hemisphere the double slope probability (row a and c) is high in the AO and cusp region, typically found around noon and 75° MLat. Additionally, we find a higher double slope probability southward of 60° MLat on the nightside. While the dayside shows an equal probability for single and double slopes southward of 70° MLat for nearly all plots, there is a higher DS probability on the dayside around 50° MLat. Generally, it is either likely that we can find an equal probability or a higher probability for double slopes throughout all plots, only very little bins show a higher probability for a single slope, and if so, the bins are either located on the dayside, in the PC or directly southward of the PC around midnight. This holds true, again, for the slope probabilities during low activity, see Figure A2 in Appendix A. However, the single slope probability is still dominant in few bins. Moreover, both autumn graphs (A and C, third plot) show a stronger double slope probability between 60° MLat and 70° MLat during midnight.

The integrated power between 1 and 2 Hz (row b and d) is also most elevated in the AO throughout all plots both for high and low activity. While most of the auroral oval exhibits a more or less uniform elevated integrated power, there is higher powers found around 75° MLat around magnetic noon, thus in the cusp, for several of the plots. While the slope probability shows a strong double slope probability within the midnight section below 60° MLat, this is not the case for the integrated power.

4. Discussion

In this study we utilize over 2 years of in situ measurements from Swarm A and C data in order to investigate a connection between irregularities in the B_y component and strong electron density fluctuations in the polar ionosphere. Additionally, we use ROTI data from the IPIR data set.

We compare the slope probability and integrated power between 1 and 2 Hz of the N_e PSD in the NH and SH for solar maximum. Both quantities show a seasonal dependency, though not for the same seasons. The slope probability varies with solar EUV radiation, meaning that we find the highest probability for a double slope to describe a power spectrum in local summer months. Close to the equinoxes the probability for a DS becomes less, especially in the polar cap. This tendency becomes even stronger during winter months, where the DS probability is roughly equal to a SS probability for most parts within the PC. These results are consistent with Ivarsen et al. (2021). They have linked the existence of DS to the influence of the SZA, showing a higher DS probability with lower SZA, presenting evidence for a dependency of N_e irregularities in the polar cap on solar EUV radiation. A higher solar EUV radiation leads to an increase of conductivity in the E-region, which consequently leads to a faster decay of plasma structures in the F-region due to the coupling between both regions (Buschmann et al., 2023; Ivarsen et al., 2019, 2023; M. C. Kelley et al., 1982). The increased decay of plasma structuring

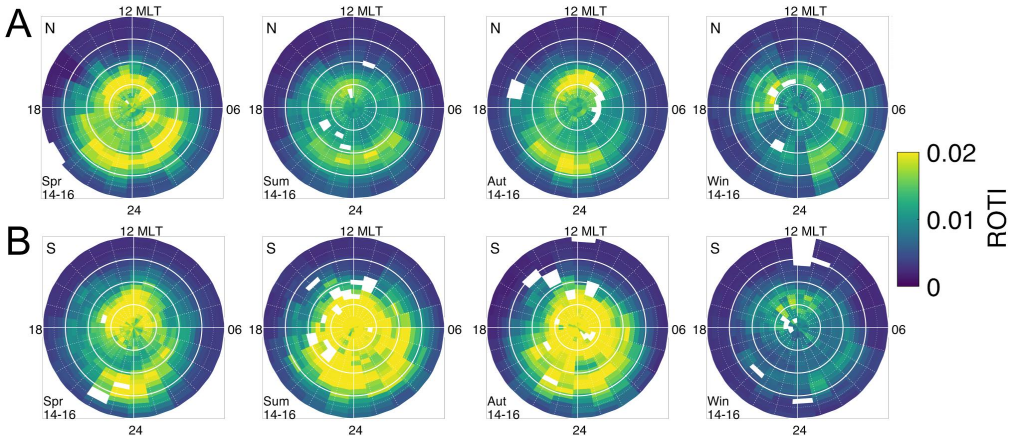

Figure 4. Rate of change of TEC Index (ROTI). The four columns contain the four seasons from spring to winter, while the two rows, rows (a and b), show the ROTI for the northern hemisphere and southern hemisphere (rows a and b, respectively) for high solar activity (years 2014–2016). All seasons are local seasons. The magnetic latitude is indicated on the bottom right plot.

together with a generally higher N_e due to solar EUV radiation leads to a PSD with higher values on large scales and lower values on small scales, thus increasing the chance to for two slopes to the corresponding spectra.

At this point it is worth mentioning that a quantity of PSD equator-ward of the AO is shallowing out, meaning the second, high-frequency slope is very flat compared to the first slope. This mainly happens in regions where N_e is smooth and unstructured. When looking at the slopes of the PSD in a turbulence context, a shallow slope is associated with an energy input in these frequencies. The algorithm that is used for slope detection, however, labels these spectra as single slopes, as the condition $p_2 - p_1 \geq 0.8$ is not met.

As mentioned within the methodology section of this study, the algorithm is only able to detect a slope in a frequency range between 0.19 and 7 Hz, which corresponds to scale sizes of approximately 1.1–40 km. Sounding rocket data have shown that breakpoints can occur on a variety of scales ranging up to 100 Hz. A variety of different frequencies may indicate a cascade from very large scales within the solar wind down to centimeter scale sizes found within the ionosphere with spectral steepening and breakpoints at several different scales stemming from different mechanisms. The 16 Hz N_e data limits the observable range up to 8 Hz corresponding to the Nyquist frequency. The spectral breaks observed within this study are occurring on kilometer scales and can thus be an indication of a redistribution of energy due to the GDI, which operates on these scale sizes, especially on the edges of polar cap patches.

The integrated power for the N_e PSD show seasonal dependencies for the NH and SH. The northern hemisphere generally shows a higher power around the equinoxes, while the southern hemisphere additionally exhibits elevated power in local summer. Generally, while the slope probability in the NH and SH are very similar, the integrated power shows no such similarity between the hemispheres and seasons. This suggests that the energy deposited in kilometer-scale structures is not necessarily linked to steepening of the PSD. The higher integrated power obtained from the N_e PSD around the equinoxes may be explained due to the tilt of the Earth's axis and the additionally slanted magnetic field, leading to a better alignment between the Earth's magnetic field and that of the solar wind. Generally, the seasonal variation of geomagnetic storms has been ascribed to both axial and equinoctal phenomena, alongside the Russell-McPherron effect (Cortie, 1912; Echer et al., 2011; Gonzalez et al., 1994; Russell & McPherron, 1973). The elevated occurrence of geomagnetic storms and the accompanying precipitating particles can then lead to a higher deposition of energy into lower frequencies, as analyzed here, around the equinoxes. An increased deposition of energy into low frequencies during particle precipitation has as well been described in Buschmann et al. (2023), who have analyzed the impact of particle precipitation on plasma structuring within different scales with sounding rockets. The study found an increase in kilometer-sized scales within the cusp aurora, which was broken down to smaller structures poleward of the cusp. The enhanced PSD in the southern

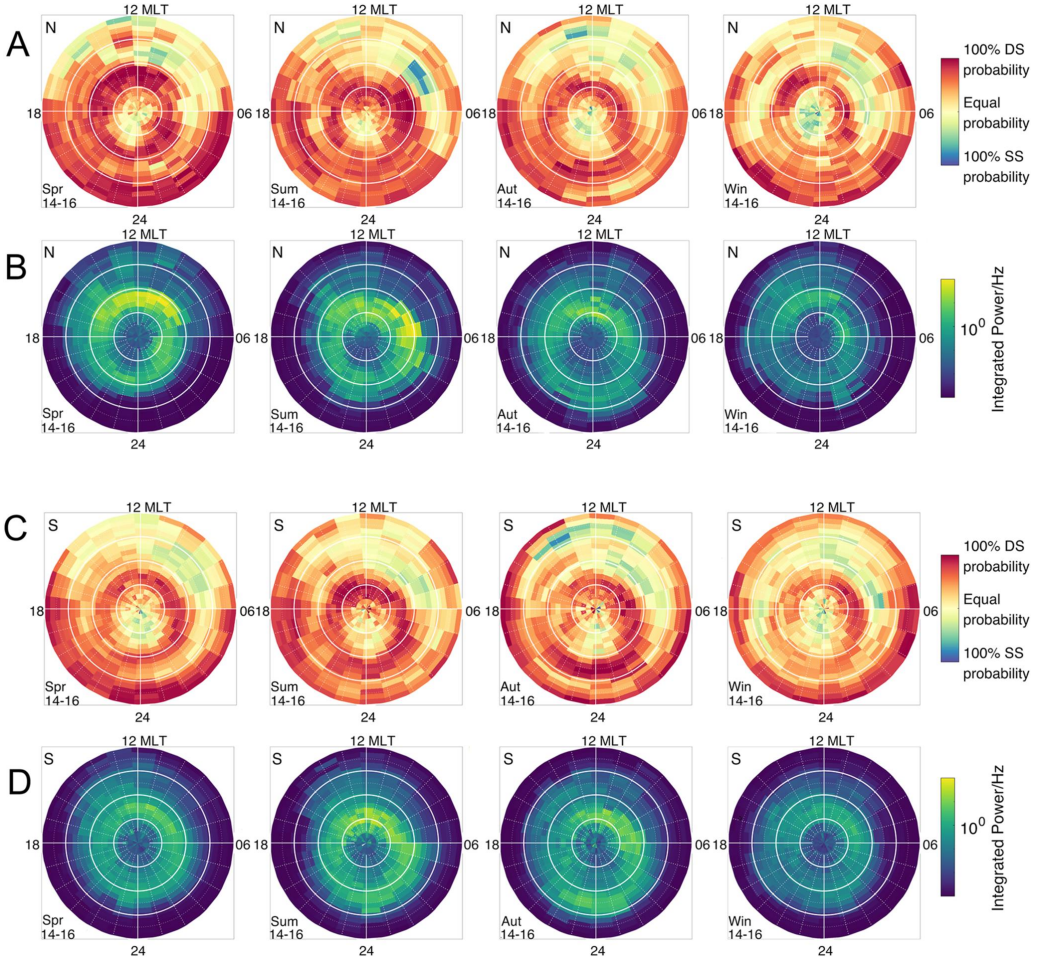

Figure 5. Slope probability and integrated power for the interval between 1 and 2 Hz obtained from the PSD of the B_y component. The four columns contain the four seasons from spring to winter, while the four rows, rows (a–d), show the slope probability and integrated power for the northern hemisphere (rows a and b) and for the southern hemisphere (c and d) for high solar activity (years 2014–2016). All seasons are local seasons. The magnetic latitude is indicated on the bottom right plot.

hemisphere within the summer months could be caused by the additional offset of the Earth's magnetic field in the SH. The magnetic pole in the SH is more than 8.5° farther from the geographic pole in the SH when compared to the NH. This results in higher illumination in the southern polar region. Convection can then lead to a higher structuring within the summer month in the SH (Coley & Heelis, 1998; Laundal et al., 2017; Noja et al., 2013). In local winter, both the NH and SH integrated power show the lowest values throughout the seasons. In addition to the 1–2 Hz interval we analyze data in between 0.1–0.6 Hz and 6–7 Hz, corresponding to scale sizes between about 10 and 80 km and of about 1 km, respectively. Both data sets show similar trends to the analysis of the 1–2 Hz interval, indicating consistent results throughout the scale sizes. As the plots yield similar results as the 1–2 Hz plots displayed within this work, we decided not to include them but rather give the short description above.

In order to get a better picture of the structuring of N_e within the polar regions, we also analyze the ROTI data within the same time-frame as the PSD analysis. The overall seasonal variation of the ROTI data aligns with the

seasonal variation that we found within the integrated power of the N_e PSD. Additionally, the interhemispheric variation that is seen within the integrated power from the N_e PSD can also be seen within this data set and is consistent with Jin and Xiong (2020). Generally, the majority of the enhanced ROTI locations also match the integrated power. However, ROTI is much more elevated within the cusp region and nightside AO in the northern hemisphere, while the southern hemisphere shows an additional pronunciation from the cusp into the nightside until the central polar cap, with a small region that exhibits a lower ROTI in the nightside PC. Similar to the integrated power, ROTI also shows a clear distinction between the NH and SH. The low ROTI in winter and higher ROTI values around the equinoxes is consistent with results in Jin et al. (2019). The integrated power is derived from the 16 Hz in situ N_e data and thus gives momentary information in the vicinity of the satellite. Additionally, we gain information on the amplitude of fluctuations within a certain scale size (here within 1–2 Hz). ROTI data, on the other hand, gives insight about the structuring of the plasma for a wider ionospheric area, as the data is obtained from GNSS signals.

In addition to the PSD analysis of N_e, we also analyze the slope probability and integrated power between 1 and 2 Hz of B_y. Both the occurrence rate for a double slope and the integrated power show elevated values within the auroral oval and within the cusp. Additionally, it is more likely for a double slope to occur below 60° MLat, especially during nighttime, however, there is no elevation within the integrated power. As B_y in this study is used instead of the FAC data, the signal within mid-latitudes is usually low, which may lead to a very low signal within the PSD. Furthermore, as seen in Figure 2, the breakpoints in the nightside mid-latitude region are very high and close to the Nyquist frequency for the B_y PSD. This adds additional uncertainty for these spectra. Thus, the double slope probability in these regions should be assessed with caution and may likely be a result of noise.

Generally, the residual magnetic field fluctuations show an integrated power enhancement in a circle around the pole, similar to the FAC data, see Figure A3. In addition, the highest values are found in the morning sector and the cusp for all seasons and both hemispheres, indicating dayside precipitation. An increased integrated power within these scales indicates an enhancement in Poynting flux. The Poynting flux gives a measure of electromagnetic energy moving between the magnetosphere and the ionosphere through the FAC. Generally, the Poynting Flux can be divided into large scale variations along the R1/R2 FAC system (Iijima & Potemra, 1976), or into variations on small scales, usually below 10 km, where Alfvénic energy plays a large role (Knudsen et al., 1992). The integrated power we analyze within this study corresponds to scale sizes of a few kilometers, falling into the range below 10 km. This indicates that the increased integrated power we obtain gives a measure on the downward Poynting flux dominated by Alfvénic energy. In recent years, studies with the Swarm satellites have been conducted to present maps of the Poynting flux in the northern and southern hemisphere (Billett et al., 2022; Ivarsen et al., 2020). The climatology we present of the B_y integrated power maps onto the Poynting flux within these studies adequately with an overall increase in Poynting flux in a circular shape around the magnetic pole and a further increase within the cusp.

It has also been shown that Alfvén waves contribute significantly to the energy input into the auroral acceleration region. The applied energy can then trigger amongst others particle precipitation into the ionosphere and thus formation of aurora (Angelopoulos et al., 2002; Chaston, 2006; Keiling, 2009; Wygant et al., 2000).

The enhancements within B_y integrated power in the cusp are also co-located with the strong ROTI enhancements as seen in Figure 4. This agrees with previous results that show how auroral dynamics within the cusp can be related to irregularities leading to high values of phase scintillations indices based on GNSS signals (Clausen et al., 2016; Jin et al., 2015, 2017). This also agrees with Fæhn Follestad et al. (2020), who showed that filamentary FACs are co-located with high phase scintillation indices in the cusp.

5. Conclusion

We present analysis of more than 2 years of data from the 16 Hz electron density, the 50 Hz magnetic field and ROTI data from the IPIR data set from Swarm A and C. Additionally, we use 3 years of a complementary data set from Swarm A and C for a time frame around solar minimum for discussion. We have been able to find new results and give new insights, as well as confirm previously found results from different studies with our methods. The probability for a DS within the N_e PSD follows a seasonal variation that changes with EUV radiation within the PC. For both hemispheres we observe the highest DS probability in local summer. Both equinoxes show lower probability, while the winter season shows the lowest probability. The DS probability within the AO is constantly

high and is thus independent of solar EUV and rather depends on auroral dynamics. Higher solar EUV photo-ionization causes an upturn in E-region conductivity leading to a faster decay of structures in F-region plasma. With an overall increase in N_e within summer due to solar EUV radiation, this increases the DS probability in the summer, but overall indicates less small-scale structuring in the polar cap in the summer months. The integrated power within the 1–2 Hz frequency interval also shows a seasonal variation, however, the variation does not correlate to solar EUV radiation, but rather has its strongest values around the equinoxes and the lowest values in winter. Additionally, while the DS probability shows little difference between the hemispheres, the integrated power shows much higher variability, especially within local summer months. This is likely attributed to the large offset of the magnetic pole in the southern hemisphere. The ROTI values show a similar variation as the integrated power obtained from N_e. However, while the integrated power, especially in the NH, shows a similar elevation for the AO and PC, the ROTI values show higher elevation within the midnight auroral oval and within the cusp. The overall seasonal variation of ROTI has been seen before, however, this study gives a seasonal climatology of the results and thus expands on the already existing studies. While the integrated power generally gives a measure of the strength of fluctuations and structuring, similar to ROTI, the results are limited to certain spatial scales. The integrated power within both hemispheres is mainly enhanced within the PC and AO, though varying in strength. Generally, ROTI shows enhancements within the same regions, however, the midnight AO and the cusp show further heightened values, thus indicating higher structuring within these regions. We also find higher values of the integrated power of B_y within the cusp, co-located with the ROTI data. The enhancements within the B_y integrated power also match with previous studies which analyzed the Poynting flux from the Swarm satellite. The enhancements within the cusp correspond to spatial scales below 10 km and are thus on scales where Alfvénic energy plays a large role. The increased values within the cusp may thus be linked to an increase in precipitating particles into the cusp.

The B_y DS probability, as well as the N_e SS probability are enhanced within mid-latitudes. The low signals for both N_e and B_y in mid-latitudes can lead to uncertainty in the assessment of the spectral index due to the low signal in the PSD. Furthermore, N_e may exhibit a shallow second slope in regions of smooth or unstructured plasma, as it is found within mid-latitudes. As the condition for the algorithm of $p_2 - p_1 \geq 0.8$ is not met, these spectra may be labeled as a single slope, even though turbulence theory associates a more shallow slope with an input of energy. Additionally, we encounter breakpoints for the B_y PSD close to the Nyquist frequency we obtain for the 50 Hz data, which adds uncertainty to this data set within mid-latitudes. The data within this region should thus be viewed with caution.

This study has implications for a better understanding of plasma structuring in the ionosphere and models for space weather effects. Structures in the electron density on scales assessed in this study of between a few hundred and a few kilometers have been shown to lead to elevated phase scintillations indices, σ_Φ, calculated for incoming GNSS signals (Jin et al., 2017; Kintner et al., 2007). Additionally, due to the turbulent cascade and energy redistribution within the ionosphere, the existence of kilometer-sized structures can sometimes be directly linked to the formation of sub-kilometer sized structures (Hamza et al., 2024). Under these conditions, when sub-kilometer sized structures are present, diffractive effects can lead to GNSS scintillations of stochastic nature which can be observed as elevated scintillation indices. This effect is mostly pronounced in the cusp region (Meziane et al., 2020). However, we note that very often the large scale structuring in TEC leads to elevated σ_Φ, but not amplitude scintillations (Enengl et al., 2024; Zheng et al., 2022). This is often the case in regions close to the auroral oval. Thus, elevated ROTI can often be an indication of large scale structuring, which can lead to problems such as loss-of-lock. A better understanding of plasma structuring and the redistribution of energy can thus aid in improving forecasting and modeling of space weather effects.

To summarize, we can present the main results of this paper as follows:

- The probability to obtain a double slope in the N_e PSD shows a seasonal dependency on the influence of solar-EUV and little variation between the northern and southern hemisphere. The integrated power within the frequency interval of 1–2 Hz from the same PSD shows a seasonal dependency with higher power during the equinoxes and a strong interhemispheric variation. A connection between the two quantities can thus not be shown within the scope of this study.
- ROTI data shows similar behavior to the integrated power from the N_e PSD but shows larger enhancements within the cusp and nightside auroral oval, which may indicate different drivers for instabilities within these regions.

- The strongest fluctuations within B_y are found within the cusp for all seasons and both hemispheres. These enhancements can be linked to an increase in downward Poynting flux on scales below 10 km which corresponds to an increase in Alfvén energy. The enhancements in B_y are additionally co-located with strong ROTI values.

In order to achieve a better picture of the redistribution of irregularities in the polar ionosphere, it would be beneficial in the future to use data with a higher sampling rate in order to map the energy contained over a large range of scales.

Appendix A: Additional Data

Complimentary data sets from January 2020 to December 2022 have been analyzed for comparison. Figure A1 shows slope probability and integrated power for low solar activity (2020–2022) obtained from the electron

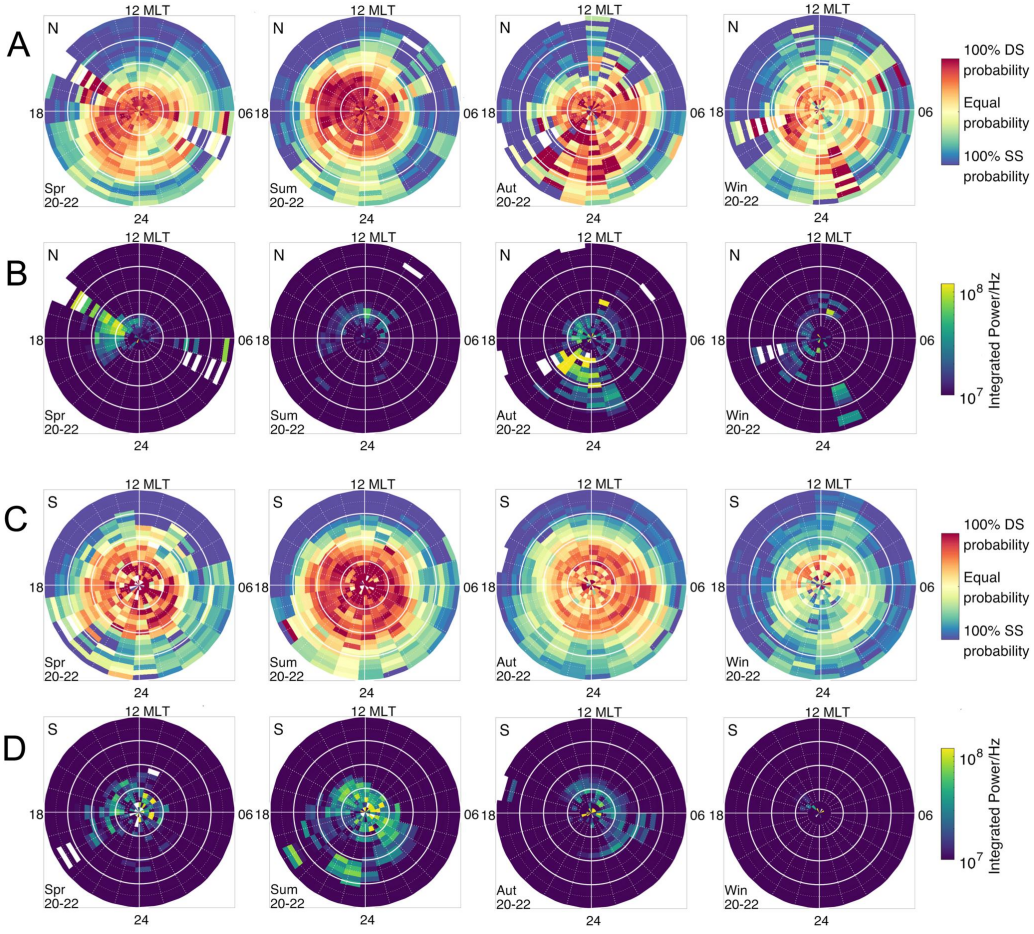

Figure A1. Slope probability and integrated power for the interval between 1 and 2 Hz obtained from the N_e PSD. The four columns contain the four seasons from spring to winter, while the four rows, rows (a–d), show the slope probability and integrated power for the northern hemisphere (rows a and b) and for the southern hemisphere (c and d) for low solar activity (years 2020–2022).

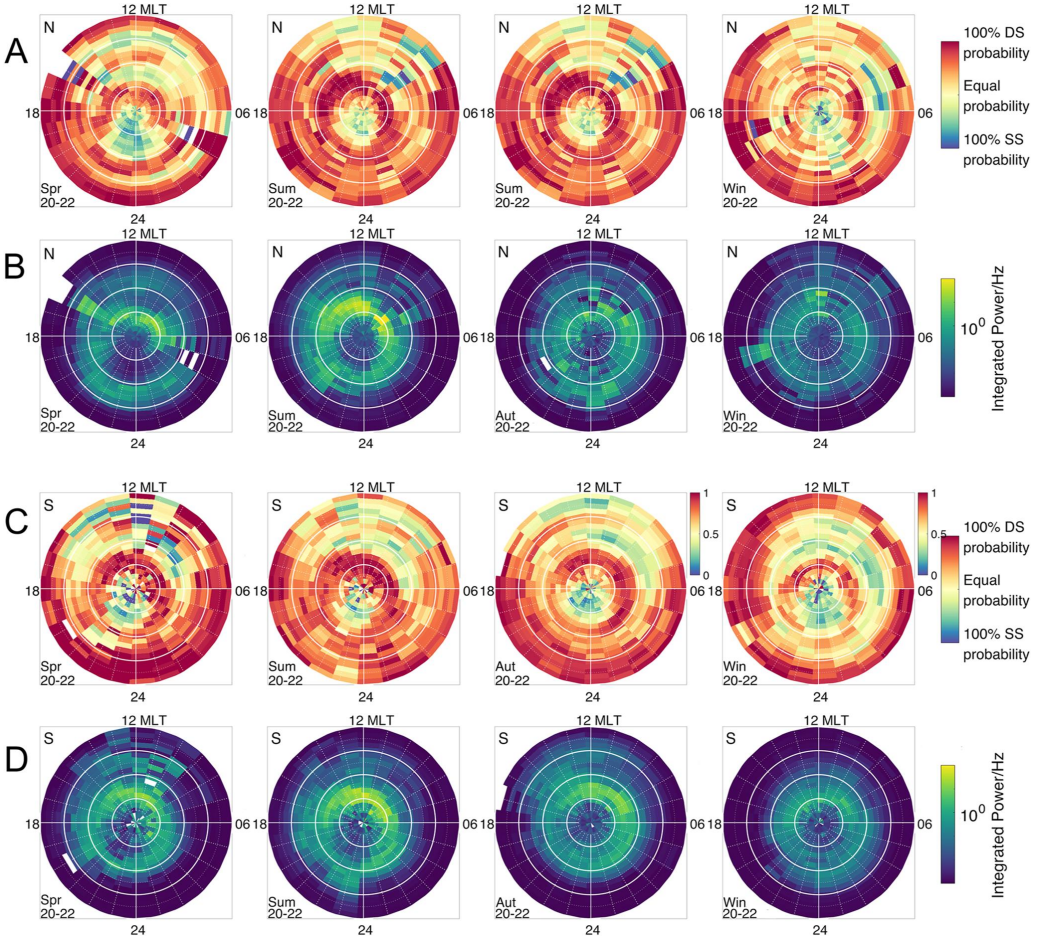

Figure A2. Slope probability and integrated power for the interval between 1 and 2 Hz obtained from the B_y PSD. The four columns contain the four seasons from spring to winter, while the four rows, rows (a–d), show the slope probability and integrated power for the northern hemisphere (rows a and b) and for the southern hemisphere (c and d) for low solar activity (years 2020–2022).

density PSD. The plot is divided into four seasons from spring to winter in column 1–4, respectively. The first two rows, rows a and b, show the slope probability and integrated power of the northern hemisphere (NH), respectively, while the two bottom rows, rows c and d, show the same quantities for the southern hemisphere (SH). The slope probability ranges from 100% DS probability (dark red) to 100% SS probability (dark blue). If it is equally likely to obtain a single or double slope in the corresponding bin, the bin is yellow. Figure A2 shows the same quantities obtained from the B_y PSD. Figure A3 shows the 1 Hz FAC data. The two top rows, rows a and b, show the FAC in the northern hemisphere for high solar activity (row a) and low solar activity (row b), while the two bottom rows, rows c and d, show the FAC in the southern hemisphere for high solar activity (row c) and for low solar activity (row d).

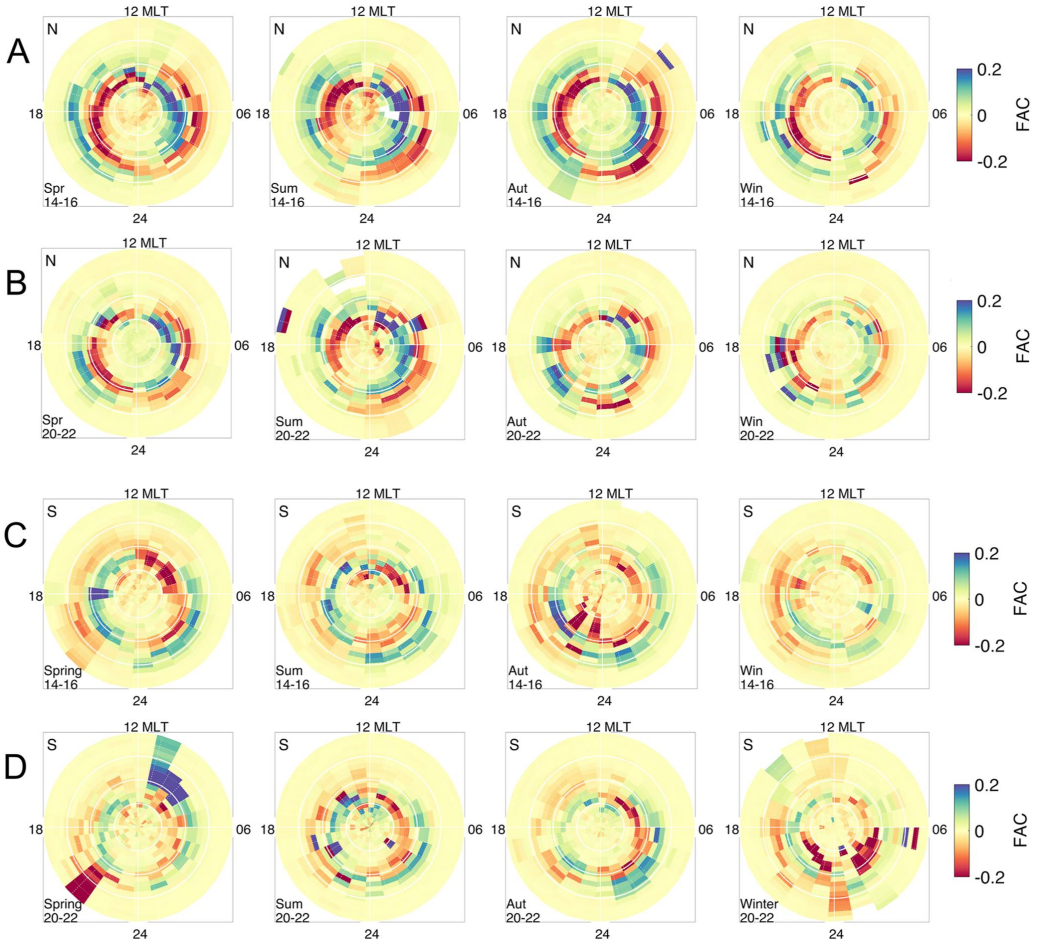

Figure A3. Field aligned current from the 1 Hz Swarm FAC data. The four columns contain the four seasons from spring to winter, while the four rows, rows (a–d), show the FAC for the northern hemisphere (rows a and b) for high solar activity (row a) and low solar activity (row b), and for the southern hemisphere (c and d) for high solar activity (row c) and low solar activity (row d).

Data Availability Statement

The European Space Agency's Swarm data, including the IPIR product, can be accessed at https://swarm-diss.eo.esa.int. Information about the Swarm data can be taken from the Swarm Data Handbook in ESA (n.d.), https://swarmhandbook.earth.esa.int.

Acknowledgments
This work was partially conducted within the 4DSpace research initiative at UiO. The study was supported in part by the European Research Council (ERC) under the European Union's Horizon 2020 research and innovation programme (Grant 866357). AS acknowledges the Research Council of Norway (RCN) (Grant 326039) and the UiT The Arctic University of Norway contribution to the EISCAT3D project (RCN funded research infrastructure Grant 245683).

References

AD, R. (1995). Ionospheric electrodynamics using magnetic apex coordinates. *Journal of geomagnetism and geoelectricity*, *47*(2), 191–212. https://doi.org/10.5636/jgg.47.191

Angelopoulos, V., Chapman, J., Mozer, F., Scudder, J., Russell, C., Tsuruda, K., et al. (2002). Plasma sheet electromagnetic power generation and its dissipation along auroral field lines. *Journal of Geophysical Research*, *107*(A8), SMP–14. https://doi.org/10.1029/2001JA900136

Basu, B., & Coppi, B. (1988). Fluctuations associated with sheared velocity regions near auroral arcs. *Geophysical research letters*, *15*(5), 417–420. https://doi.org/10.1029/gl015i005p00417

Basu, S., Basu, S., MacKenzie, E., Coley, W., Sharber, J., & Hoegy, W. (1990). Plasma structuring by the gradient drift instability at high latitudes and comparison with velocity shear driven processes. *Journal of Geophysical Research*, *95*(A6), 7799–7818. https://doi.org/10.1029/JA095iA06p07799

Billett, D. D., McWilliams, K. A., Pakhotin, I. P., Burchill, J. K., Knudsen, D. J., & Martin, C. J. (2022). High-resolution Poynting flux statistics from the swarm mission: How much is being underestimated at larger scales? *Journal of Geophysical Research: Space Physics*, *127*(7), e2022JA030573. https://doi.org/10.1029/2022JA030573

Buschmann, L. M., Spicher, A., Clausen, L. B., Marholm, S., & Miloch, W. J. (2023). The role of particle precipitation at different altitudes by in-situ measurements. *Journal of Space Weather and Space Climate*, *13*, 1. https://doi.org/10.1051/swsc/2023012

Carlson, H. C. (2012). Sharpening our thinking about polar cap ionospheric patch morphology, research, and mitigation techniques. *Radio Science*, *47*(4). https://doi.org/10.1029/2011RS004946

Carlson, H. C., Pedersen, T., Basu, S., Keskinen, M., & Moen, J. (2007). Case for a new process, not mechanism, for cusp irregularity production. *Journal of Geophysical Research*, *112*(A11), A11304. https://doi.org/10.1029/2007JA012384

Carrano, C. S., Groves, K. M., McNeil, W. J., & Doherty, P. H. (2013). Direct measurement of the residual in the ionosphere-free linear combination during scintillation. In *Proceedings of the 2013 international technical meeting of the institute of navigation* (pp. 585–596).

Chartier, A. T., Huba, J., & Mitchell, C. N. (2019). On the annual asymmetry of high-latitude sporadic F. *Space Weather*, *17*(11), 1618–1626. https://doi.org/10.1029/2019SW002305

Chartier, A. T., Mitchell, C. N., & Miller, E. S. (2018). Annual occurrence rates of ionospheric polar cap patches observed using Swarm. *Journal of Geophysical Research: Space Physics*, *123*(3), 2327–2335. https://doi.org/10.1002/2017JA024811

Chaston, C. (2006). ULF waves and auroral electrons. *Magnetospheric ULF waves: Synthesis and new directions*, *169*, 239–257. https://doi.org/10.1029/169GM16

Clausen, L., Moen, J., Hosokawa, K., & Holmes, J. (2016). GPS scintillations in the high latitudes during periods of dayside and nightside reconnection. *Journal of Geophysical Research: Space Physics*, *121*(4), 3293–3309. https://doi.org/10.1002/2015JA022199

Coley, W., & Heelis, R. (1998). Seasonal and universal time distribution of patches in the northern and southern polar caps. *Journal of Geophysical Research*, *103*(A12), 29229–29237. https://doi.org/10.1029/1998JA900005

Cortie, A. (1912). Sun-spots and terrestrial magnetic phenomena, 1898-1911. *Monthly Notices of the Royal Astronomical Society*, *73*(1), 52–60. https://doi.org/10.1093/mnras/73.1.52

Crowley, G., Schoendorf, J., Roble, R. G., & Marcos, F. A. (1996). Cellular structures in the high-latitude thermosphere. *Journal of Geophysical Research*, *101*(A1), 211–223. https://doi.org/10.1029/95JA02584

David, M., Sojka, J. J., Schunk, R. W., & Coster, A. J. (2019). Hemispherical shifted symmetry in polar cap patch occurrence: A survey of GPS TEC maps from 2015–2018. *Geophysical Research Letters*, *46*(19), 10726–10734. https://doi.org/10.1029/2019GL083952

De Franceschi, G., Spogli, L., Alfonsi, L., Romano, V., Cesaroni, C., & Hunstad, I. (2019). The ionospheric irregularities climatology over Svalbard from solar cycle 23. *Scientific reports*, *9*(1), 9232. https://doi.org/10.1038/s41598-019-44829-5

D'Errico, J. (2017). SLM—Shape language modeling. (MATLAB File Exchange). Retrieved from https://se.mathworks.com/matlabcentral/fileexchange/24443%2Dslm%2Dshape%2Dlanguage%2Dmodeling

Di Mare, F., Spicher, A., Clausen, L. B. N., Miloch, W. J., & Moen, J. I. (2021). Turbulence and intermittency in the winter cusp ionosphere studied with the ICI sounding rockets. *Journal of Geophysical Research: Space Physics*, *126*(8), e2021JA029150. https://doi.org/10.1029/2021JA029150

Echer, E., Gonzalez, W., & Tsurutani, B. (2011). Statistical studies of geomagnetic storms with peak Dst—50 nT from 1957 to 2008. *Journal of Atmospheric and Solar-Terrestrial Physics*, *73*(11–12), 1454–1459. https://doi.org/10.1016/j.jastp.2011.04.021

Emmert, J., Richmond, A., & Drob, D. (2010). A computationally compact representation of magnetic-apex and quasi-dipole coordinates with smooth base vectors. *Journal of Geophysical Research*, *115*(A8), A08322. https://doi.org/10.1029/2010JA015326

Enengl, F., Spogli, L., Kotova, D., Jin, Y., Oksavik, K., Partamies, N., & Miloch, W. (2024). Investigation of ionospheric small-scale plasma structures associated with particle precipitation. *Space Weather*, *22*(1), e2023SW003605. https://doi.org/10.1029/2023sw003605

ESA. (n.d.). Swarm data handbook. Retrieved from https://swarmhandbook.earth.esa.int

Fæhn Follestad, A., Herlingshaw, K., Ghadjari, H., Knudsen, D. J., McWilliams, K. A., Moen, J. I., et al. (2020). Dayside field-aligned current impacts on ionospheric irregularities. *Geophysical Research Letters*, *47*(11), e2019GL086722. https://doi.org/10.1029/2019GL086722

Friis-Christensen, E., Lühr, H., & Hulot, G. (2006). Swarm: A constellation to study the Earth's magnetic field. *Earth, Planets and Space*, *58*(4), 351–358. https://doi.org/10.1186/BF03351933

Friis-Christensen, E., Lühr, H., Knudsen, D., & Haagmans, R. (2008). Swarm–an Earth observation mission investigating geospace. *Advances in Space Research*, *41*(1), 210–216. https://doi.org/10.1016/j.asr.2006.10.008

Frisch, U., & Kolmogorov, A. N. (1995). *Turbulence: The legacy of an Kolmogorov*. Cambridge University Press.

Ghobadi, H., Spogli, L., Alfonsi, L., Cesaroni, C., Cicone, A., Linty, N., et al. (2020). Disentangling ionospheric refraction and diffraction effects in GNSS raw phase through fast iterative filtering technique. *GPS Solutions*, *24*(3), 85. https://doi.org/10.1007/s10291-020-01001-1

Gonzalez, W., Joselyn, J.-A., Kamide, Y., Kroehl, H. W., Rostoker, G., Tsurutani, B. T., & Vasyliunas, V. (1994). What is a geomagnetic storm? *Journal of Geophysical Research*, *99*(A4), 5771–5792. https://doi.org/10.1029/93JA02867

Hamza, A. M., Song, K., Meziane, K., & Jayachandran, P. (2024). Two-component phase scintillation spectra in the auroral region: Observations and model. *Journal of Geophysical Research: Space Physics*, *129*(1), e2023JA031998. https://doi.org/10.1029/2023ja031998

Hosokawa, K., Taguchi, S., Ogawa, Y., & Sakai, J. (2013). Two-dimensional direct imaging of structuring of polar cap patches. *Journal of Geophysical Research: Space Physics*, *118*(10), 6536–6543. https://doi.org/10.1002/jgra.50577

Hysell, D., Kelley, M., Swartz, W., Pfaff, R., & Swenson, C. (1994). Steepened structures in equatorial spread F: 1. New observations. *Journal of Geophysical Research*, *99*(A5), 8827–8840. https://doi.org/10.1029/93JA02961

Iijima, T., & Potemra, T. A. (1976). The amplitude distribution of field-aligned currents at northern high latitudes observed by triad. *Journal of Geophysical Research*, *81*(13), 2165–2174. https://doi.org/10.1029/JA081i013p02165

Ivarsen, M. F., Jin, Y., Spicher, A., & Clausen, L. B. (2019). Direct evidence for the dissipation of small-scale ionospheric plasma structures by a conductive e region. *Journal of Geophysical Research: Space Physics*, *124*(4), 2935–2942. https://doi.org/10.1029/2019JA026500

Ivarsen, M. F., Park, J., Kwak, Y.-S., Jin, Y., Knudsen, D. J., & Clausen, L. B. (2020). Observational evidence for the role of hall conductance in Alfvén wave reflection. *Journal of Geophysical Research: Space Physics*, *125*(12), e2020JA028119. https://doi.org/10.1029/2020JA028119

Ivarsen, M. F., St-Maurice, J.-P., Hussey, G., Spicher, A., Jin, Y., Lozinsky, A., et al. (2023). Measuring small-scale plasma irregularities in the high-latitude E-and F-regions simultaneously. *Scientific Reports*, *13*(1), 11579. https://doi.org/10.1038/s41598-023-38777-4

Ivarsen, M. F., St-Maurice, J.-P., Jin, Y., Park, J., Miloch, W., Spicher, A., et al. (2021). Steepening plasma density spectra in the ionosphere: The crucial role played by a strong E-region. *Journal of Geophysical Research: Space Physics*, *126*(8), e2021JA029401. https://doi.org/10.1029/2021JA029401

Jahn, J.-M., & LaBelle, J. (1998). Rocket measurements of high-altitude spread F irregularities at the magnetic dip equator. *Journal of Geophysical Research*, *103*(A10), 23427–23441. https://doi.org/10.1029/97JA02636

Jin, Y., Kotova, D., Xiong, C., Brask, S. M., Clausen, L. B., Kervalishvili, G., et al. (2022). Ionospheric plasma irregularities-IPIR-data product based on data from the Swarm satellites. *Journal of Geophysical Research: Space Physics*, *127*(4), e2021JA030183. https://doi.org/10.1029/2021JA030183

Jin, Y., Moen, J. I., & Miloch, W. J. (2014). GPS scintillation effects associated with polar cap patches and substorm auroral activity: Direct comparison. *Journal of Space Weather and Space Climate*, *4*, A23. https://doi.org/10.1051/swsc/2014019

Jin, Y., Moen, J. I., & Miloch, W. J. (2015). On the collocation of the cusp aurora and the GPS phase scintillation: A statistical study. *Journal of Geophysical Research: Space Physics*, *120*(10), 9176–9191. https://doi.org/10.1002/2015JA021449

Jin, Y., Moen, J. I., Oksavik, K., Spicher, A., Clausen, L. B., & Miloch, W. J. (2017). GPS scintillations associated with cusp dynamics and polar cap patches. *Journal of Space Weather and Space Climate*, *7*, A23. https://doi.org/10.1051/swsc/2017022

Jin, Y., Spicher, A., Xiong, C., Clausen, L. B., Kervalishvili, G., Stolle, C., & Miloch, W. J. (2019). Ionospheric plasma irregularities characterized by the Swarm satellites: Statistics at high latitudes. *Journal of Geophysical Research: Space Physics*, *124*(2), 1262–1282. https://doi.org/10.1029/2018JA026063

Jin, Y., & Xiong, C. (2020). Interhemispheric asymmetry of large-scale electron density gradients in the polar cap ionosphere: UT and seasonal variations. *Journal of Geophysical Research: Space Physics*, *125*(2), e2019JA027601. https://doi.org/10.1029/2019JA027601

Kagawa, A., Hosokawa, K., Ogawa, Y., Ebihara, Y., & Kadokura, A. (2021). Occurrence distribution of polar cap patches: Dependences on UT, season and hemisphere. *Journal of Geophysical Research: Space Physics*, *126*(1), e2020JA028538. https://doi.org/10.1029/2020JA028538

Keiling, A. (2009). Alfvén waves and their roles in the dynamics of the Earth's magnetotail: A review. *Space Science Reviews*, *142*(1–4), 73–156. https://doi.org/10.1007/s11214-008-9463-8

Kelley, M., Pfaff, R., Baker, K., Ulwick, J., Livingston, R., Rino, C., & Tsunoda, R. (1982). Simultaneous rocket probe and radar measurements of equatorial spread F—Transitional and short wavelength results. *Journal of Geophysical Research*, *87*(A3), 1575–1588. https://doi.org/10.1029/JA087iA03p01575

Kelley, M. C., Vickrey, J. F., Carlson, C., & Torbert, R. (1982). On the origin and spatial extent of high-latitude F region irregularities. *Journal of Geophysical Research*, *87*(A6), 4469–4475. https://doi.org/10.1029/JA087iA06p04469

Keskinen, M., & Huba, J. (1990). Nonlinear evolution of high-latitude ionospheric interchange instabilities with scale-size-dependent magnetospheric coupling. *Journal of Geophysical Research*, *95*(A9), 15157–15166. https://doi.org/10.1029/ja095ia09p15157

Keskinen, M. J., & Ossakow, S. (1983). Theories of high-latitude ionospheric irregularities: A review. *Radio science*, *18*(06), 1077–1091. https://doi.org/10.1029/rs018i006p01077

Kintner, P. M., Ledvina, B. M., & De Paula, E. (2007). GPS and ionospheric scintillations. *Space weather*, *5*(9). https://doi.org/10.1029/2006SW000260

Kintner, P. M., & Seyler, C. E. (1985). The status of observations and theory of high latitude ionospheric and magnetospheric plasma turbulence. *Space science reviews*, *41*(1), 91–129. https://doi.org/10.1007/bf00241347

Knudsen, D., Kelley, M., & Vickrey, J. (1992). Alfvén waves in the auroral ionosphere: A numerical model compared with measurements. *Journal of Geophysical Research*, *97*(A1), 77–90. https://doi.org/10.1029/91JA02300

LaBelle, J., Kelley, M., & Seyler, C. (1986). An analysis of the role of drift waves in equatorial spread F. *Journal of Geophysical Research*, *91*(A5), 5513–5525. https://doi.org/10.1029/JA091iA05p05513

Laundal, K. M., Cnossen, I., Milan, S. E., Haaland, S., Coxon, J., Pedatella, N., et al. (2017). North–south asymmetries in Earth's magnetic field: Effects on high-latitude geospace. *Space Science Reviews*, *206*(1–4), 225–257. https://doi.org/10.1007/s11214-016-0273-0

McCaffrey, A., & Jayachandran, P. (2019). Determination of the refractive contribution to GPS phase "scintillation". *Journal of Geophysical Research: Space Physics*, *124*(2), 1454–1469. https://doi.org/10.1029/2018ja025759

Meziane, K., Kashcheyev, A., Patra, S., Jayachandran, P., & Hamza, A. (2020). Solar cycle variations of GPS amplitude scintillation for the polar region. *Space Weather*, *18*(8), e2019SW002434. https://doi.org/10.1029/2019sw002434

Moen, J., Oksavik, K., Abe, T., Lester, M., Saito, Y., Bekkeng, T., & Jacobsen, K. (2012). First in-situ measurements of hf radar echoing targets. *Geophysical Research Letters*, *39*(7), L07104. https://doi.org/10.1029/2012GL051407

Moen, J., Oksavik, K., Alfonsi, L., Daabakk, Y., Romano, V., & Spogli, L. (2013). Space weather challenges of the polar cap ionosphere. *Journal of Space Weather and Space Climate*, *3*, A02. https://doi.org/10.1051/swsc/2013025

Moen, J., Walker, I., Kersley, L., & Milan, S. (2002). On the generation of cusp HF backscatter irregularities. *Journal of Geophysical Research*, *107*(A4), SIA–3. https://doi.org/10.1029/2001JA000111

Noja, M., Stolle, C., Park, J., & Lühr, H. (2013). Long-term analysis of ionospheric polar patches based on CHAMP TEC data. *Radio Science*, *48*(3), 289–301. https://doi.org/10.1002/rds.20033

Oksavik, K., Moen, J., Lester, M., Bekkeng, T. A., & Bekkeng, J. K. (2012). In situ measurements of plasma irregularity growth in the cusp ionosphere. *Journal of Geophysical Research*, *117*(A11). A11301. https://doi.org/10.1029/2012ja017835

Pfaff, R. F., Jr., Marionni, P. A., & Swartz, W. E. (1997). Wavevector observations of the two-stream instability in the daytime equatorial electrojet. *Geophysical research letters*, *24*(13), 1671–1674. https://doi.org/10.1029/97GL01535

Prakash, S., Gupta, S., Subbaraya, B., & Jain, C. (1971). Electrostatic plasma instabilities in the equatorial electrojet. *Nature Physical Science*, *233*(38), 56–58. https://doi.org/10.1038/physci233056a0

Rino, C., Morton, Y., Breitsch, B., & Carrano, C. (2019). Stochastic TEC structure characterization. *Journal of Geophysical Research: Space Physics*, *124*(12), 10571–10579. https://doi.org/10.1029/2019ja026958

Ritter, P., Lühr, H., & Rauberg, J. (2013). Determining field-aligned currents with the Swarm constellation mission. *Earth, Planets and Space*, *65*(11), 1285–1294. https://doi.org/10.5047/eps.2013.09.006

Russell, C., & McPherron, R. (1973). Semiannual variation of geomagnetic activity. *Journal of Geophysical Research*, *78*(1), 92–108. https://doi.org/10.1029/JA078i001p00092

Spicher, A., Clausen, L. B. N., Miloch, W. J., Lofstad, V., Jin, Y., & Moen, J. I. (2017). Interhemispheric study of polar cap patch occurrence based on Swarm in situ data. *Journal of Geophysical Research: Space Physics*, *122*(3), 3837–3851. https://doi.org/10.1002/2016JA023750

Spicher, A., LaBelle, J., Bonnell, J. W., Roglans, R., Moser, C., Fuselier, S. A., et al. (2022). Interferometric study of ionospheric plasma irregularities in regions of phase scintillations and HF backscatter. *Geophysical Research Letters*, *49*(12), e2021GL097013. https://doi.org/10.1029/2021GL097013

Spicher, A., Miloch, W., & Moen, J. (2014). Direct evidence of double-slope power spectra in the high-latitude ionospheric plasma. *Geophysical Research Letters*, *41*(5), 1406–1412. https://doi.org/10.1002/2014GL059214

Spogli, L., Ghobadi, H., Cicone, A., Alfonsi, L., Cesaroni, C., Linty, N., et al. (2021). Adaptive phase detrending for GNSS scintillation detection: A case study over Antarctica. *IEEE Geoscience and Remote Sensing Letters*, *19*, 1–5. https://doi.org/10.1109/lgrs.2021.3067727

Tröbs, M., & Heinzel, G. (2006). Improved spectrum estimation from digitized time series on a logarithmic frequency axis. *Measurement*, *39*(2), 120–129. https://doi.org/10.1016/j.measurement.2005.10.010

Tsunoda, R. T. (1988). High-latitude F region irregularities: A review and synthesis. *Reviews of Geophysics*, *26*(4), 719–760. https://doi.org/10.1029/RG026i004p00719

van der Meeren, C., Oksavik, K., Lorentzen, D. A., Rietveld, M. T., & Clausen, L. B. (2015). Severe and localized GNSS scintillation at the poleward edge of the nightside auroral oval during intense substorm aurora. *Journal of Geophysical Research: Space Physics*, *120*(12), 10–607. https://doi.org/10.1002/2015JA021819

Villain, J., Hanuise, C., & Beghin, C. (1986). ARCAD3-SAFARI coordinated study of auroral and polar F-region ionospheric irregularities. *Annales geophysicae*, *4*, 61–68.

Wang, H., Lühr, H., & Ma, S. (2005). Solar zenith angle and merging electric field control of field-aligned currents: A statistical study of the southern hemisphere. *Journal of Geophysical Research*, *110*(A3), A03306. https://doi.org/10.1029/2004JA010530

Wang, Y., Jayachandran, P., Ma, Y.-Z., Zhang, Q.-H., Xing, Z.-Y., Ruohoniemi, J., et al. (2022). Dependencies of GPS scintillation indices on the ionospheric plasma drift and rate of change of TEC around the dawn sector of the polar ionosphere. *Journal of Geophysical Research: Space Physics*, *127*(11), e2022JA030870. https://doi.org/10.1029/2022ja030870

Wang, Y., Zhang, Q.-H., Jayachandran, P., Moen, J., Xing, Z.-Y., Chadwick, R., et al. (2018). Experimental evidence on the dependence of the standard GPS phase scintillation index on the ionospheric plasma drift around noon sector of the polar ionosphere. *Journal of Geophysical Research: Space Physics*, *123*(3), 2370–2378. https://doi.org/10.1002/2017ja024805

Welch, P. (1967). The use of fast Fourier transform for the estimation of power spectra: A method based on time averaging over short, modified periodograms. *IEEE Transactions on audio and electroacoustics*, *15*(2), 70–73. https://doi.org/10.1109/TAU.1967.1161901

Wygant, J., Keiling, A., Cattell, C., Johnson, l. M., Lysak, R., Temerin, M., et al. (2000). Polar spacecraft based comparisons of intense electric fields and Poynting flux near and within the plasma sheet-tail lobe boundary to UVI images: An energy source for the aurora. *Journal of Geophysical Research*, *105*(A8), 18675–18692. https://doi.org/10.1029/1999JA900500

Yeh, K. C., & Liu, C.-H. (1982). Radio wave scintillations in the ionosphere. *Proceedings of the IEEE*, *70*(4), 324–360. https://doi.org/10.1109/PROC.1982.12313

Zheng, Y., Xiong, C., Jin, Y., Liu, D., Oksavik, K., Xu, C., et al. (2022). The refractive and diffractive contributions to GPS signal scintillation at high latitudes during the geomagnetic storm on 7-8 September 2017.

Paper III

Plasma structuring within an expanded active cusp region studied with the SS-520-3 sounding rocket

Lisa M. Buschmann, Kazushi Asamura, Lasse B.N. Clausen, Yaqi Jin, Hirotsugu Kojima, Atsushi Kumamoto, Satoshi Kurita, Yasunobu Ogawa, Kjellmar Oksavik, Yoshifumi Saito, Andres Spicher, Shoichiro Yokota, Wojciech J. Miloch

Submitted to Earth, Planets and Space for publication.

III